UNIVERSITÀ DEGLI STUDI DI CATANIA

FACOLTÀ DI INGEGNERIA

DIPARTIMENTO DI INGEGNERIA INDUSTRIALE

PhD Student: Ing. Ignazia Scuderi

"DESIGN OF A WATER PVT SYSTEM INTEGRATED INTO PREFABRICATE CONCRETE"

Dottorato XXVII ciclo: Energetica

Doctoral Dissertation

Tutor:
Chiar.mo Prof. Ing. L. Marletta

SESSION 2014 – 2015

INDEX……….2

CHAPTER 1

CHAPTER 2

PRELIMINARY ANALYSIS TO DESIGN A WATER PVT COLLECTOR……………...………………………………………………………..….46

CHAPTER 3

PLANT LAYOUT AND EXPERIMENTAL RESULTS…………………….....65

CHAPTER 6

INTRODUCTION

Recent hike in oil prices has resulted in strong stimulation of research into renewable energy because such research can make major contributions to the diversity and security of energy supply, to the economic development and to the clean local environment. During the last few years, PVT technology has received great attentions worldwide.

The concept of PVT has been used and discussed for more than three decades by various researchers both experimentally and numerically. During the 1970s, the research on PVT started, with the focus on PVT collectors, with the main aim of increasing the overall energy efficiency.

Hybrid photovoltaic/thermal collectors (PV/T) are devices that convert solar energy simultaneously into thermal and electric energy. As a general rule, they consist of common PV panels refrigerated by means of a suitable coolant fluid, that is collected and made available for appropriate uses. Thus, one can improve the electric efficiency of the PV cells while recovering low-grade heat; hence, PVT collectors are expected to show very interesting energy performance.

In this study, a preliminary analysis was carried out to determine the size of the cross section, the depth of the water duct, the thick and the material of the absorber-plate maintaining the overall performance at a satisfactory level. By means of a thermo-fluid dynamic modeling software "Comsol Multiphysics" it was also possible to determine the temperature distribution throughout the PVT collector .

In addition, this work shows the results of an experimental campaign, carried out on a prototype of PVT collector. The prototype consists of two panels, where a stainless steel absorber plate is cooled by means of a water flow circulating into square channels. On the top side of the absorber plate, polycrystalline PV cells are applied by lamination.

The prototype has been tested during the summer 2013 in the premises of a factory situated near Catania. In order to get controlled operating conditions, the panels have been fed with water at constant temperature, thanks to an appropriate control system. The main parameters acquired during the measurement campaign were: absorber plate temperature, inlet and outlet fluid temperature, available solar radiation and outdoor air temperature.

Now, from the examination of the experimental data, and from the simulations carried out with a mathematical model implemented on Mathcad, it is possible to identify too high temperatures on the absorber plate, as well as a quite low efficiency for the heat recovery. This is due to a series of constructive faults, and mainly to the bad contact between the absorber plate and the channels where the coolant flows.

For this reason, the mathematical model has been modified, in order to introduce an additional thermal resistance. A parametric analysis has allowed to tune the model and to identify the value of this thermal resistance that minimizes the discrepancy between simulated and experimental results.

Starting from the results of this investigation, it was possible to construct a new PVT panel lacking any construction fault, and whose performance are very promising and significantly better than the prototype tested so far.

Finally, in this dissertation, the Second Law analysis of a real PVT and an improved PVT collectors are presented to study a crucial problem for the optimal exploitation of this technology: since the electricity production from PV cell is favoured by low temperatures, whereas the usability of the thermal energy gets higher at high temperatures.

CHAPTER 1

PVT concept and performance analysis

1.1 Introduction

Solar energy is usually utilized after it is converted into energy forms suitable for specific applications. In a hybrid system, such as the photovoltaic/thermal (PVT) energy system, both thermal energy and photovoltaic solar energy (electric) are produced at the same time. In this chapter a review of the available literature covering the latest development of photovoltaic/thermal (PVT) technology is presented, with its performance in terms of electric as well as thermal output. A discussion will be also given about the various systems of heat recovery by means of water or air as coolant fluid, PVT design criteria and different techniques to increase the performance.

1.2 PVT developments

Hybrid photovoltaic/thermal collectors (PVT) are devices that convert solar energy simultaneously into thermal and electric energy. As a general rule, they consist of common PV panels refrigerated by means of a suitable coolant fluid, that is collected and made available for appropriate uses. Thus, one can improve the electric efficiency of the PV cells while recovering low-grade heat. In more detail, in a PV system most of the absorbed solar radiation is not converted into electricity: PV cells utilize a small fraction of the incident solar radiation to produce electricity and the remainder is turned mainly into waste heat in the cells, causing the increase of PV cell temperature, hence the efficiency of the module drops. Cooling either by natural or forced circulation can reduce the PV cell temperature. An alternative to the common PV systems is to use a photovoltaic thermal system (PVT), where PV cells are coupled to heat extraction devices. The simultaneous cooling of the PV module maintains the electrical efficiency at satisfactory level, thus the PVT collector offers a better way of utilizing solar energy due to the increased overall efficiency.

Furthermore, the PVT modules generate more energy per unit surface area than with side by side PV panels and solar thermal collectors, at a lower production and installation cost. Because of its high efficiency per unit surface area, PVT is particularly well suited for applications with both heat and power demand and with limited roof space availability.

Hence, PVT collectors are expected to show very interesting energy performance. With the following figure one can describe how to produce heat and electricity from various properly combined:

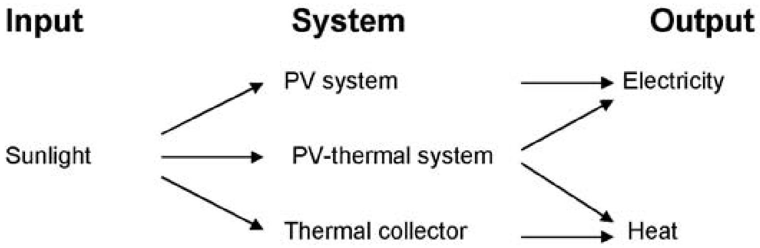

Figure 1. *Comparison between PV, PVT and solar thermal systems*

As a general rule, PVT systems can be classified as:

- Liquid PVT collector;
- Air PVT collector;
- Ventilated PV with heat recovery;
- PVT concentrator.

Irrespective of the type of collector, the absorber of a PVT collector may have a glass cover to reduce the thermal losses. Glazed collectors have smaller thermal losses, especially at higher collector fluid temperatures. For medium to high temperature applications, this results in a much higher annual thermal yield.

However, this may also result in high stagnation temperatures that may be critical for certain types of PV encapsulations (risk of yellowing and delamination); furthermore, the glazing makes the module more sensitive to hot spots. In addition, bypass diodes may get overheated due to the additional insulation. Reflection losses at the glazing further reduce electrical performance. Increased temperature levels lower the electrical yield.

In summary, it is important to find a good balance between the increased thermal yield on one hand, and the reduction in electrical yield and the issues related to possible degradation on the other hand.

1.3 Liquid PV/T collector

In order to improve energy performance of the photovoltaic systems, much effort has been spent on research and development of the hybrid PVT technology using water as the coolant fluid.

The liquid PVT collectors are similar to conventional flat-plate liquid collectors; an absorber with a serpentine tube or a series of parallel risers is applied, onto which PV is laminated or glued by means of adhesive epoxy joint. PVT water systems are more efficient than PVT air systems, due to the higher thermal conductivity and the higher heat capacity, as well as the high density-resulting in a high volume transfer. But the use of water requires more extensive modifications to enable water-tight and corrosion-free construction.

Various design concepts for water- type PVT collectors [3] are possible and can be classified in four groups:

- Sheet-and-tube PVT-collectors;
- Channel PVT-collectors;
- Free flow PVT-collectors;
- Two-absorber PVT-collectors.

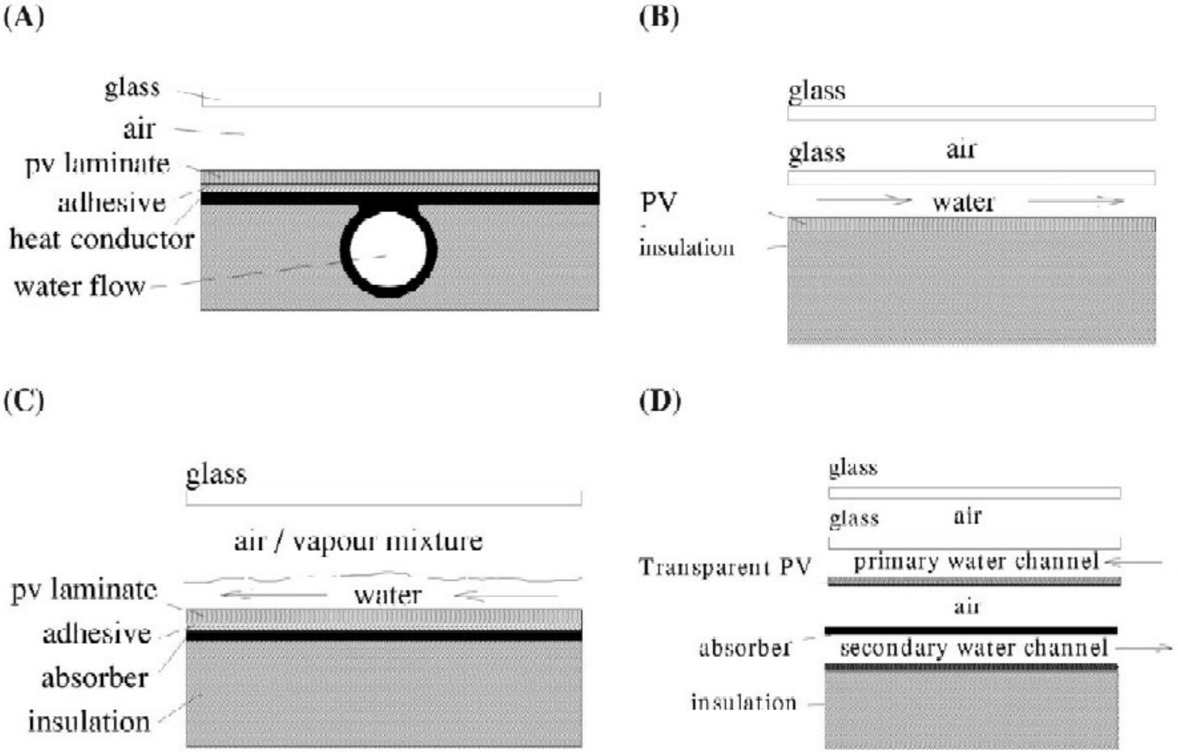

Figure 2. *Various collector concepts: (A) sheet-and-tube PVT, (B) channel PVT, (C) free flow PVT, (D) two-absorber PVT (insulated type).*

1.3.1 Sheet-and-tube PVT-collectors

The simplest way to construct a PVT collector is to rely entirely on well-known available technology by taking a standard photovoltaic panel and integrate it into a thermal collector without any modification.

The sheet-and-tube PVT collector shown in Fig. 2a is an example of such an approach. The thermal insulation of this design can be improved by increasing the number of top covers.

However, since each cover creates additional reflections, this strategy reduces the electrical yield of the PVT collector. Sheet-and-tube PVT collectors are examined with zero, one and two covers. Designs with more than two glass covers do not seem to have practical applications, since the electrical efficiency is reduced too much.

The heat flows in the sheet-and-tube PVT collector are indicated schematically in Fig. 3:

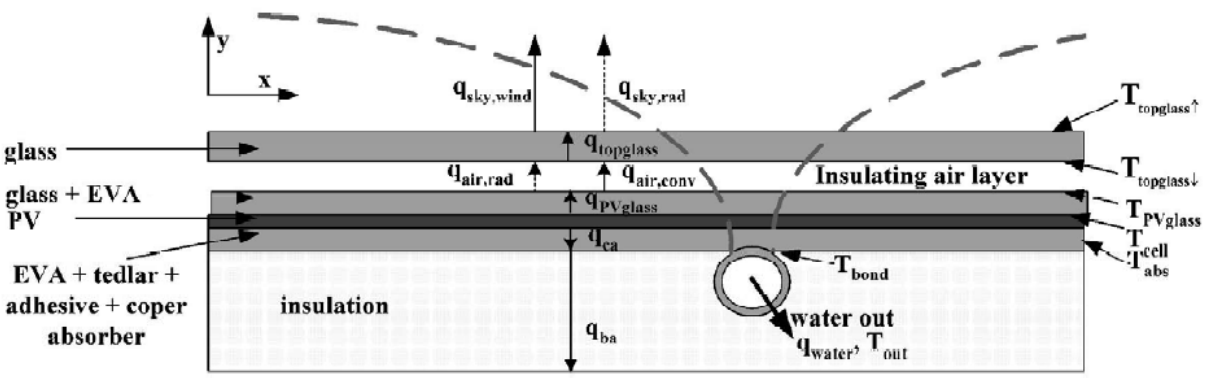

Figure 3. *The heat flows in the sheet-and-tube PVT-panel, together with the temperature distribution according to the Hottel–Whillier equations*

For the sheet-and-tube PVT collector, the heat balance is represented by the following equations:

$$q_{water} = q_{ca} - q_{ba} \tag{1}$$

$$q_{ca} = \tau_{\alpha} - \tau_{PV}\eta\,\big) G - q_{PVglass} \tag{2}$$

$$q_{PVglass} = q_{air,conv} + q_{air,rad} \tag{3}$$

$$q_{air,conv} + q_{air,rad} = q_{topglass} \tag{4}$$

$$q_{topglass} = q_{sky,conv} + q_{sky,rad} \tag{5}$$

The set of equations presented above is for the case of the panel with one cover. For the case with no cover, Eqs. (3) and (4) are left out, while in Eq. (5) q_{topglass} is changed into q_{PVglass}. For the panel with two covers, Eqs. (3) and (4) are repeated. In contrast to the case of the channel collector designs, for the sheet-and-tube collector the PV is connected to a separate thermal absorber plate by means of adhesive layer. Therefore, the heat transfer between the PV cells and the absorber plate should be modelled as well.

This is taken into account by using Eqs. (6) and (7) indicated below:

$$q_{ca} = h_{ca}\left(T_{cell} - T_{abs}\right)$$

$$q_{ba} = h_{ba}\left(T_{abs} - T_{a}\right)$$

In which h_{ca} and h_{ba} represent respectively the heat transfer coefficients from the cells to the absorber and from the absorber to the back of the collector, T_{abs} is the average absorber temperature and T_a the ambient temperature. In more detail h_{ca} can be calculated as follow:.

$$h_{ca} = \left(R_{EVA} + R_{tedlar} + R_{glue}\right)^{-1}$$

In order to solve the equations for the heat flows, the average absorber temperature T_{abs} is calculated from the temperature distribution indicated by Hottel-Whillier equations:

$$T_{abs}(x) = T_a + \frac{\left(\tau_\alpha - \tau_{PV}\eta_{PV}\right)G}{U_{loss}} + \cosh(mh)\frac{\left[T_{bond} - T_a - \left(\tau_\alpha - \tau_{PV}\eta_{PV}\right)G/U_{loss}\right]}{\cosh\left[m(W - D)/2\right]} \qquad (8)$$

With

$$m = \sqrt{U_{loss}/k\delta_{abs}}$$

In which the heat loss coefficient and the bond temperature are given by:

$$U_{loss} = \frac{q_{sky,rad} + q_{sky,conv} + q_{ba}}{T_{PVglass} - T_a}$$

$$T_{bond} = T_{water} + q_{water}/h_{tube}$$

$$= T_{water} + qD/Nu_{tube}k_{water}$$

This temperature distribution is also shown in Figure 3, and results from the fact that a temperature gradient over the absorber is required to drive the absorber heat to the tubes. So Eq. (8) is numerically integrated with respect to *x* in order to provide the average absorber temperature.

1.3.2 Channel PVT-collectors

As shown by Figure 2b, a channel PVT-collector is a simple PV with a channel on the top. Such a configuration imposes constraints on the choice of the collector fluid; for a PVT collector design the absorption spectrum of the fluid should be sufficiently different from the absorption spectrum of the PV in order to allow the PV to receive the incoming radiation.

Usually water is used, which has a small overlap in absorption with the PV, resulting in 4% relative decrease in the electrical performance. A disadvantage of this design is that, if a wide channel is used covered by one glass plate, very thick glass may be necessary to withstand the water pressure,

resulting in a heavy but fragile construction. A variation of the channel design is obtained by letting the water flow underneath the PV panel. Two cases are examined: a channel above a conventional opaque PV panel and a channel below a transparent PV panel with a separate black thermal absorber underneath the channel. The latter can be expected to have a higher thermal efficiency, but it should be kept in mind that transparent PV laminates are at the present substantially more expensive. In addition, the PV panel should be able to withstand the pressure of the water. In the case of opaque PV this might be less of a problem since the backside could be strengthened with a metal back. Care should be taken that the backside of the PV laminate is sufficiently watertight.
The heat flows in the channel PVT collectors are indicated respectively in Fig. 4 and Fig. 5, for the case of channel above and below the PV.

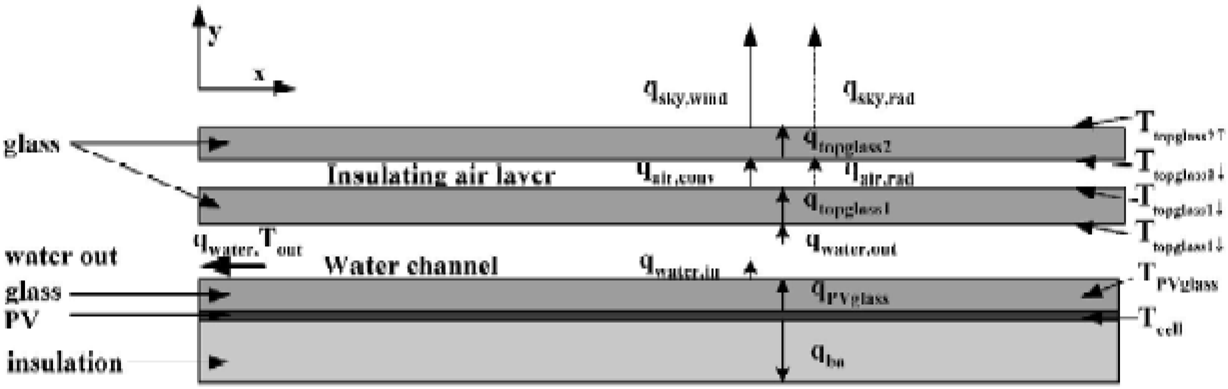

Figure 4 - *The heat flows in the PVT-panel with the channel above the PV*

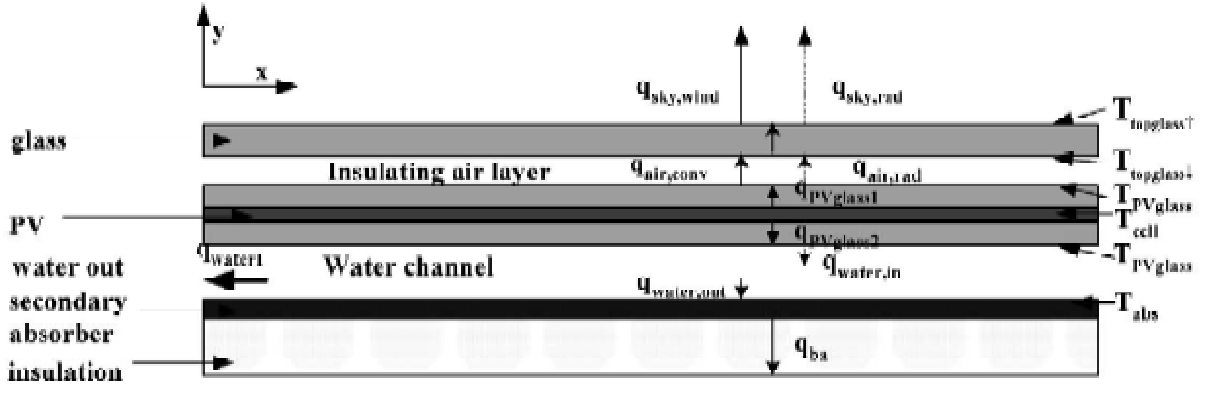

Figure 5 - *The heat flows in the PVT-panel with the channel below the PV*

For this concept a similar approach as for the sheet-and-tube PVT collector can be followed. Therefore for the case of the channel above the PV, the water presents a layer through which part of the heat absorbed by PV is lost to the collector surface again, in contrast to the case of the sheet-and–tube absorber. Part of the incoming heat $q_{water,in}$ will be retained in the water and drawn off

(q_{water}), while another part will be transferred from the water layer to the glass plate on the top of the water channel ($q_{water,out}$). In addition, the water now absorbs solar energy directly as well, according to the transmission-absorption coefficient for the water τ_{water}. The case for the channel-below-transparent-PV is similar to the channel-above-PV, but the heat flow from the PV upwards is now entirely lost, while the heat flow downwards contributes to the collected heat. In addition, cover glass on the top of the channel disappears.

1.3.3 Free flow PVT-collector

In a free flow panel unrestrained fluid flows over the absorber, as shown in Fig. 2c. In comparison to the channel case, this design eliminates one glass layer. Thus reflections and material costs are reduced, while the mechanical problem of breaking the glass cover is avoided. A disadvantage is the increased heat loss due to evaporation. As in the case of the channel PVT-collector, the fluid flowing over the PV panel has to be transparent for the solar spectrum. Water seems a natural choice, but, since its evaporation pressure is not very low, evaporation will be shown to create problems to higher temperatures. The heat flows in the free flow PVT-collector are indicated schematically in Fig. 6:

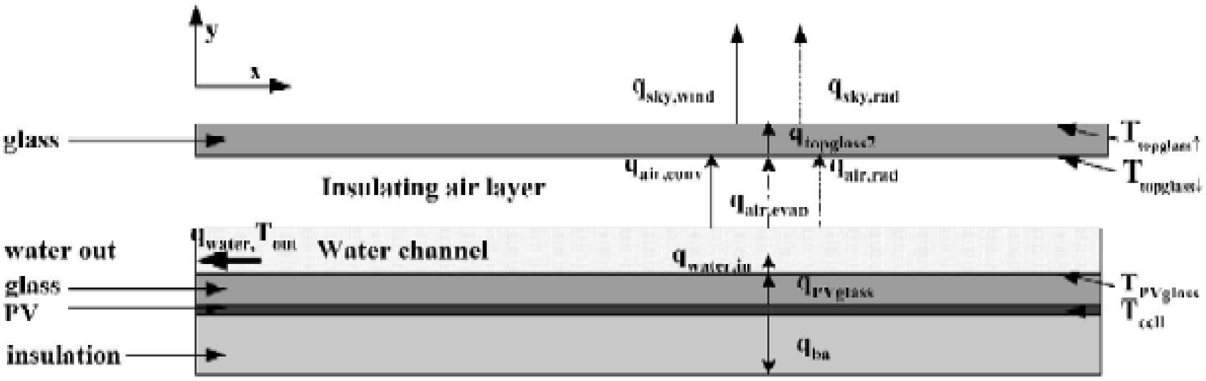

Figure 6 - *The heat flows in the free flow PVT-panel*

In the free flow concept the solving procedure is similar as for the PVT-collector design with the channel above the PV. However, in the free flow panel evaporative heat transfer takes place. The model assumes that the evaporation process at the water film on the PV laminate and the subsequent condensation process at the top glass layer are much faster than the actual transport of the water vapour through the air /vapour mixture due to concentration differences. Therefore, this diffusion process determines the evaporative heat transfer coefficient. The natural convection due to the temperature difference over the air layer enhances this process. Because of the similarity of the free flow design with the PVT-collector design with the channel above the PV, the approach to study the heat flow is the same as in the latter case. The difference is the absence of the topglass1, so that thermal radiation and convection take place directly between the water layer and the topglass2. However, the fact that air is present above the fluid introduces a new heat transfer mechanism due to evaporation.

1.3.4 Two-absorber PVT-collectors

The two-absorber panel uses a transparent PV laminate as a primary absorber and a black metal plate as a secondary absorber. The panel contains two water channels on top of each other. The water flows through the upper channel and is returned through the lower channel. However, the disadvantage of the heavy channel cover - indicated previously for the channel PVT - applies even more strongly for the two-absorber PVT.

Several variations can be applied in the design. The efficiency of the design could be improved by an additional transparent insulating layer between the primary and the secondary channel to reduce the heat loss further (Fig. 7). On the other hand, this reduces the robustness of the collector. One of the main advantages of this concept is that a lower mean PV cell temperature is maintained, compared to geometries with heat and electricity generation in one plane. Another possible variation is obtained by replacing the channel under the secondary absorber by a sheet-and-tube construction.

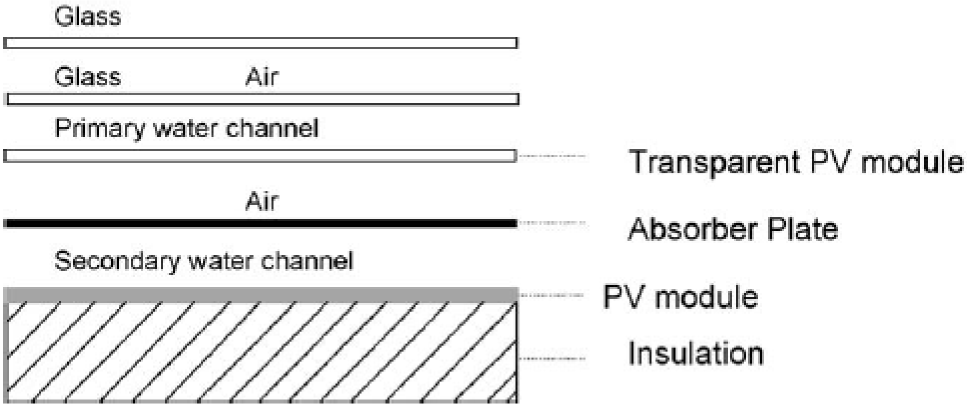

Figure 7. *Two-absorber PVT-model.*

1.4 Electrical and thermal efficiencies of PVT water

The electrical efficiency is a function of temperature with respect to the effect of the electrical production, it is subtracted from the transmission absorption factor to find the amount of thermal energy that was absorbed in the system, according to $\tau_{\alpha eff} = (\tau_{\alpha} - \tau_{pv}\eta_{el})$. In this way one obtains the amount of absorbed heat that contributes to the thermal yield. The yield of the collector is defined as the amount of useful energy produced, while the efficiency is defined as the yield divided by the amount of solar energy received by the collector. The electrical and thermal efficiency are there defined as follows[3]:

$$\eta_{th} = \dot{m}\frac{c\left(T_{out} - T_{in}\right)}{G} \tag{9}$$

$$\eta_{el} = \frac{V_{MPP}I_{MPP}}{GA} \tag{10}$$

In which V_{MPP} and I_{MPP} represent the voltage and the current in the maximum power point, A is the panel area, c is the heat capacity of the working fluid (water), $\dot{m}$ the mass flow for square meter in [$kg \cdot s^{-1} \cdot m^2$], G the irradiation in [$W \cdot m^{-2}$] and T_{in} and T_{out} are the inlet temperature and the outlet temperature in [°C], respectively. The thermal efficiency is conventionally stated as a function of the reduced temperature, which is defined as

$$T_{red} = \frac{T_{in} - T_a}{G} \tag{11}$$

In which T_a represents the ambient temperature.

But to evaluate the PV electrical efficiency of the above mentioned models, the following formula was used:

$$\eta_{el} = \eta_0\left(1 - 0.0045\left(T - 25^\circ\right)\right)$$

In which η_0=0.097 for both conventional and transparent PV.

For the various designs described above, the thermal efficiency curves are shown in fig 8 and the electrical efficiencies in fig.9. Table 1 shows the thermal and electrical efficiencies at zero reduced temperature.

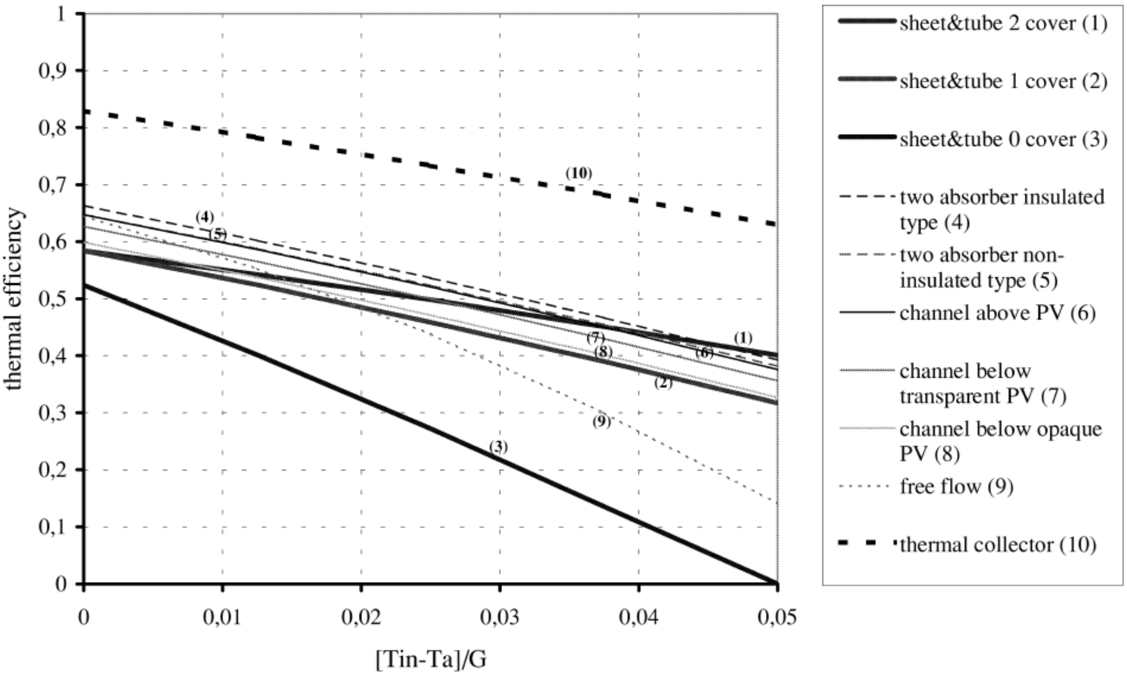

Figure 8. *Thermal efficiency of various PVT panels*

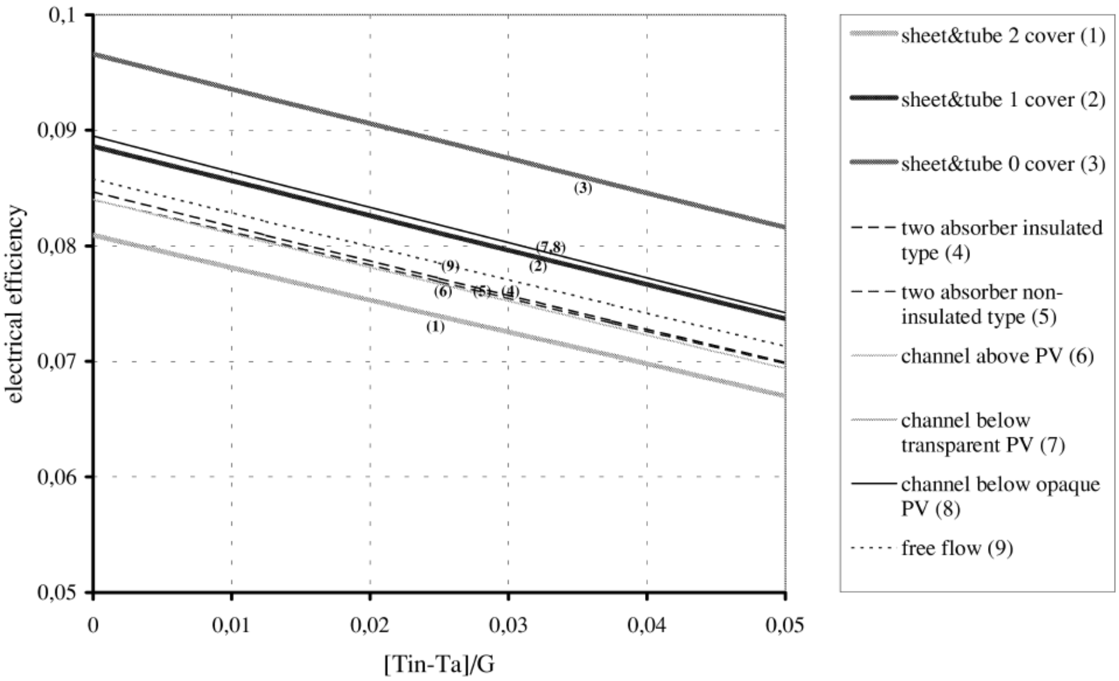

Figure 9. *Electrical efficiency of various PVT panels.*

Panel type	Thermal efficiency	Electrical efficiency
PV laminate	–	0.097
Sheet and tube PVT-collector 0 cover	0.52	0.097
Sheet and tube PVT-collector 1 cover	0.58	0.089
Sheet and tube PVT-collector 2 covers	0.58	0.081
PVT-collector with channel above PV	0.65	0.084
PVT-collector with channel below opaque PV	0.60	0.090
PVT-collector with channel below transparent PV	0.63	0.090
Free flow PVT-collector	0.64	0.086
Two-absorber PVT-collector (insulated type)	0.66	0.085
Two-absorber PVT-collector (non-insulated type)	0.65	0.084
Thermal collector	0.83	–

Table 1.*Thermal and electric efficiency of various PVT-collector design concepts***.**

One can notice that the uncovered sheet-and-tube collector is obviously performing poorest at zero reduced temperature because of its large heat losses. The sheet-and-tube collectors with one or two covers have a substantially higher efficiency at these conditions. It seems that a sheet-and tube collector with two covers is only useful for high temperature applications, since the electrical efficiency strongly deteriorates due to the second cover, while the thermal efficiency does not show a significant increase at modest values of reduced temperature. In addition, it can be observed that all channel concepts have a substantially higher efficiency than the sheet-and-tube collectors because of the excellent heat transfer properties.

Furthermore, for the case of the free flow panel, Fig. 8 shows that evaporation strongly reduces the thermal efficiency at higher reduced temperatures. It can be concluded that, at higher reduced temperatures, water is not a good choice for a free flow collector. An extra complication is caused by the fact that the condensate on the top glass layer will cause additional reflection of the radiation, which will reduce the efficiency at reduced temperatures even faster than shown in Fig. 8. An advantage of the free flow concept is its intrinsic prevention against overheating because of the strong increase in the rate of evaporation towards higher temperatures.

1.5 Air PVT collector

The PVT air collectors are similar to a conventional air collector heater with a PV laminate functioning as the top or bottom cover of the air channel. PVT air collectors are cheaper than the PVT liquid collectors because conventional PV modules can be easily converted to a PVT system, with very few modifications.

PVT air collectors can either be glazed or unglazed. In general, air collectors are mostly applied if there is a demand of hot air from the end-users. Presently, this technology is mainly designed for space heating applications. However, the opportunity for this application depends directly on the market share of air heating systems, which is low in most countries. A niche market is given by preheating of ventilation air for large volume buildings (stores, sport halls, schools and other commercial buildings) where temperatures in the range of 15–25°C are desirable. With the same air systems, hot water preparation is often possible through an air/water heat exchanger, which is generally done during the summer season in order to increase the overall performance of the system. The application of air as a heat transport medium compared to air, has significant advantages along with few inevitable disadvantages.

Advantages:

- No freezing and no boiling of the collector fluid.
- No damage if leakages occur.

Disadvantages:

- Low heat capacity and low heat conductivity, which result in a low heat transfer.
- Low density, which results in a high volume transfer.
- High heat losses through air leakage.

As the heat transfer in the air-cooled PVT system is much more critical than in the liquid cooled PVT system, it is important to model the heat transfer properly.

1.5.1 Single and double pass PVT Air

First, air PVT collectors can be classified in two groups, namely single and double pass combined photovoltaic thermal collectors, as shown in figure 10:

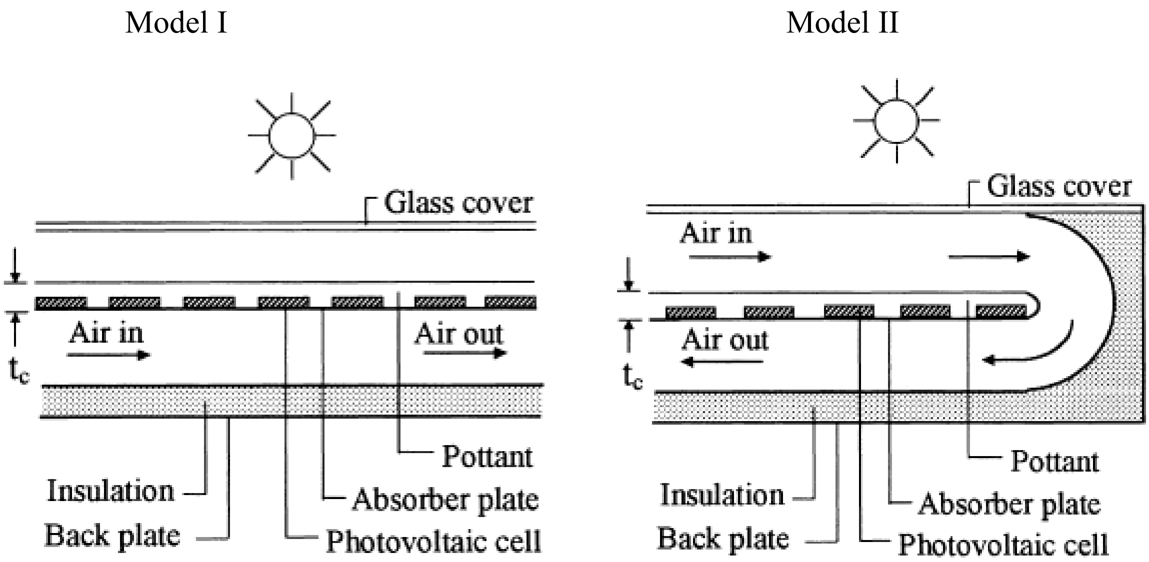

Figure 10: *Configuration of two PVT air collectors designs: a) single pass; b) double pass.*

The single-pass PVT system is essentially a single-glazing air heater with the air flow passage between two metallic plates. The upper metallic plate is painted in black and the photovoltaic cells are pasted over it. The material used to paste the cells on the absorber plate is a good thermal conductor and a good electrical insulator. The cells can be either circular or rectangular. For rectangular cells, it is possible to cover the entire area of the absorber plate.

As concerns the double-pass PVT heater, air first enters the flow channel formed by the glass cover and the upper metallic collector, and then flows under it. This flow arrangement produces greater heat removal from the top absorber plate, and also reduces the heat loss from the collector. The upper and lower metallic plates are painted in black and the photovoltaic cells are pasted over the upper plate. The air must not come in contact with the bare cells, otherwise the cells would be damaged. Hence, a protective transparent layer has to be applied to the surface.

Both models have been analyzed by Sopian and Ygit [4] in steady–state conditions using the energy balance equations at various nodes of the collector: at the glass cover, absorber plate and working fluid (air). In this research, it was assumed that various parameters, as the absorber plate temperature, mass flow rate, duct depth, collector length, inlet temperature, solar radiation and packing factor affect the performance of the single-pass and double-pass photovoltaic thermal solar collector. Sopian and Ygit kept constant the values of solar irradiance and ambient temperature at S

= 1000 W/m^2 and T_a = 22°C, respectively, and generated the efficiency curves varying T_{fi} (inlet fluid temperature), with the packing factor ranging from P = 0.25 to P = 1.00. Figures 11 and 12 show the thermal and electrical efficiency:

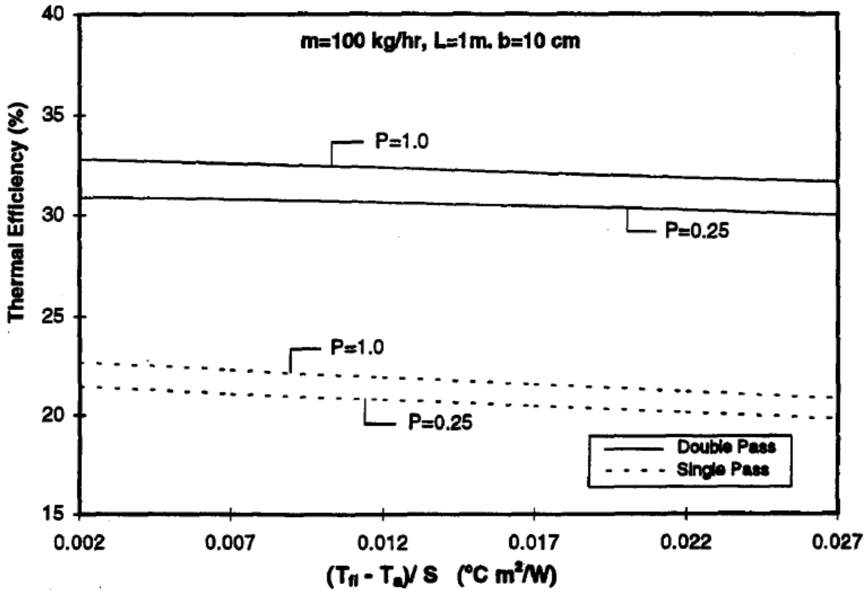

Figure 11. *Thermal efficiency curves for the single-pass and double-pass PVT collector.*

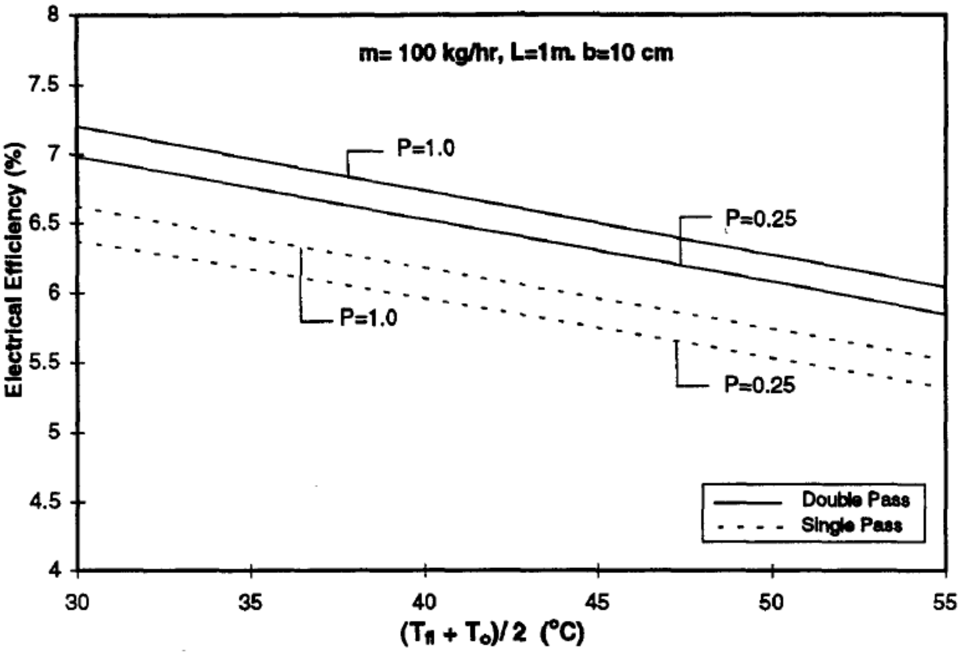

Figure 12. *Electrical efficiency curves for the single-pass and double-pass PVT collector.*

In Fig 11 a typical efficiency versus ((T_{fi}-T_a)/S) curve is normally used as a standard form for rating commercial thermal collectors.

Instead Figure 12 shows the electrical efficiencies plotted as a function of the average fluid temperature in the collector, (T_{fo} + T_0)/2.

Instead, if one considers the daily variation of solar radiation and ambient temperature, which have been utilized in analyzing both the single-pass and double-pass PVT collectors, for the single-pass PVT collector with length of 1 m, the maximum outlet temperature of 44°C and 48°C can be achieved, respectively. A similar analysis for the double-pass photovoltaic thermal solar collector was performed, and for collector lengths of 1 and 2 m the maximum outlet temperatures for the day are 47°C and 55°C, respectively.

The effects of mass flow rate, packing factor, and length of the absorber on the PV cell efficiency were plotted and are shown in Figures 13 and 14 for the single and double pass cases, respectively.

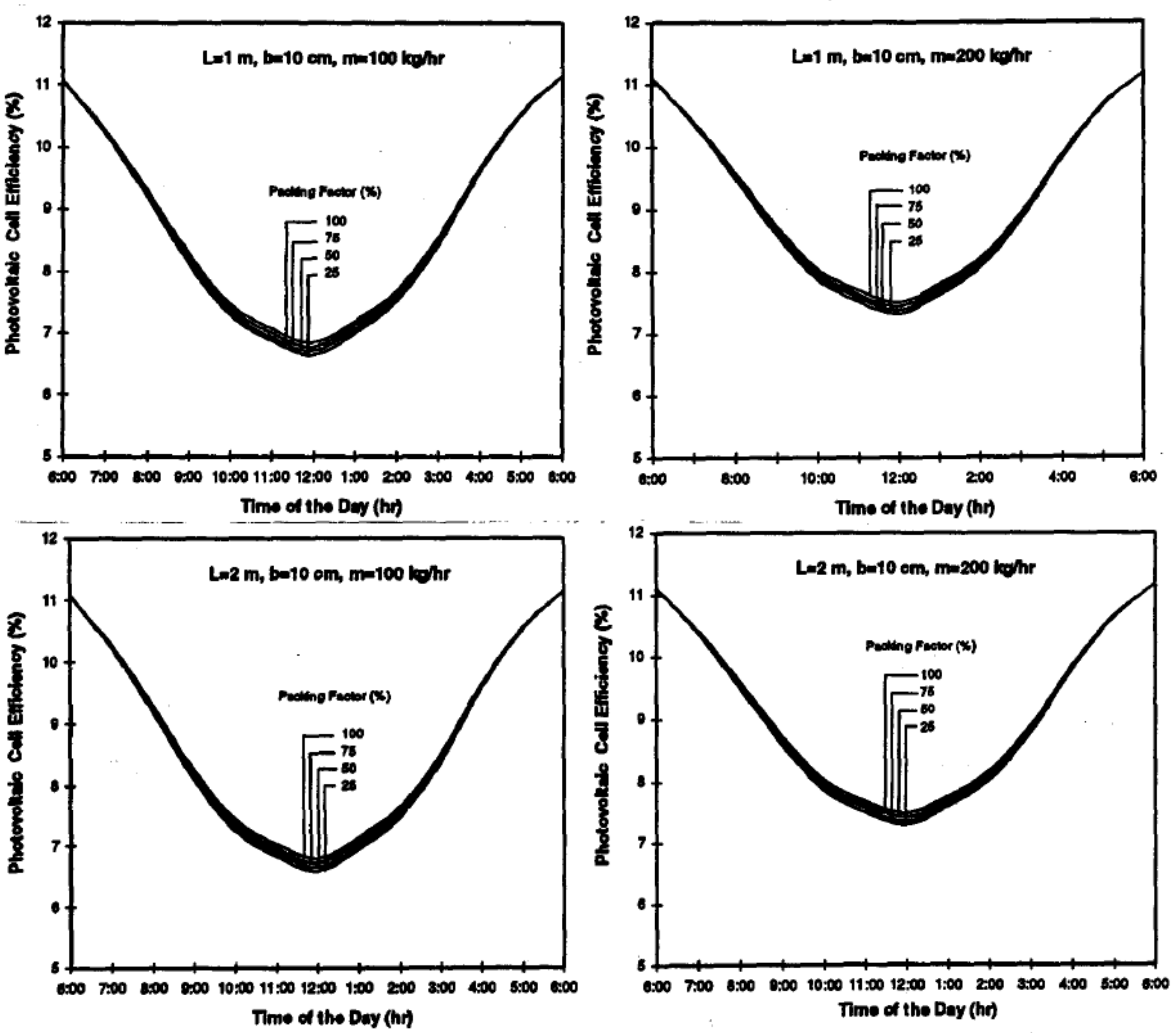

Figure 13. *Effect of mass flow rate, packing factor and length of the absorber on the photovoltaic cell efficiency for single pass collector.*

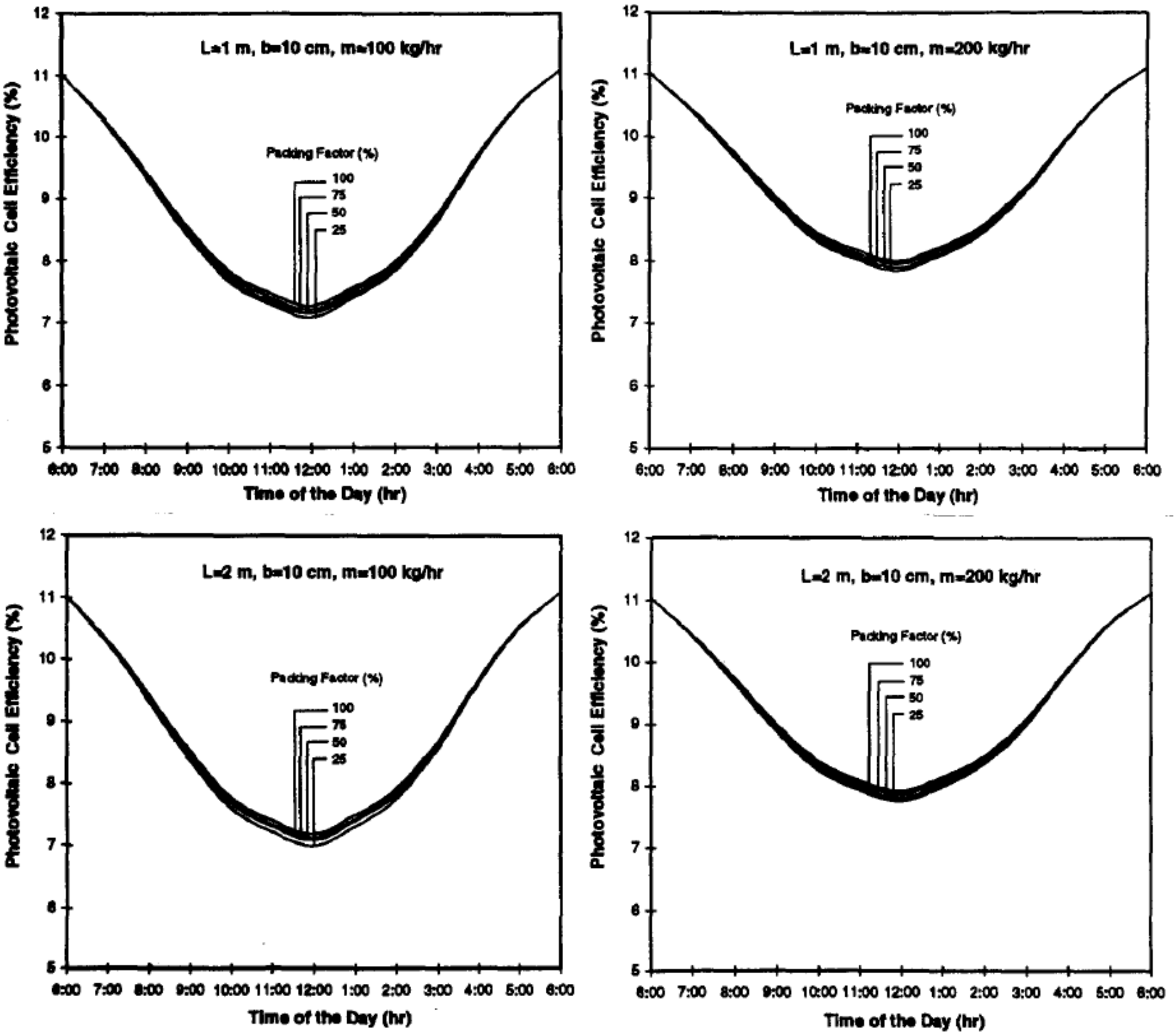

Figure 14. *Effect of mass flow rate, packing factor and length of the absorber on the photovoltaic cell efficiency for double pass collector.*

From the figures, it can be seen that, as the absorber plate length increases, the efficiency of the photovoltaic cell decreases since the average absorber plate temperature increases.

Furthermore, for the same length of collector plate, if the flow rate increases, the photovoltaic cell efficiency increases. Hence, the output from the photovoltaic cells increases for increasing air flow, regardless of the values of the packing factor. As the thermal efficiency of the photovoltaic thermal solar collector increases, the mean photovoltaic cell temperature decreases and, hence, the combined solar efficiency increases. A lower thermal efficiency implies an increase in the average absorber plate temperature.

In the case of the double-pass photovoltaic thermal collector, the working fluid cools the absorber plate and the glass cover. Hence, there is a reduction in the temperature difference of the absorber and the glass cover, thereby reducing the top losses. The photovoltaic cell efficiency is slightly higher for the double-pass photovoltaic thermal collector than for the single-pass photovoltaic thermal collector. For example, at a collector length of 1 m, duct depth of 10 cm, flow rate of 100 [kg·h^{-1}], and a packing factor P = 1, the PV cell efficiencies at noon are 6.7% and 7.5% for the single-pass and double-pass, respectively. In addition, when L = 1 m, mass flow rate 200-300 [kg·h^{-1}] and PF= 0.5 the average daily thermal, photovoltaic and combined for the single and double pass collector and are resumed in Table 2 as follows:

	Single pass PVT		***Double pass PVT***		***u.m.***
mass flow	200	300	200	300	[kg·h^{-1}]
$\eta_{thermal}$	24	28	32	34	[%]
$\eta_{electrical}$	6	7	8	9	[%]
$\eta_{combined}$	30	35	40	45	[%]

Table 2. *Average daily thermal, photovoltaic and combined efficiencies for the single and double pass PVT collector*

Further different studies have been made on new different configurations of hybrid air collectors as single glazing PVT systems, in which air may flow over the absorber and even on both sides of the absorber in a single pass as shown in the Figure 15:

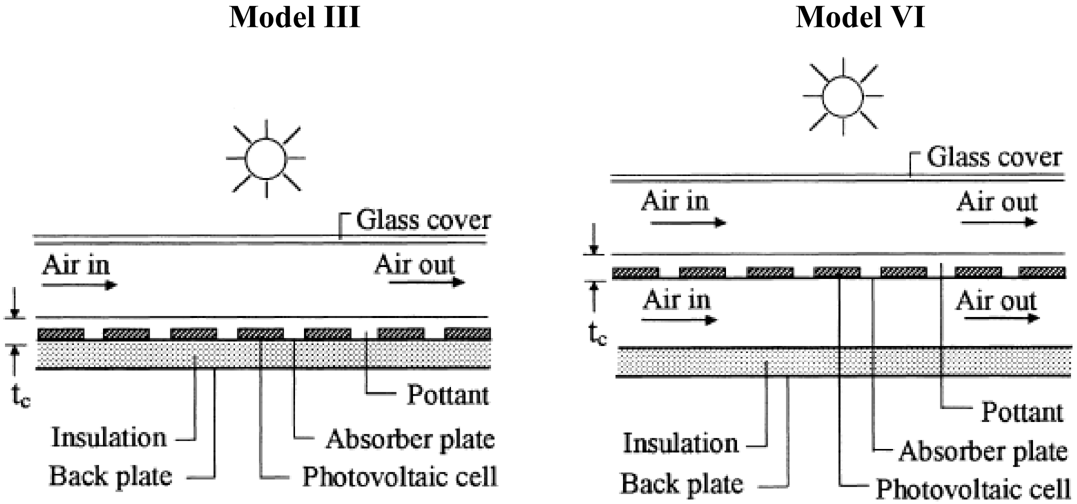
Model III

Model VI

Figure 15. *Schematics of the various PVT models*

In [5] the overall performance of these two collectors were studied in addition to those shown in Fig 10. In particular the daily variation of the thermal and the electrical efficiency were determined for eight specific air mass flow rates, spanning in the range G = 0.005-0.04 [kg·s^{-1}·m^{-2}], as illustrated in Fig. 16 and Fig. 17.

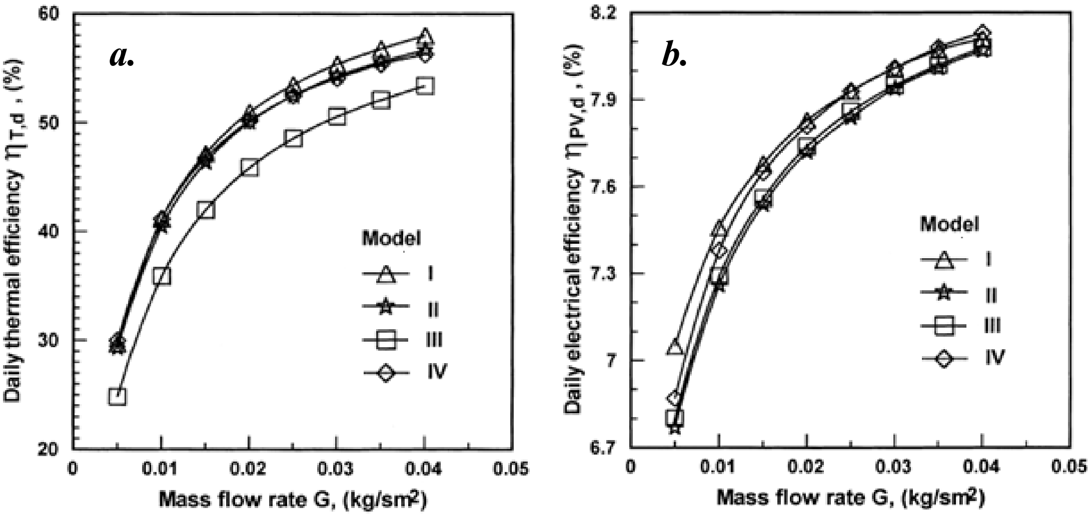

Figure 16. *Variation of daily thermal [a] and electrical [b] efficiency with air mass flow rate for PVT collectors I-IV.*

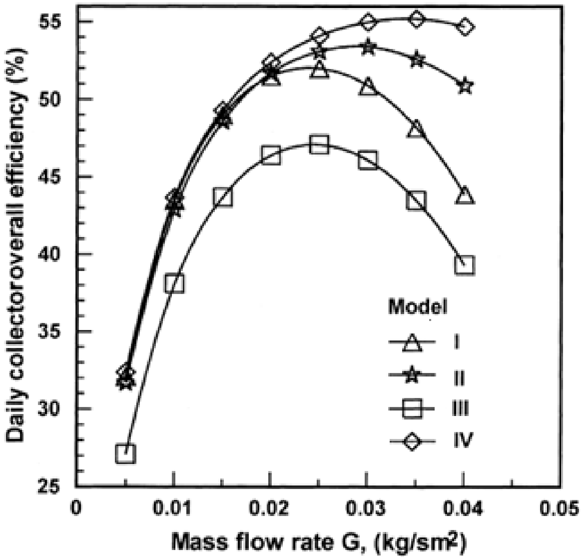

Figure 17. *Daily collector overall efficiency for models I-IV as a function of air mass flow rate.*

As a summary, the following conclusions can be drawn. First, Model I shows a thermal performance comparable with that of Model IV up to G < 0.02 [kg·s^{-1}·m^{-2}], but it has better thermal performance for higher flow rates. Then, the PV energy generated from Model I is relatively higher than for the other models, but its amount is close to that of Model IV for G > 0.02 [kg·s^{-1}·m^{-2}]. Furthermore, the daily electrical efficiencies of the four PVT models are related to the thermal efficiencies. In fact, it is obvious that as the air temperature rise of a particular model gets lower with increasing specific mass rate G, the collector $\eta_{PV,d}$ gets correspondingly higher due to the decrease in the average temperatures of the PV modules. However, the enhancement in the value of $\eta_{PV,d}$ is remarkably small as compared to the increase in the value of the G rate.

Generally, the overall efficiency of a particular PVT model increases with an increase in air mass rate G, attains a maximum value and then decreases with a further increase in G. This is attributed to the sharp increase in fan power with increasing G, while the accompanying enhancements in the generated PV energy and the collected heat (Fig. 16) are, respectively, slight and moderate. Also obvious in Fig. 17 is that the Model III collector has the lowest overall performance among the other models for all mass rates G. In the range of $G < 0.02$ kg [$s^{-1} \cdot m^{-2}$], Models I-II have almost identical overall performances.

To improve the performance of Model I, as it is easier and cheaper to implement, in comparison to the other configurations, other studies have recently been performed trying to add a double layer of glass on cells with or without Tedlar under them, as shown in Figure 18.

Tiwari and Sodha [6] demonstrated that the outlet air temperature, back surface module temperature and solar cell temperature for glazed hybrid PVT without Tedlar is slightly higher than with glazed hybrid PVT with Tedlar. They also found out that the rate of useful thermal energy obtained for glazed hybrid PVT systems was higher than unglazed systems. Irrespective of the PVT system with or without Tedlar, the study reported that there is a significant increase in overall efficiency of the hybrid PVT system, and it can be more pronounced if more small modules are connected in series.

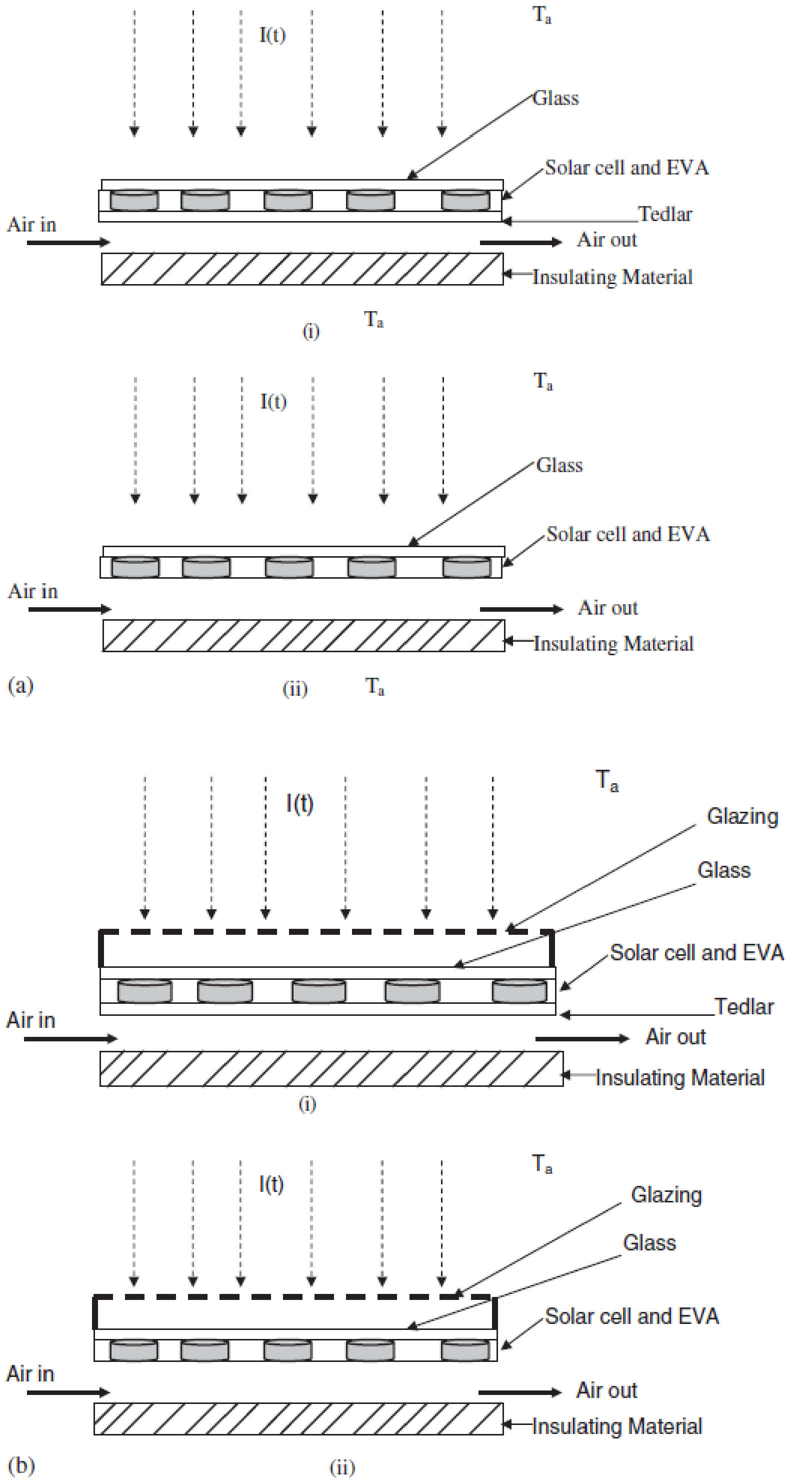

Figure 18 *(a) Cross-sectional view of unglazed PVT air (i) with tedlar, (ii) without tedlar.(b)Cross sectional PVT air (i) with tedlar, (ii) without tedlar.*

1.6 Ventilated PV with heat recovery

In conventional PV facades or PV roofs, an air gap is often present at the rear in order to allow the air to cool the PV by means of natural convection (ventilated PV). If this heat can be recovered and used in the building, then the same PV is considered to function as a PVT collector. Such PV façades, apart from providing electricity and heat, have additional benefits as well:

- A PV façade may limit the thermal losses by infiltration. It also has the advantage to shield the building from the solar irradiance, thereby reducing the cooling load. Hence, such façades are especially useful for retrofitting poorly insulated existing offices;
- If there is no demand for the generated heat, then air collectors and PV façades can use their buoyancy induced pressure difference to assist the ventilation;
- Facade integration of PV has an additional cost incentive of substituting expensive facade cladding materials.

Because of their easier construction and operation, hybrid PVT systems with air heat extraction are more extensively studied, mainly as an alternative and cost effective solution to building integrated PV systems (BIPV).

1.6.1 Performance evaluation of different application of ventilated PV

The effective cooling of a PV panel is able to increase the electricity output of the solar cells. This paragraph describes a comparative study of four different options in applying large-scale building-integrated PV technology [7] in a coastal city at the South China Sea. The computational model was based on a 260 m^2 mono-crystalline silicon PV wall on a 30-storey hotel building.

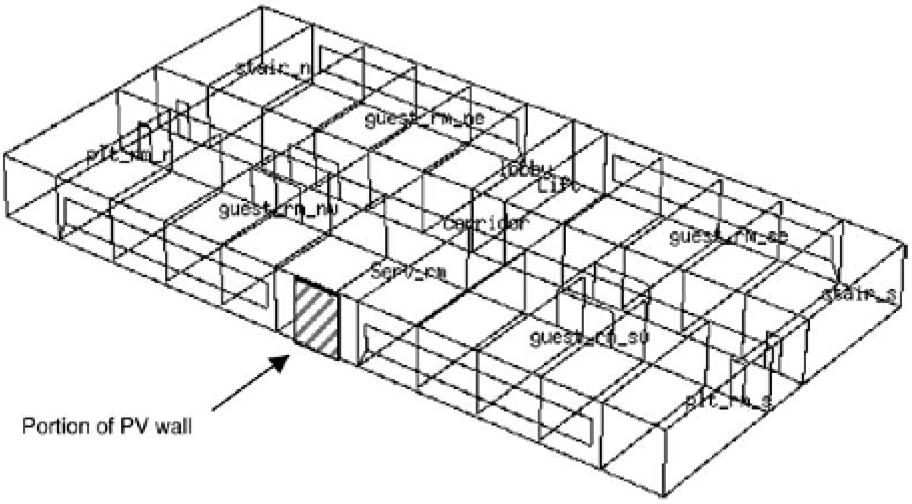

Figure 19. *Hotel tower with PV wall on west-facing façade.*

The results showed that the different design options exhibit differences in the electrical performance. However, some design options perform much better in reducing the air-conditioning loads of the building. The four design options evaluated were:

1. PVC case: the air gap remains open at all sides including the top and bottom ends; this maximizes the air cooling effect through both wind-induced and buoyant effects.
2. PVT case: the air gap opens at the top and bottom ends with all other sides concealed; the air gap behaves like a solar chimney for the production of a warm air stream through natural convection.
3. BiPV case: the PV panels are directly mounted on to the external wall of the service room (the common BiPV case).
4. Base case: no provision of PV panels; the building wall is directly exposed under sunlight as a basis for evaluating the space heat gain of the above design options

The annual outputs from the PVC, PVT and BiPV cases are respectively 83680, 83584 and 83205 MJ. The differences are less than 1%. The overall yearly electrical efficiency of all three installations is around 10.2%.

Comparing graphically the space heat gain via the external facade (86.4 m x 3m) behind the PV panels during the summer period from May to October, it can be seen that PVC gives the best performance, followed by PVT and then BiPV as illustrated in Figure 20.

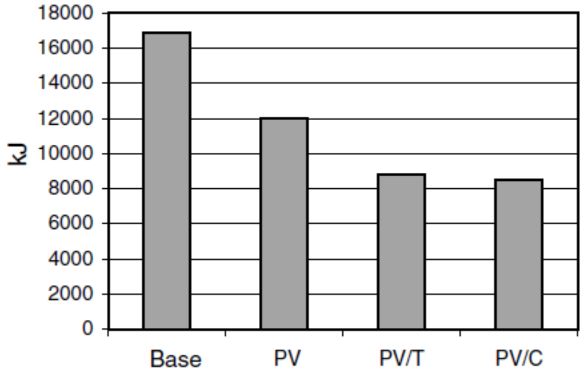

Figure 20. *Comparison of space heat gain via the PV wall for four different designs.*

Compared with the conventional external facade as a reference, the BiPV, PVT and PVC are able to reduce the space heat gain by 29%, 48% and 50% respectively. These values increase to 34%, 52% and 55% respectively when counting only the peak summer week in August. Furthermore, Fig. 21 shows the variation of solar cell temperature at the uppermost panel section during a hot summer day.

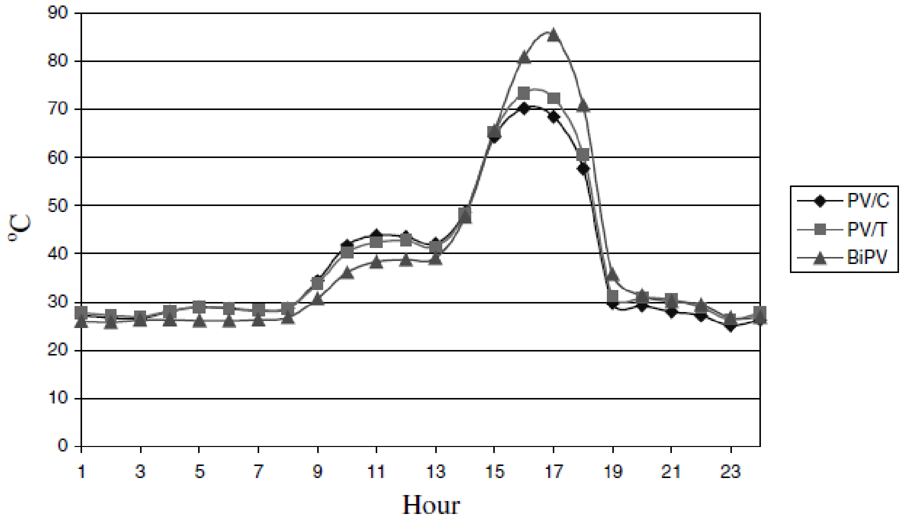

Figure 21. *Variation of solar cell temperature during a hot summer day.*

Another interesting application consists in the use of photovoltaic cladding for walls and roofs of buildings. In this case, an important reduction in temperature of up to 20 K can be obtained by heat transfer to an air flow induced by buoyancy in a duct behind the PV component, with a important increase in the electrical output and reduction of heat gain into the building. Figures 22 and 23 show a realistic roof installation:

Figure 22 *PV roof installation*

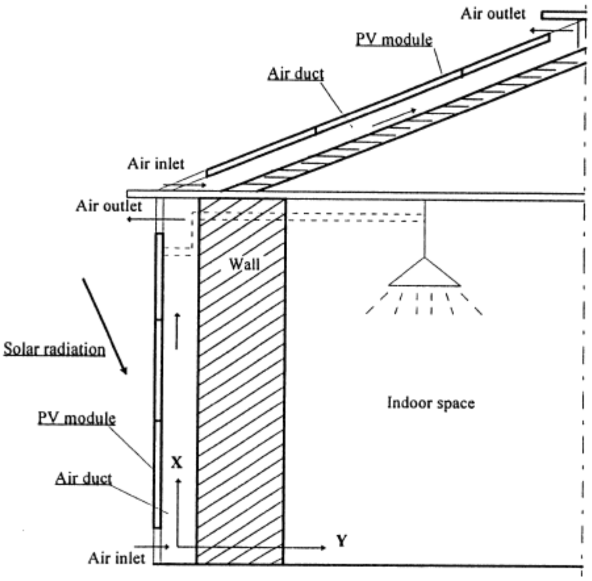

Figure 23 *System schematic of a generic PV .....wall and roof*

For this wall cladding system with height 5 m, air duct depth 120 mm, a wall thickness 240 mm and climate date of a typical day in July 1994 at Cardiff [8] (peak irradiance for a vertical surface 620 W/m^2, ambient temperature between 15 and 22 °C, wind speed between 1.8 and 3.2 m·s^{-1}) the temperature histories of the PV panel, duct air inlet and outlet, wall outer surface are illustrated in Figure 24:

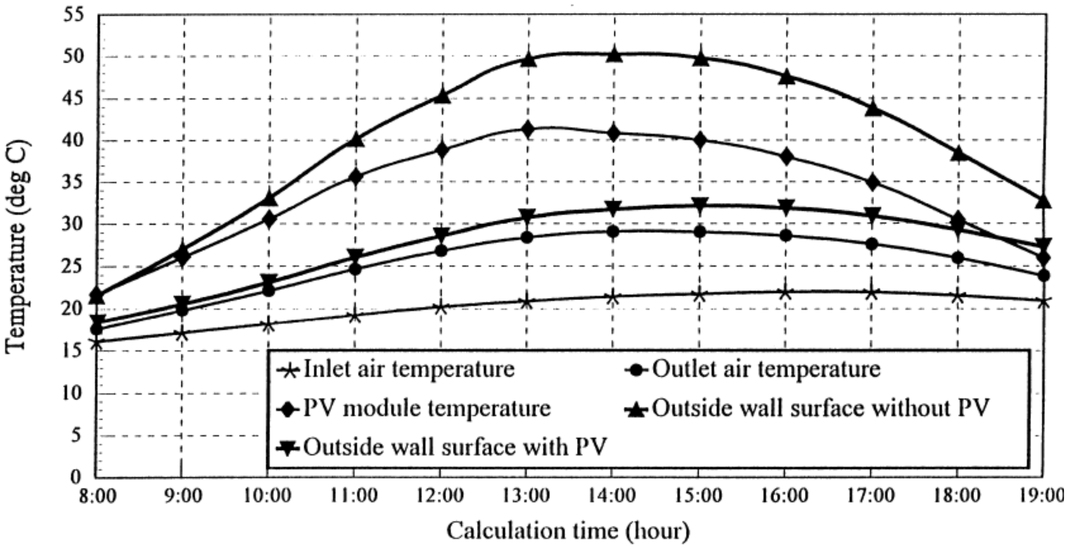

Figure 24. *Temperature histories for a wall cladding system.*

These temperature distributions show that the peak temperature of the outer surface of the wall is reduced from 50°C to 32°C, followed by a significant reduction in heat gains. For this model, the most critical variable for optimum performance is the dimension of the air duct. In fact, an increase in duct height increases the temperature rise of the duct air, thus increasing the buoyant flow and the convective heat transfer coefficient at rear of the PV panel. On other hand, the higher temperature of the duct air and the surface of the backing wall in the upper part of the system raise the sink temperature into which heat is rejected. Figure 25 shows the predicted effect of duct height on the relevant quantities for the base case at noon

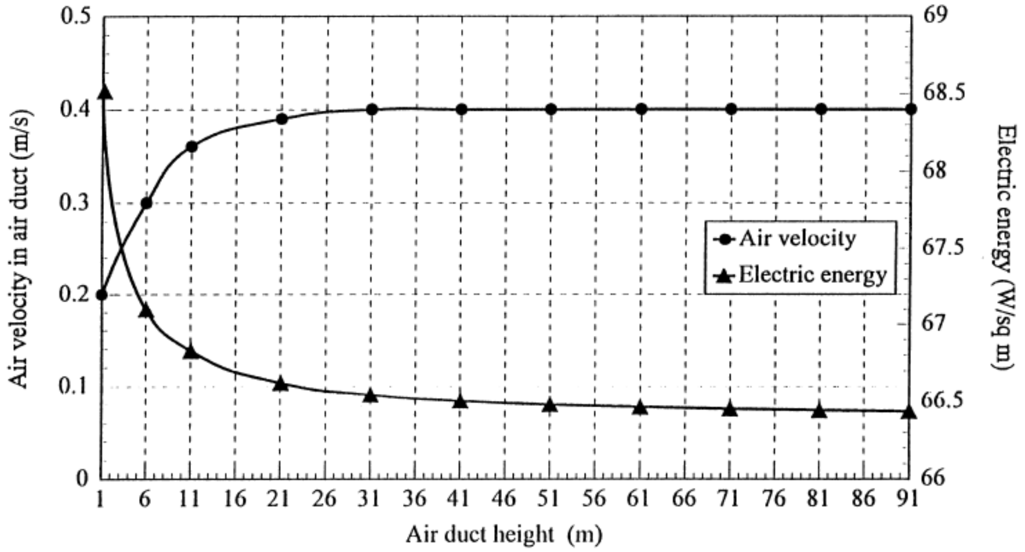

Figure 25. *Effect of air duct height on air velocity and electrical output*

It is seen that in this case the rise in sink temperature overrides the other effects, so that the electrical output falls as duct height increases. The reverse happens for increasing duct depth, where the greater mass flow-rate of the larger channel, which is enhanced by the relative drop in frictional resistance to flow, has the greater effect .An equilibrium between the various factor is eventually reached. Fig.26 shows how the daily total of electrical output varies with duct depth; for this case it is seen that no gain is obtained by employing a depth greater than 250 mm.

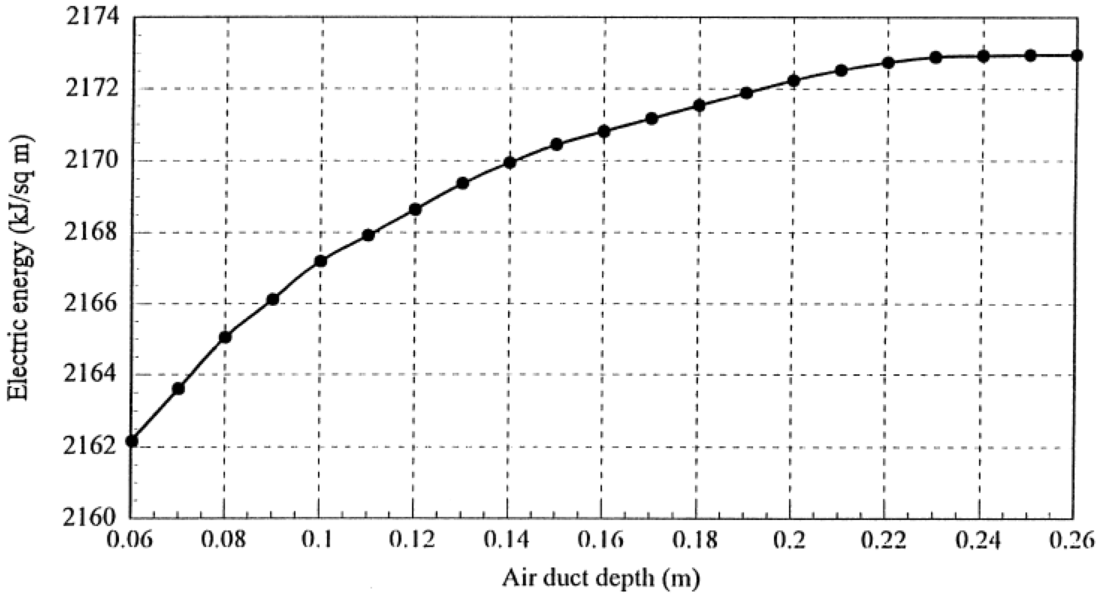

Figure 26. *Daily electrical output for air ducts with different depths*

1.7 Concentrating PVT collectors

The combination of solar radiation concentration devices with PV modules is up to now the most viable method to reduce system cost, replacing the expensive cells with a cheaper solar radiation concentrating system. With such a system, a (large) part of the expensive PV area is replaced by cheap mirror area, which is a way to reduce the payback time. This argument is the driving force behind PV concentrators. Concentrating photovoltaic systems present higher efficiency than the typical ones, but this can be achieved only when the PV module temperature is maintained as low as possible. The concentrating solar systems use reflective and refractive optical devices and are characterized by their concentration ratio (CR) defined as the ratio between the entry aperture and the exit aperture:

$$C = \frac{A_1}{A_2}$$

where A_1 is the area of the entry aperture and A_2 is the area of the exit aperture.

Concentrators can be divided into two groups: concentrating systems with CR > 2.5 must use a system to track the sun, while for systems with CR < 2.5, stationary concentrating devices can be used. The distribution of the solar radiation on the absorber surface (PV module) and its temperature rise are two problems that affect the electrical output. The uniform distribution of the concentrated solar radiation on the PV surface and the suitable cooling mode contribute to an effective system operation and the achievement of high electrical output.

These systems can be classified in different categories: Reflectors of low concentration of flat type or of Compound Parabolic Concentrator (CPC) type, linear or circular Fresnel lenses or reflectors or with parabolic dishes.

The simplest flat type for a concentrator PVT collector has been discussed early by Tripanagnostopoulos [11] placing stationary flat diffuse reflectors as shown in Fig. 27, from the higher part of the modules of one row to the lower part of the modules of the next row. This installation increases solar input on PV modules almost all year round, resulting in an increase of electrical and thermal efficiencies. The diffuse reflectors do not contribute to electrical efficiency drop but an uniform distribution of reflector solar radiation on PV module surface

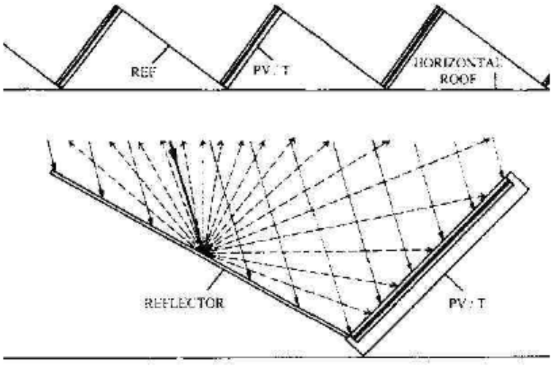

Figure 27. *PVT systems with diffuse reflectors installed between collectors rows*

As mentioned, concentration by linear Fresnel reflectors is also possible. Rosell demonstrated a system based on this method that had a concentrating ratio CR = 11 [12] . They were able to obtain a maximum thermal efficiency of approximately 60% from their system with no electrical load. Moreover, they identified the fact that one of the main thermal resistances in their PVT was that between the PV cell and the absorber plate to which it was bonded.

Regarding the integration of the suggested Fresnel lens in PVT systems [13] on the transparent roof of buildings, Fig. 28 presents the design principle of the Fresnel lens (left), which is a non-imaging concentrator and therefore the refractive rays form a diffused image of sun at the focal length. In the same figure (right), present six types of possible solar radiation absorbers of thermal (T), photovoltaic (PV) and photovoltaic/thermal (PVT) type. The first line shows the fin with pipe type for water heating, the air duct for air heating and the photovoltaic type absorber. In the second line there are the hybrid PVT type absorbers for water heating, for air heating and also for water heating with additional glazing and thermal insulation.

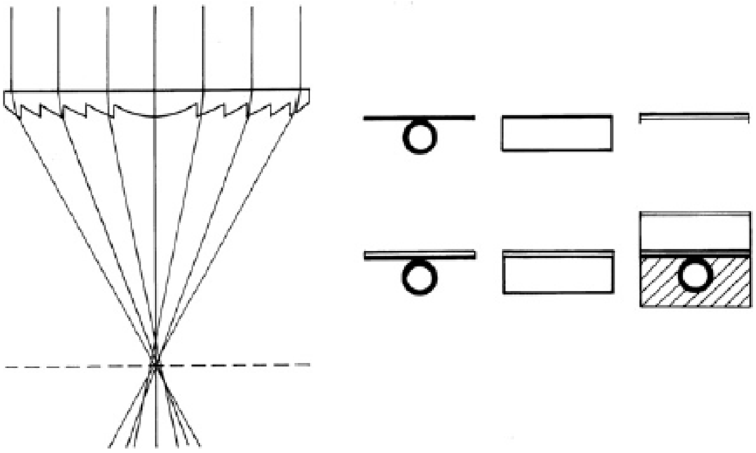

Figure 28. *The geometry of the Fresnel lens at left and alternative absorbers at right, for water heating, air heating, PV (up) and Hybrid PVT- water, PVT-air and PVT-water plus glazing (down).*

Garg and Adhikari (1999) demonstrated the use of several truncated CPCs in a single PVT module. They found that their collector for air heating, with a concentration ratio CR = 3, resulted in better efficiencies when integrated into a system. A similar system was also demonstrated by Othman [14] as shown in Figure 29:

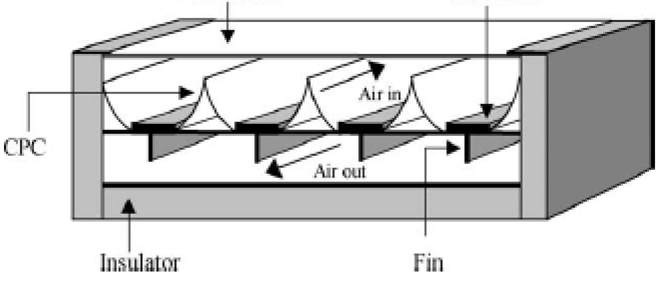

Figure 29. *The schematic model of a double – pass PVT collector with CPC and fins*

The absorber of this PVT collector consists of an array of solar cells for generating electricity, compound parabolic concentrator (CPC) to increase the radiation intensity falling on the solar cells and fins attached to the back side of the absorber plate to improve heat transfer to the flowing air. Air enters through the upper channel formed by the glass cover and the photovoltaic panel and is heated directly by the sun. Next it enters in lower channel formed by the back plate and the photovoltaic panel. The compound parabolic concentrators, concentrate solar radiation onto the PV cells. The fins on the back of the photovoltaic panel increases the heat transfer to the air and enhances the efficiency of the system. Figure 30 shows the effect of the mass flow rate on the efficiencies (photovoltaic, thermal and combined) of the PVT systems.

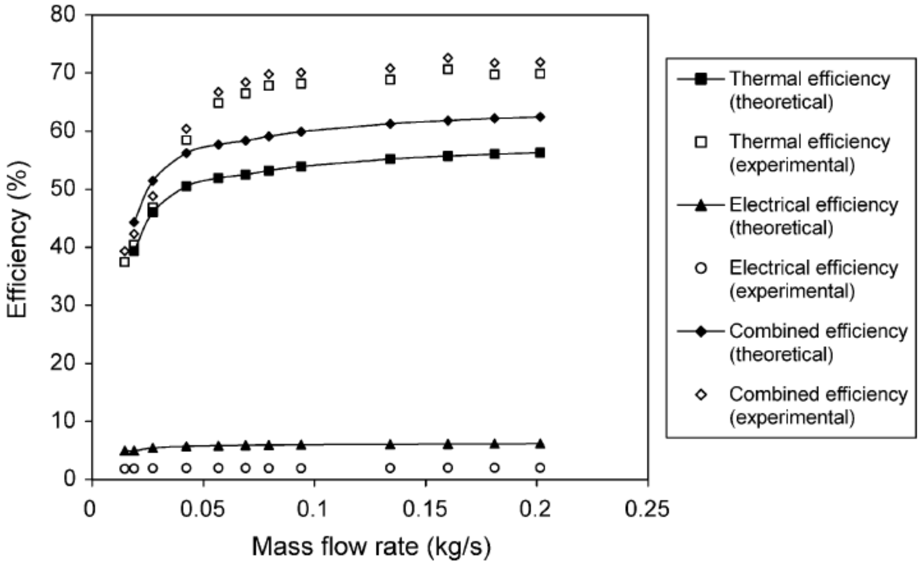

Figure 30. *The effect of mass flow rate on efficiencies at solar radiation of 500 [Wm^{-2}]*

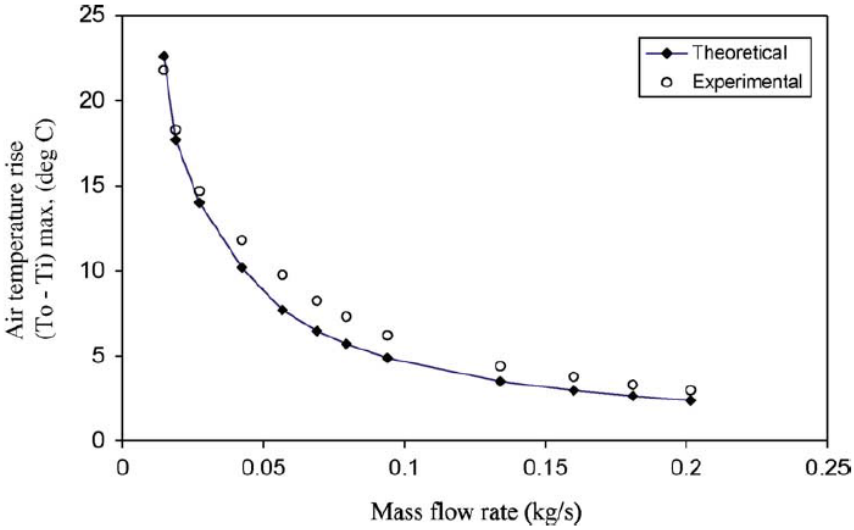

Figure 31. *Variation of maximum air temperature rise with air specific mass flow rate at radiation level of 500 [Wm^{-2}]*

In connection with Figure 31, it is obvious that as the air temperature rise gets less and less with increasing mass flow rate, the collector thermal efficiency gets correspondingly higher and higher due to the decrease in the average temperatures of the absorber plate and the glass cover, thereby reducing the top losses. Increasing the flow rate will increase the heat transfer coefficient between the channel walls and the working fluid, resulting in a lower mean photovoltaic cells temperature. This will increase the electrical efficiencies of the collector. However the enhancement in the value of electrical efficiency is remarkably very small as compared to the increase in the value of mass flow rate. Nevertheless from Figure 30 it shows some contribution of the electrical efficiency to the total efficiency of the system. The combined efficiency varies from 39 to 70% at mass flow rate of 0.015–0.16 [$kg \cdot s^{-1}$] and radiation intensity at 500 [$W \cdot m^{-2}$].

It has been observed that the experimental results were slightly higher than as predicted in mathematical model. This characteristic may be due to the effect of I radiation released by tungsten halogen lamps during the test. It has been seen in Figure 30 that the I radiation gave an impact to the electrical performance of the collector and reduced to 50% of the actual electrical energy produced meanwhile the thermal performance increased by 10% of the predicted value.

However, important concentration of solar radiation can also be achieved with compound parabolic concentrators (CPC). A typical arrangement of a CPC PVT [15] collector is shown in Figure 32.

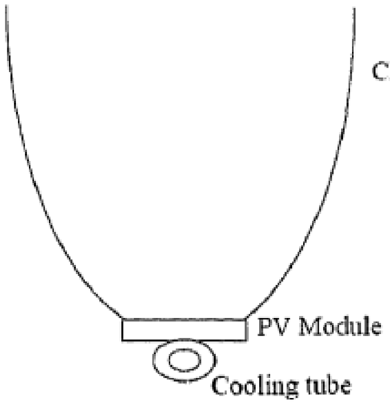

Figure 32. *CPC PVT collector.*

This PVT system consist of PV module mounted on focus of CPC and a cooling tube positioned below the PV module in which coolant fluid flows to remove heat.

Another system based on the same operation principle is the CHAPS (concentrating heat and power system); currently in use at one of the residential colleges at the Australian National University (ANU). This system, discussed by Coventry [16] , and the model of double pass PVT collector with CPC fins proposed by Othman are the most innovative among those available in the literature.

1.7.1 Performance of the CHAPS systems

The so-called combined heat and power solar (CHAPS) collectors consist of glass-on-metal mirrors that focus light onto high efficiency monocrystalline silicon solar cells to generate electricity. Water, with anti-freeze and anticorrosion additives, flows through a conduit at the back of the cells to remove most of the remaining energy as heat. The energy may either be shed through cooling fins, or be used via a heat exchanger for building heating and domestic hot water. The collectors are made up of 1.5 m long mirror and receiver modules, which are connected end-to-end to form a row. The first CHAPS prototype is a single trough, 15 m long, shown in Fig. 33.

Figure 33. *Prototype CHAPS collector at the ANU*

The solar cells manufactured by ANU (Fig. 34), are monocrystalline silicon cells designed to have low internal series resistance, since the high current density under concentrated radiation significantly affects the fill factor of the cell.

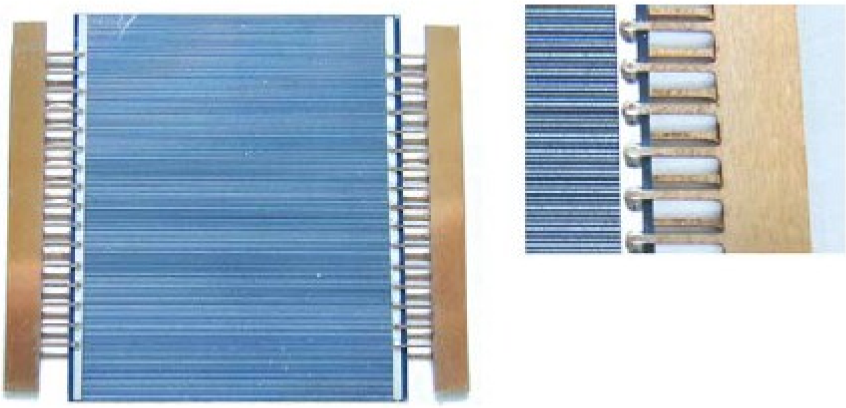

Figure 34. *ANU concentrator cell*

Also, the solar cells are bonded to an aluminium receiver with a thermally conductive, electrically insulating tape. They are connected in series and encapsulated with silicon and low-iron glass. The heat transfer fluid, which is water with anti-freeze and anti-corrosive additives, is pumped through the extruded aluminium receiver (Figure 35) to cool the cells and collect thermal energy. The back and sides of the receiver are insulated with 20 mm thick glass wool encased by a sheet aluminium cover. Internal fins have been incorporated in the fluid conduit to increase the heat transfer surface in order to minimize the operating temperature difference between the cells and the fluid.

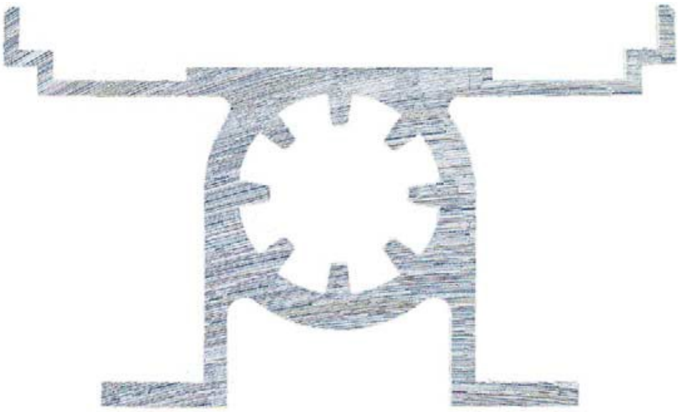

Figure 35. *Cross-section of the spine of the CHAPS receiver*

The reflective surface is a glass on metal laminate (GOML) composed of a silver backed mirror 1 mm thick, laminated to a sheet metal substrate. The mirror is held in its parabolic shape by stamped tab ribs at either end of the mirror. The mirrors are around 92% reflective, which compares well with other reflective surfaces such as anodized aluminium at 81% and the glass surface is highly scratch resistant when compared to some plastic film concentrators. The sun-tracking controller controls a linear actuator that is connected to a circular tracking wheel by cables. The tracking accuracy is set to ±0.2. Because of the stamped tab rib design, there are small gaps between the mirrors averaging around 19 mm.

Figure 36 shows the efficiency results for the receiver when it is operating both with and without an electrical load. T_f and T_{amb} are the mean fluid temperature and ambient temperature respectively.

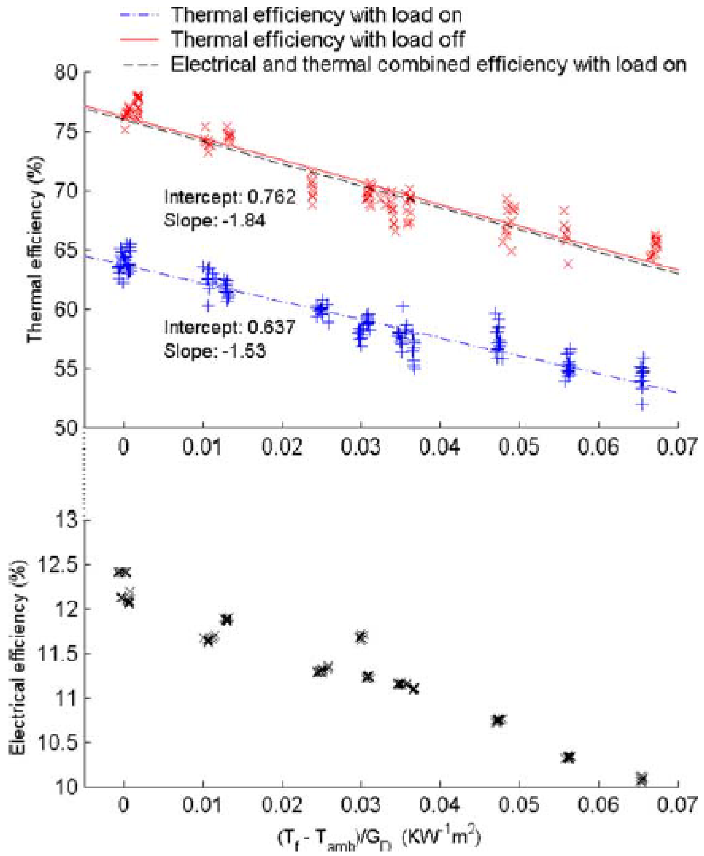

Figure 36. *Efficiency curves for the CHAPS receiver.*

The average wind speed across all tests was 0.21 [m·s^{-1}], with peak wind speed of 1 [m·s^{-1}]. The water flow rate varied between about 37.5 and 42.5 [ml·s^{-1}] between different runs, but usually within a 1 [ml·s^{-1}] range for a given run. While flow rate influences the heat transfer coefficient within the receiver, and hence the efficiency, calculations show the corresponding uncertainty in efficiency for this range of flows is around 0.3%. Similarly, the inlet temperature was normally very stable for a given run, within range of 0.3 °C. Direct beam radiation ranged between 829 and 928 [W·m^{-2}] and ambient temperature between 14.8 and 27.5 °C.

For the thermal efficiency plots, the measurement uncertainty combined with the variable wind conditions give uncertainty around 5.0%. The uncertainty in the electrical efficiency calculations is lower, around 2.2%.

In Figure 36, the electrical efficiency is plotted on the same horizontal axis in order to show the data points corresponding to the thermal efficiency data points. Addition of the electrical efficiency data to the thermal efficiency data (plotted in Fig. 36) yields a combined efficiency trend very similar to that of the thermal efficiency when there is no electrical load. However, the electrical efficiency depends on absolute temperature rather than temperature difference. To illustrate this point, the same data set plotted against the average fluid temperature shows a reasonably linear relationship (Figure. 37).

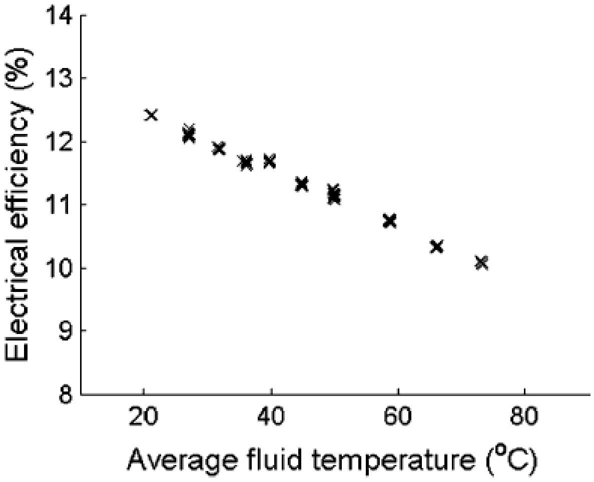

Figure 37. *Electrical efficiency for various fluid temperatures***.**

Under typical operating conditions such as fluid temperature of 65 °C, ambient temperature of 25 °C and direct radiation of 1000 [W·m^{-2}] the CHAPS collector has thermal efficiency of 58%. The electrical system efficiency is around 11% under typical operating conditions, which is equivalent to a good quality flat plate PV system under operating conditions. To make a direct comparison between the efficiency curves of the CHAPS collector with those of a typical flat plate collector, it is necessary to make an assumption regarding the ratio of direct beam radiation G_d to total global radiation G_t. Figure 38 shows a comparison between the chaps collector and a Solahart Oyster Ko collector

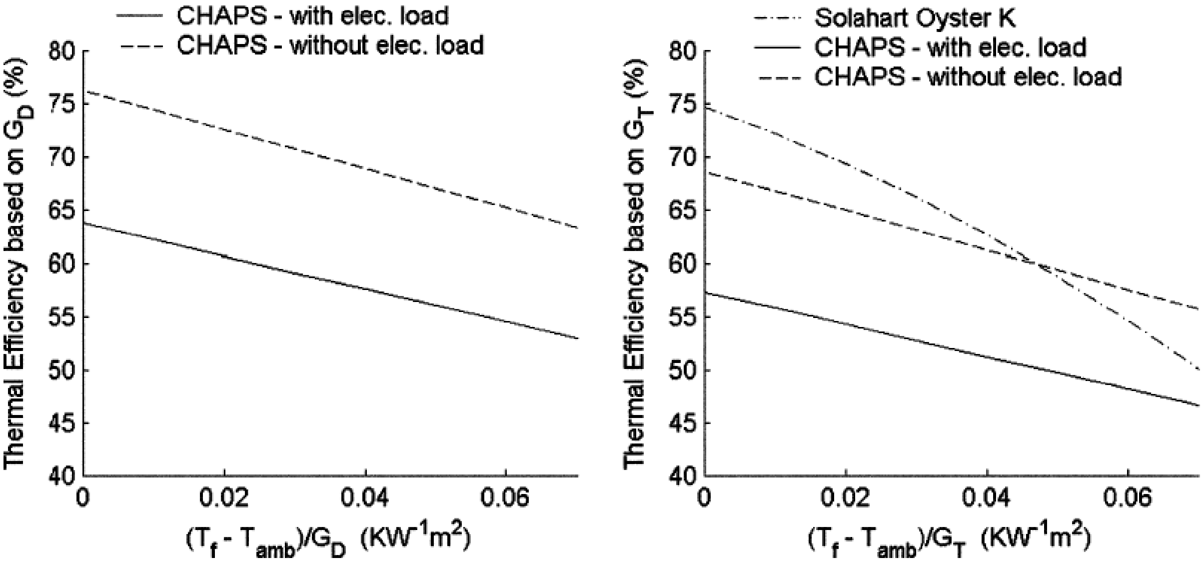

Figure 38. *Thermal efficiency of the CHAPs collector using direct radiation (left) and comparison with a flat plate collector using total (direct and diffuse) radiation (right).*

It is assumed for the sake of comparison that the direct radiation is 90% of the total radiation. The comparison in Figure 38 shows that at lower operating temperatures, a flat plate collector has a higher efficiency than the CHAPS collector, but that as the operating temperature rises, the gap in performance is reduced. Clearly the thermal losses increase more rapidly for a flat plate collector due to the larger surface area. However the comparison is only valid when the two collectors are oriented directly towards the sun a concentrating collector must track the sun, and therefore the efficiency does not suffer to the same extent as a flat plate collector due to reflection losses at higher incidence angles.

The CPC system has a concentration ratio of 37 and under typical operating conditions shows thermal efficiency around 58% and electrical efficiency around 11%, therefore a combined efficiency of 69% .

1.8 Techniques to increase PV/T performance

During the last few years, new design principles in energy conversion processes have been invented and applied for the PVT systems. In the following paragraph, a review of some more performing PVT technologies will be presented.

Tripanagnostopoulos carried out research on PVT systems and tested three design modes (Fig. 39) with a heat exchanger (HE) placed on PV rear surface (Mode A), in the middle of an air channel (Mode B), and on an air channel on the opposite surface (Mode C).

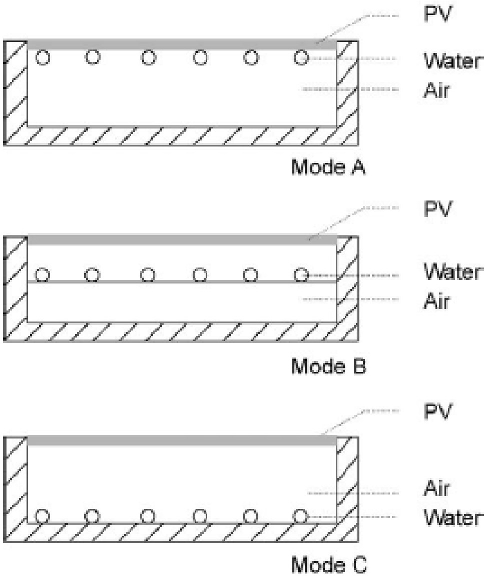

Figure 39 *Three modes of unglazed PVT modules.*

The results of the research show that the placement of HE at PV module’s rear surface gives optimum system thermal performance, both for water and air circulation. From the analysis of the three configurations it is possible to deduce that Mode A is an effective combination for the PVT system when engaged with the dual heat extraction operation.

A more effective heat transfer is obtained when the mean distance between heat generation and heat collection is minimal. Hence, in the second type of design shown in Fig. 40, the liquid is allowed to flow beneath the PV panel through multiple channels to withdraw the heat generated by the PV cells.

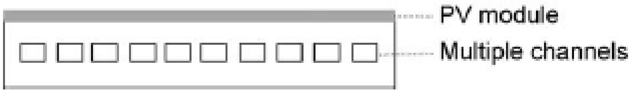

Figure 40.*Channel PVT concept with liquid flow beneath the PV cells*

These channels are formed using plastic sheet by extrusion. This geometry is better suited to withstand water pressures in the channels than in the case of one broad channel. Plastics, however, have a relatively large coefficient of thermal expansion. Hence, it becomes challenging to ensure proper connection between channel material and PV cells. Another similar type of PV module based on same concept is the following:

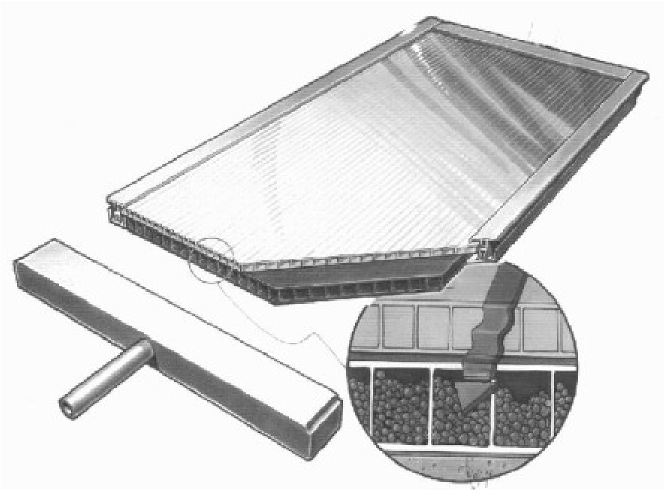

Figure 41. *The absorber PPO plastic contains internal, wall to wall channel filled with ceramic granulates*

Here, the absorber plate contains internal, wall-to wall channels filled with ceramic granulates. The fluid (water) flows through the parallel absorber channels, fills the vacant space between the ceramic particles and is brought in contact with the top absorber sheet, enabling good heat transport from absorbing surface to heat carrier fluid. The fluid flows in the square wall-to-wall channels covers the entire back of the absorber surface, resulting in a uniform temperature distribution across the width of the absorber.

To enhance the performance of PVT air collectors several geometry can be placed between the PV module and the opposite channel wall. Roughening the opposite channel wall with ribs or/and using wall surface of high emissivity, which is considerably a low cost air heating improvement, has also been adapted (Fig. 42 a). In addition, corrugated sheet inside the air channel along the air flow can be attached on PV rear surface as well as on the opposite channel wall surface (Fig. 42 b). An alternative modification is to put lightweight pipes along the air flow in the air channel, with slight elasticity to ensure satisfactory thermal contact with PV rear surface and channel wall (Fig. 42 c). These pipes are heated by conduction, convection and radiation from PV rear surface, which can contribute to air heat extraction, avoiding the undesirable increase of opposite channel wall surface temperature.

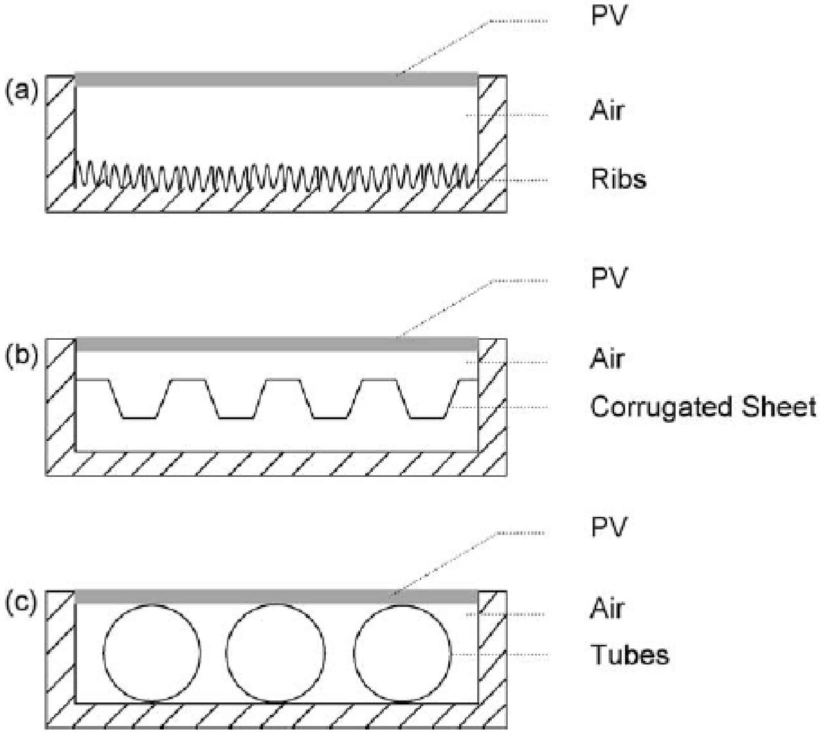

Figure 42. *Improvement of heat extraction of the PVT air system with (a) ribs,(b)a corrugated sheet and (c) tubes.*

To improve heat transfer in the air channel of an air PVT systems there are numerous methods such as the use of fins attached to the PV rear surface or wire mesh in the air channel providing air circulation on both front and rear surfaces of the PV module. The cross-sectional views of their models are shown in Fig. 43:

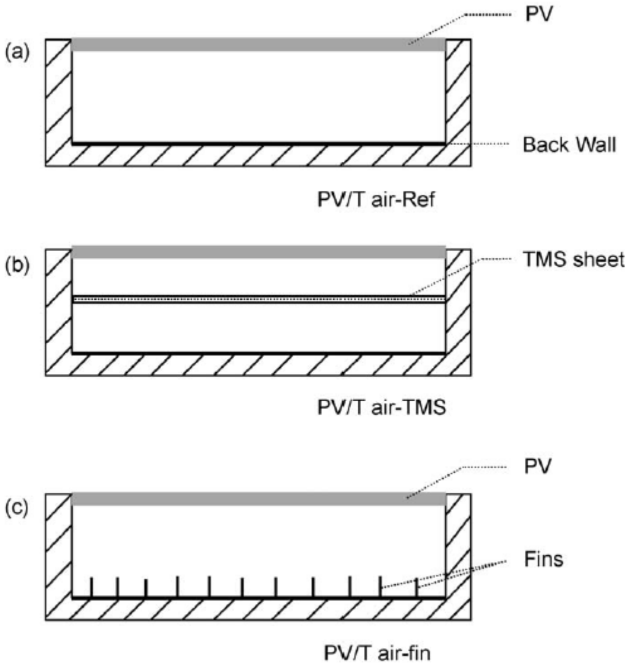

Figure 43. *Cross-sectional view of PVT air collector models*

Fins of 1.5 and 4 cm of profile using aluminum and galvanized iron, respectively, were used to form fin plate elements. The fins were positioned such that their vertical surfaces were parallel to the air flow, resulting in an increase in the heat exchanging surface area in the air channel. Further, the fins were selectively coated to improve emissivity on the thermal performance of the system. It was observed that the larger the fin area, the higher the temperature drop experienced at the PV module surface. Typically, the values were about 2–4°C for a fin profile of 4 cm.

Apart from using fins in the air channel duct, attempt was made to use metallic cylindrical tubes, using 0.5 mm thick aluminum sheet. Tubes were installed along the air channel pressed fit by PV rear surface and opposite wall surface of the air channel duct. The results of this study carried out that though the temperature drop at the PV laminate surface is not much higher compared to the system using fins, it has better advantage since the back wall temperatures are much lower.

In addition to the above modifications described, Tripanagnostopoulos combined the advantages of TMS PVT, formed by suspended thin aluminum sheet (0.1mm tick), with ribis of about 5mm on the opposite channel wall. The ribs were further painted black to increase the heat transmittance by radiation from TMS back surface to air channel wall Fig.44

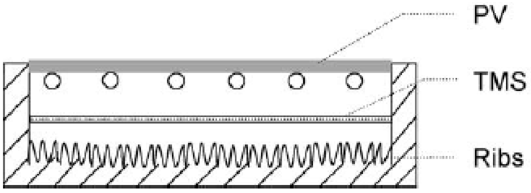

Figure 44. *Cross sectional of the modified PVT dual solar systems provided with TMS and ribs*

This method is particularly promising and cost effective not only in terms of heat transfer, but also the fabrication, installation and material costs are much lower for the above mentioned simple plate geometry compared to other designs.

Confirming the improvement of system's thermal performance Tripanagnostopoulos realized a new model design and integrated the mentioned modification with using two metallic plates instead of a single sheet to increase the heat transfer area by four folds (Fig.45). The study showed that the system could obtain a maximum thermal efficiency of about 45% and 55% for air heat extraction and water heat extraction mode, respectively.

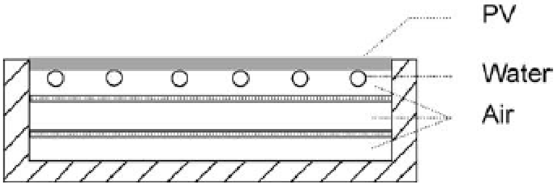

Figure 45. *Modified PVT dual systems provided with two TMS*

References

[1] M.Arif Hasan, K Sumathy . Photovoltaic thermal module concepts and their performance analysys:A review. Renewable and sustainable Energy Reviews.

[2] Kamran Moradi, M.Ali Edadian, Cheng-Xian Lin. A review of PV/T technologies: Effects of control parameters. International Journal of Heat and Mass Transfer 2013

[3] H.A. Zondag, D.W. de Vries, W.G.J. Helden , R.j.C. van Zolinger, A.A. van Steenhoven. The yield of different combined PV-thermal collector designs. Solar Energy 2003.

[4] K. Sopian, K.S. Ygit, H.T. Liu, S. Kakac and T.N.Veziroglu. Performance analysis of photovoltaic thermal air heaters. Elsevier science 1996.

[5] Adel A. Hegazy. Comparative study of the performances of four photovoltaic/thermal solar air collectors. Energy conversion e Management (2000)

[6] Arvin Tiwari, M.S. Sodha. Parametric study of various configurations of hybrid PV/thermal air collector: Experimental validation of theoretical model. Solar Energy Materials and Solar Cells 2007

[7] T:T.Chow, J.W. Hand, P.A: Strachan Building- integrated photovoltaic and thermal applications in a subtropical hotel building. Applied Thermal engineering 2003.

[8] B.J. Brinkworth, B.M. Cross, R.H. Marshall, Hongxing Yang. Thermal regulation of photovoltaic cladding. Solar Energy 1997

[9] M. Posnansky, S. Gnos. The importance of hybrid PV-Building integration. Atlantis energy LTD.

[10] B. Sandnes, J. Rekstad. A photovoltaic/ thermal (PV/T) collector with a polymer absorber plate. Experimental study and analytical model. Solar Energy 2002.

[11] Y. Tripanagnostopoulos and M. Souliotis. Application aspects of hybrid PVT solar systems

[12] Rosell JI, Vallverdu X, Lechon MA, Ibanez M. Design and simulation of a low concentrating photovoltaic/thermal system. Energy Conversion and Management 2005;

[13] Y. Tripanagnostopoulos, Ch. Siabekou, J.K. Tonui The Fresnel lens concept for solar control of buildings. Solar Energy 2007.

[14] Mohd. Yusof Hj. Othman, Baharudin Yatim, Kamaruzzaman Sopianb, Mohd. Nazari Abu Bakar. Performance analysis of a double-pass photovoltaic/thermal (PV/T) solar collector with CPC and fins. Renewable Energy

[15] Johan Nillson Optical Design and Characterization of Solar Concentrators for Photovoltaic

[16] Joe S. Coventry. Performance of a concentrating photovoltaic/thermal solar collector. Solar Energy 2005

CHAPTER 2

Preliminary Analysis to design a water PVT collector

2.1 Introduction

In the context of a national scientific research project, a prototype of water PVT collector has been designed, to be integrated into prefabricate concrete, suitable for roofs of industrial buildings. In this chapter, a preliminary analysis is carried out to determine the size of the cross section, the depth of the water duct, and the thickness and the material of the absorber-plate to maintain the overall performance at a satisfactory level. By means of a thermo-fluid dynamic modeling software "Comsol Multiphysics" it was also possible to determine the temperature distribution throughout the PVT collector. To the success of this project, two well-known companies, Sicep and ST Microelectronics, attended as partners. They processed the implementation of the reinforced concrete modules and PV panels, respectively.

2.2 Cross section of the water PVT collector

Following an extensive bibliographic investigation, it was found that the heat recovery by means of water allows, compared to the case where the air is used, a reduction of the volumes and better efficiency. In addition, the water can be stored in suitable tanks and then used in many applications: environmental heating and cooling (by means of absorption refrigeration machines), medical uses. Thus, after choosing the type of coolant fluid, attention was focused on the geometry of the heat exchanger for the recovery of waste heat. Between the various design solutions proposed in the literature for water PVT collector, the "sheet-and-tube" was initially considered, but this configuration was soon overcome because the welding between the tubes and the absorber plate would have led to problems of practical realization, and also because the contact with the absorber plate occurs only for a quite limited area, thus not improving the heat exchange. So, to increase the contact surface, the channels will be made with rectangular or square section.

After that, a preliminary analysis has been conducted to determine the velocity field expected within the channels for the water distribution. As a general rule, to obtain efficient heat transfer, it is necessary to have high speed, such as to induce high values of the convective heat transfer coefficients.

As a reference, the water velocity inside the channels for a typical solar collector should vary in the range of 0.1 - 0.5 $m \cdot s^{-1}$.

At such velocity values a flow field is usually established in the turbulent regime. Velocity values less than 0.1 $m \cdot s^{-1}$ are considered insufficient to ensure an efficient heat transfer. So the fluid velocity value is a significant parameter, and it depends on other conditions such as the cross section, its size and shape and the fluid flow rate.

The latter parameter, in the design practice of solar thermal systems, is limited to a rather narrow range. Characteristic values are in fact between 40 and 100 $l \cdot h^{-1}$ per unit absorbing area: these values are suitable to ensure a temperature variation, between the input and output channel section, about 4-5 °C.

To this regard, the following example may be useful. The average solar radiation incident on a solar panel can be assumed to be I_{sol} = 800 $W \cdot m^{-2}$ in a sunny day. Considering an average thermal efficiency of $\eta = 50\%$ the temperature difference Δt obtained can be calculated as follows:

$$\Delta = \frac{\quad}{\rho \cdot \quad \cdot \quad}$$

Here, ρ = 1000 $kg \cdot m^{-3}$ is the density of water, c_p = 4186 $J \cdot kg^{-1} K^{-1}$ is its specific heat. Assuming flow rate values equal to Q_w = 40 and 100 $l \cdot h^{-1} m^{-2}$, temperature differences Δt = 8.6 and 3.5°C are reached, respectively. These evaluations show that increasing the value of the flow rate implies a real detriment in the use of thermal waste recovered.

Figure 1 shows the first design solutions where the channels of moderate height were made with polyethylene to be fixed, by means of a special glue with high thermal conductivity, to an aluminum absorber plate of 1 mm thickness.

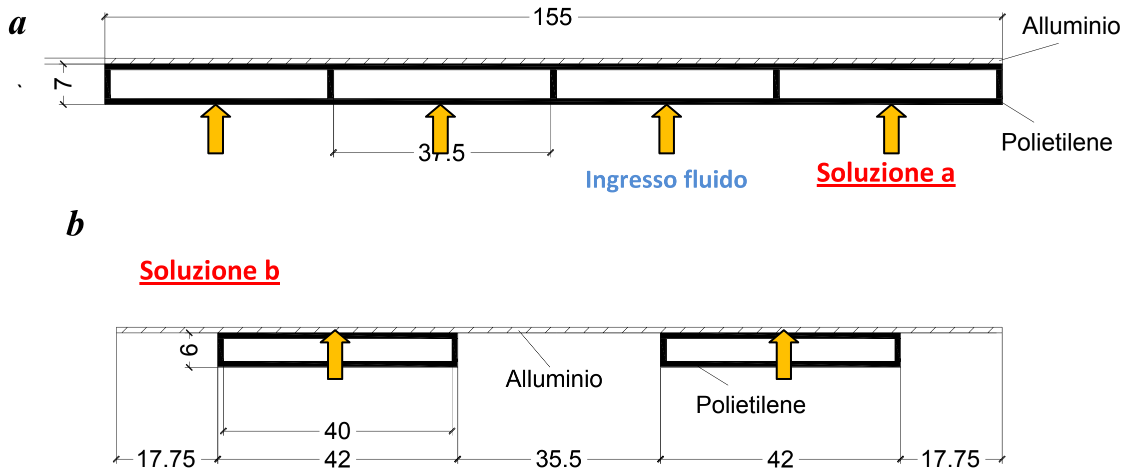

Figure 1 –*Cross Section of two absorber plates to recover the thermal waste – first solutions analyzed*

The absorber should be made up of elementary modules of width 155 mm and length 3 m, hydraulically connected to the bottom side. The solution ***a*** would offer the advantage of greater contact surface between the absorber plate and the channels, while in the solution ***b*** the channel number, at equal flow rate, is reduced to increase the fluid flow velocity. The solution ***b***, thanks to the high thermal conductivity of the aluminum plate that acts as a fin, allows a good heat transfer to water.

	40 [$l\cdot h^{-1}\cdot m^{-2}$]	**100 [$l\cdot h^{-1}\cdot m^{-2}$]**	**unit**
Soluzione a	0.01	0.025	[$m\cdot s^{-1}$]
Soluzione b	0.02	0.05	[$m\cdot s^{-1}$]

Table 1 – *Fluid flow (in m/s) for the solution analyzed in Figure 1.*

As shown from the results of Table 1, the velocity of the fluid inside the channels is excessively low in both cases. In particular, among the two configurations the solution ***b***, with flow rate of 100 [$l\cdot h^{-1}$ m^{-2}], achieves velocity around 0.05 [$m\cdot s^{-1}$], therefore well below the acceptable range previously introduced (0.1 - 0.5 [$m\cdot s^{-1}$]). Thus, to increase the velocity one should start from the solution ***b***, and reduce the height or the width of the channels: in the first case, however, one would get a too elongated shape, hydraulically inappropriate, whereas in the second case the excessive distance between the channels could reduce the absorbing surface area. Taking account of these considerations, at equal flow, it is preferred to increase the number of ducts and to reduce their section to rise the fluid flow velocity. So the solution considered more appropriate is represented in Figure 2:

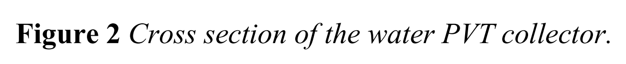

Figure 2 *Cross section of the water PVT collector.*

In more detail, the designed system is composed of stainless steel absorber plate of 0.6 mm thickness, on which photovoltaic cells are applied by lamination. The ducts are applied in the rear absorber surface, and are also made of stainless steel, with a square section having the outer side a = 10 mm and thickness δ_c = 1 mm; the distance between the channels is 78.6 mm and the length of the plate is 2966 mm.

Flow rate	**40 [$l\cdot h^{-1}\cdot m^{-2}$]**	**60 [$l\cdot h^{-1}\cdot m^{-2}$]**	**80 [$l\cdot h^{-1}\cdot m^{-2}$]**	**100 [$l\cdot h^{-1}\cdot m^{-2}$]**
Velocità [$m\cdot s^{-1}$]	0.08	0.12	0.16	0.2
Reynolds [-]	1303	1954	2606	3260

Table 2 – *Results of the solution shown in Figure 3.*
(Reynolds number is evaluated at 50°C)

From the results shown in Table 2, it is understood that the solution of Figure 2 can be regarded as appropriate, according to the criteria previously introduced, for flow rate not lower than 60 $l\cdot h^{-1}m^{-2}$. Within each channel belonging to the module, the water flows in the same direction. The module will then be joined by another similar module in which the water runs in reverse direction, in order to have the delivery and return manifold positioned on the same side of the PVT collector, to facilitate the installation and the hydraulic connections.

2.3 Absorber plate material

In a PVT system, the absorber represents the main functional component, which collects the incident solar radiation and transfers it to the coolant fluid, minimizing the losses to the outside and through the casing. Its thermal capacity must not assume too high values in order to allow fast reaction times in relation to the variable irradiation conditions and to optimize the possibilities of available energy use, even to low quantities. From the thermal point of view the main absorber features are:

- high absorption coefficient $\boldsymbol{\alpha}$ in the solar spectrum;
- low emissivity $\boldsymbol{\varepsilon}$ in the infrared spectrum,
- good thermal conductivity ;
- good heat transfer coefficient of the coolant fluid ;
- low thermal capacity;

On the other hand, the absorber plate must assure stability and reliability in time as well as mechanical resistance to stress, maintenance of optical properties in the long term, stability under high temperatures, limited weight, impregnability with respect to oxidation and corrosion processes. In order to meet the needs identified, it is generally realized by means of a copper or aluminum or stainless steel foil with thickness generally ranging between 0.15 and 2 mm; depending on the material. The main features associated to the materials used are shown in Table 3:

Absorber plate material	**Thickness δ [mm]**	**Weight per unit area [kg·m^{-2}]**	**Thermal conductivity λ [W·m^{-1}K^{-1}]**	**Thermal Capacity c_p [J·kg^{-1}K^{-1}]**
Copper	0.3	2.5 - 3	386	350
Aluminum	0.6	2	164	900
Steel	2	15-20	50	450

Table 3. *Thermo-physical properties of Copper, Aluminum and steel.*

Considering that the water PVT collectors are integrated in reinforced concrete modules for buildings roofs, their weight could be an important problem given the collector sizes, in fact their length and width are L = 2966 mm and H = 1237 mm, respectively. Taking into account these project benchmarks, copper, as shown in table 3, has the most appropriate thermo-physical properties; however its cost is high, so the material choice falls back on aluminum or steel. Aluminum, being a lightweight and malleable material but less expensive than copper, was the solution proposed by this research team; in any case Sicep pointed out that, due to constructive and technical-economic reasons, they would have preferred to realized the collector prototype with an absorber plate made of steel (thickness of 0.6 mm). Subsequently, to test the performance of the whole system a multi-physics analysis was carried out by means of Comsol software, as explained more in detail in paragraph 2.5.

2.4 Fin efficiency and distance between the channels

Once designed the duct section of the absorber plate, it is important to define what is the optimal distance between the channels to ensure a performing operation of the PVT system. To this purpose, it is necessary to introduce the concept of "*Fin efficiency*" **F** [3], that takes into account the mode of heat distribution within the fin shown in Figure 3:

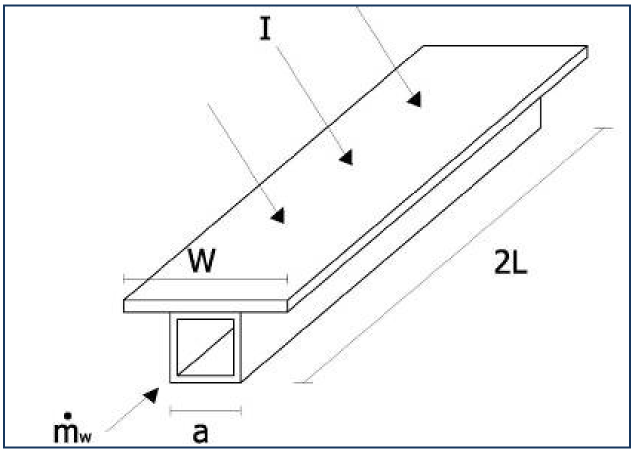

Figure 3. *Fin*

The F value depends on the geometrical and thermo-physical properties of the absorbing plate as shown by equation (1):

$$F = \frac{\tanh\left(m \cdot \frac{W-a}{2}\right)}{m \cdot \frac{W-a}{2}} \qquad \text{with:} \quad m = \sqrt{\frac{U_L}{\lambda_r \cdot \delta_r}} \tag{1}$$

In particular U$_L$ represents the overall heat transfer coefficient of the PVT collector determined by the equations (2), (3), and (4):

$$U_L \approx U_f \cdot \left[1 - (\psi - 45) \cdot (0.00259 - 0.00144 \cdot \varepsilon_p)\right] \tag{2}$$

$$U_f = \frac{1}{\frac{1}{h_{c,v}} + \frac{T_p}{344}\left(\frac{T_p - T_a}{f}\right)^{-0.31}} + \frac{\sigma\,(T_p + T_a)(T_p^2 + T_a^2)}{\frac{1}{\varepsilon_p + 0.00425\,(1 - \varepsilon_p)} + \frac{f + 1}{\varepsilon_v} - 1} \tag{3}$$

$$f = 1.058 \cdot (1 - 0.04 \cdot h_{c,v} + 5 \cdot 10^{-4} \cdot h_{c,v}^2) \tag{4}$$

Here, T_p and T_a are the absorber plate and ambient temperature, respectively, and ε_v is the glass emissivity. Moreover, ψ and ε_p are the latitude and the emissivity of the absorber plate, respectively The equations (3) and (4) can be applied to a PVT collector with a single glass. In this context it is interesting to estimate the external convective coefficient, which can be calculated by equation (5) as a function of the wind speed *w:*

$$h_{c,v} = 5.7 + 3.8 \cdot w \tag{5}$$

As shown in Figure 4, the fin efficiency F, while maintaining the other parameters constant:

- decreases with the increase of the overall heat transfer coefficient and the distance W between the tubes;
- increases with the thermal conductivity λ_p of the absorber plate material and the diameter D of the tubes;
- increases with the thickness δ of the absorber plate;

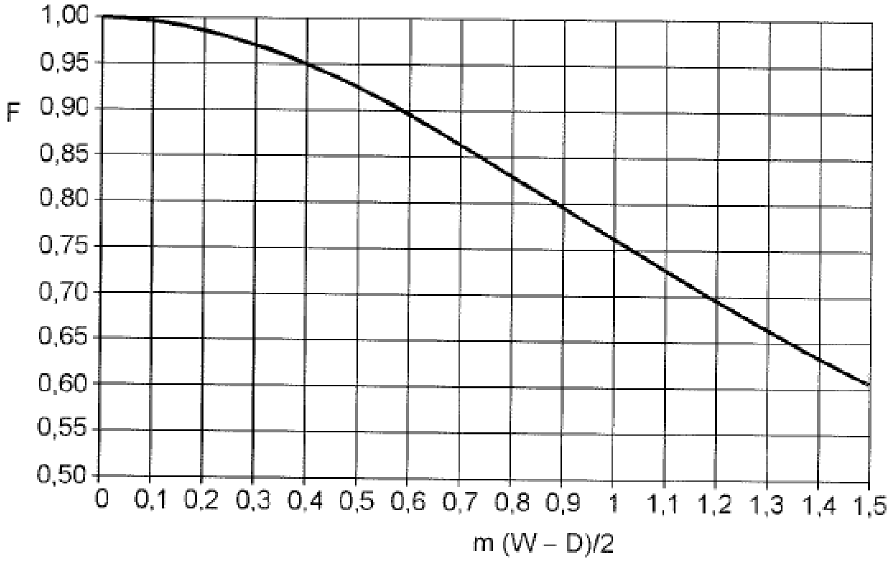

Figure 4. *Fin efficiency*

As a general rule, it can be stated that in collectors of good quality level the factor F ranges approximately between 0.8 and 0.98. Since the F value affects the overall efficiency of the water PVT collector, the above comments provide useful information on the design, on the most appropriate choice of the absorber plate, and on the channel number applied in accordance with the limitations imposed by technical and economical assessments about the actual feasibility of various tested solutions. In this case, the calculation of F for the section shown in figure 3 provides a value very close to 1 that ensures a good thermal efficiency.

A parametric analysis was subsequently conducted, by varying the number of pipes to evaluate their effects on the performance of the PVT system. It consisted of three case studies, with variable number of tubes from six to ten (Figure 5). These simulations were performed in all cases proposed with water flow rate of 80 $l \cdot h^{-1} m^{-2}$.

The three configurations provide very similar performance, therefore the final choice fell on the panel with six tubes also considering the possibility of constructive and technical-economic feasibility.

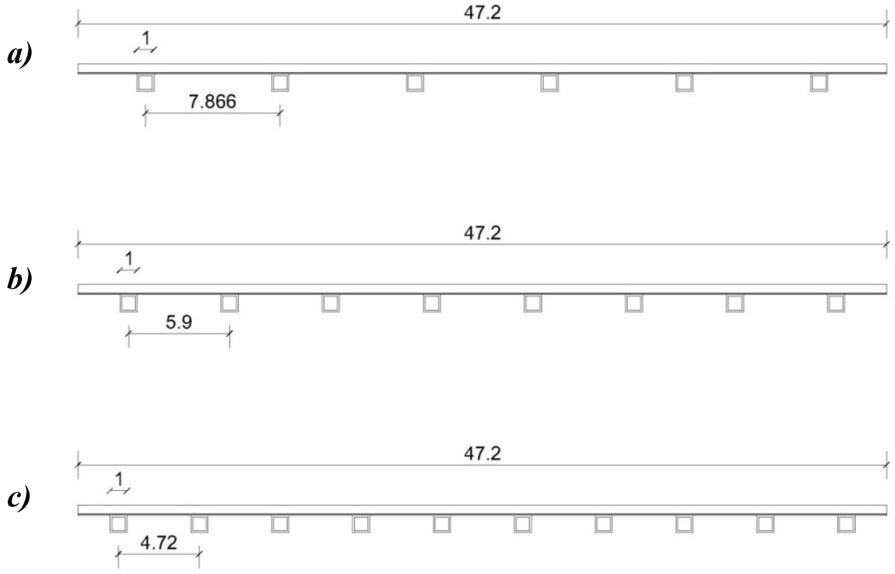

Figure 5. *Three different cross sections of a water PVT collector*

2.5 Introduction to Comsol Multiphysics software

Comsol Multiphysics [4] is a powerful interactive environment for modeling and solving all kinds of scientific and engineering problems based on partial differential equations (PDEs). With this software, it is possible to easily extend conventional models for one type of physics into multi-physics models that solve coupled physics phenomena simultaneously. When solving the PDEs Comsol uses the proven finite element method (FEM). It runs the finite element analysis together with adaptive meshing and error control using a variety of numerical solvers. In this software, like in the conventional FEM solver, it is conceptually possible to distinguish three different sections: preprocessor, processor and postprocessor. In the preprocessor section one draws the solid model, chooses the materials to be assigned to the various elements, discretizes the space continuous in finite elements generating a mesh, and applies the boundary conditions referring to the examined problem. In the second section one establishes the calculation parameters. The last section instead permits to postprocess the results obtained by the simulations and to view them by means of graphs. In order to determine the temperature distribution on the whole PVT device it is necessary to draw a 3D geometric model, as the temperature gradient in the flow direction is not negligible. The water PVT collector is composed by 6 fins, but the analysis can focus on only one of them, since they all have the same thermo-fluidynamic behavior. Comsol also includes a parametric CAD: this means that it can repeat the calculations by changing the value attributed to a certain number of geometric variables.

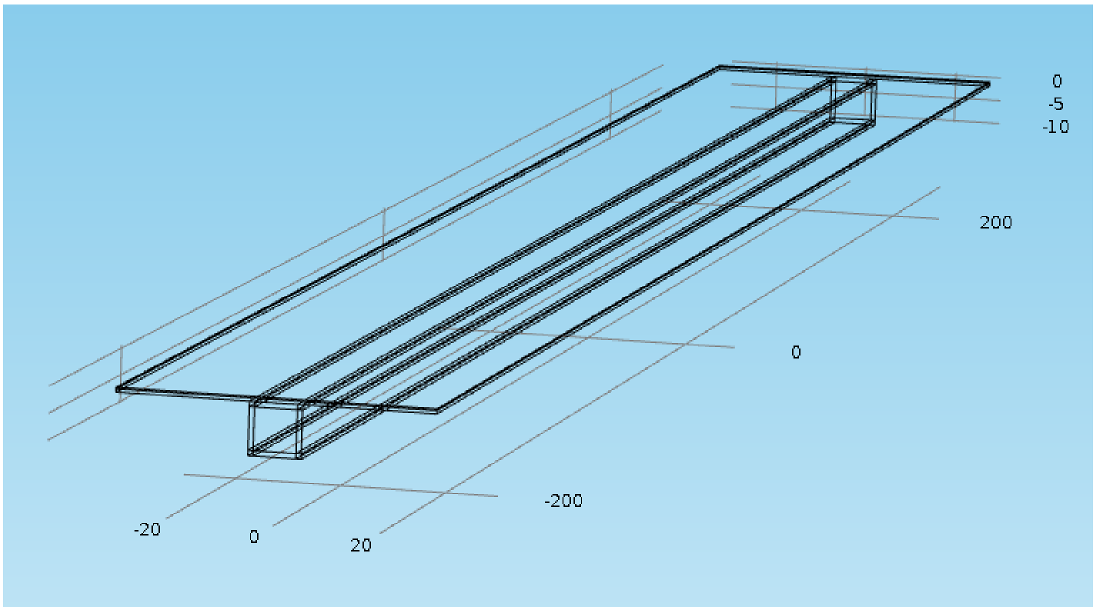

Figure 6. *3D model of PVT collector*

Figure 6 shows the 3D model used for the simulations. After drawing the geometry, it is possible to assign the material to different domains. Then, the model is discretized into elements, thus generating a mesh. In order to find a good compromise between quality of the results and computation time, that depend heavily on the mesh quality, for each fin component a different mesh was generated in relation to its shape. Thus, the water channel was discretized by means of tetrahedral elements but with different mesh strategies. In the first case, predefined mesh element sizes of type *Fine*r while to discretize water domain was used the *Boundary Layers* mesh tool that is a mesh with dense element distribution in the normal direction along specific boundaries and it is typically used for fluid flow. Instead, to mesh the absorber plate and the polycrystalline silicon layer, representative of the PV panel, a *boundary mesh* was generated on the absorber plate using triangular element, and then it has been extruded until the upper surface of the PV panel through the use of the sweep function. The whole geometric model was discretized in 116968 elements.

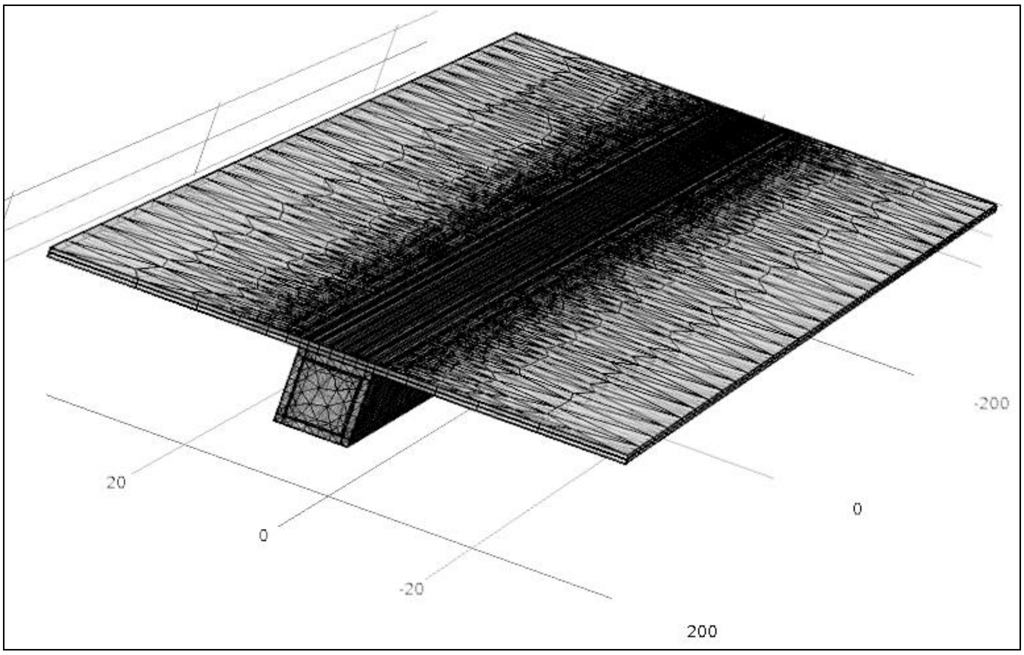

Figure 8. *Mesh generation*

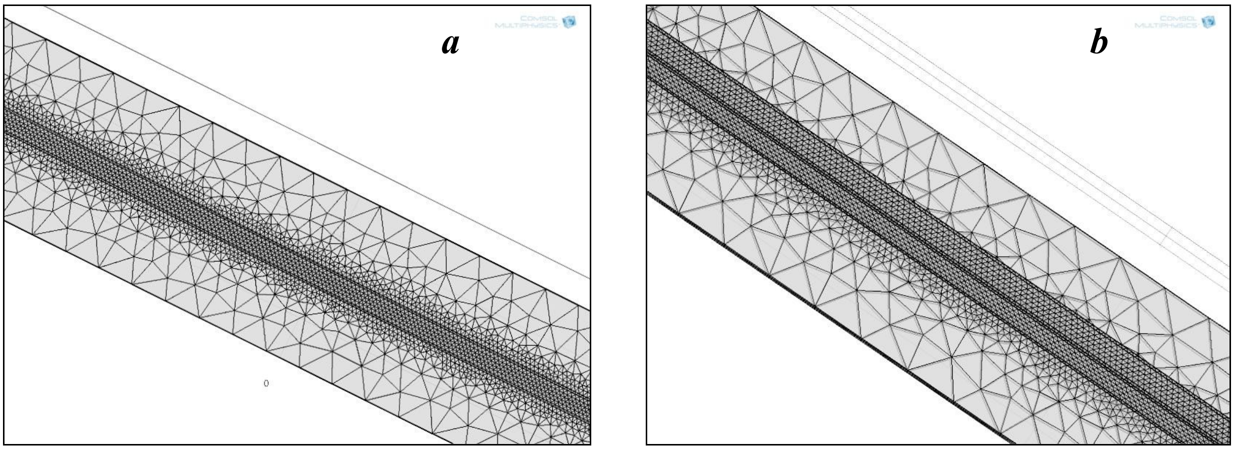

Figure 8. *Mesh details of upper a) and lower b) fin surface, respectively*.

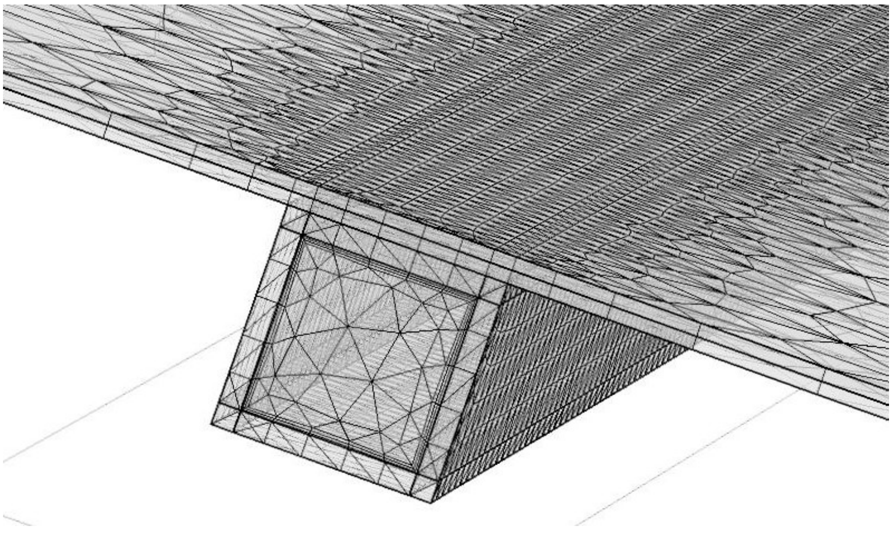

Figure 9. *Cross section mesh*

2.6 Governing Equations and Boundary conditions

All three modes of heat transfer are involved when considering a basic PV panel. Heat is transferred within the PV cell and its structure by conduction, and is transferred to the surroundings both by free natural convection and by long-wave radiation. Heat transfer by conduction to the panel structural framework is often ignored due to the small area of contact; in addition, the fins are thermally insulated as they are placed inside grooves designed on a polystyrene layer. The contact surfaces with the polystyrene layers are governed by the equation (6):

$$n \cdot (k \nabla T) = 0 \tag{6}$$

This boundary condition means that there is no heat flux across the boundary, as the domain is well insulated. This equation also states that the temperature gradient across the boundary is zero. For this to be true, the temperature on the side of the boundary must equal the temperature on the other side. Because there is no temperature difference across the boundary, heat cannot transfer across it. Figure 10 shows all boundaries that are considered insulated in the model.

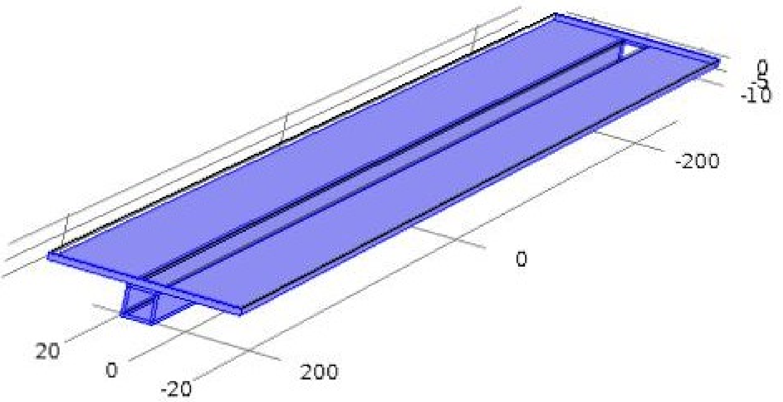

Figure 10. *Boundaries insulated*

The PV panel receives energy under the form of solar irradiance, converts a certain fraction of it into electricity through the PV effect, while the rest is transformed into heat. The aim of attaching the thermal panel underneath the PV cell is to remove as much heat as possible in order to increase the electric efficiency.

The FEA software being used in this study, COMSOL, contains a laminar flow and conjugate heat transfer physics module, which was used to model conduction heat transport within the cells as well as the convective heat transfer in the water channel on the backside of the PV panel. This package is appropriate for this study, because of the inhomogeneous temperature field that is created as water flows from the inlet to the outlet of the duct. COMSOL numerically solves the continuity and momentum equations, which are the governing equations for the fluid flow, as shown in equations (7) and (8) respectively:

$$\nabla \quad (\rho \quad) = \quad) \tag{7}$$

$$\rho \ \cdot \nabla \ = -\nabla \ + \nabla \ (\mu \ \nabla \ + \nabla \ ^{T} \ ) \tag{8}$$

The conduction-convection equation is also solved for the heat transfer in the flowing water, which is shown in Equation (9).

$$\rho \ _{p} u \nabla \ = \nabla \ (k \nabla \ ) \tag{9}$$

The fluid domain considered in this analysis is represented in Figure 11.

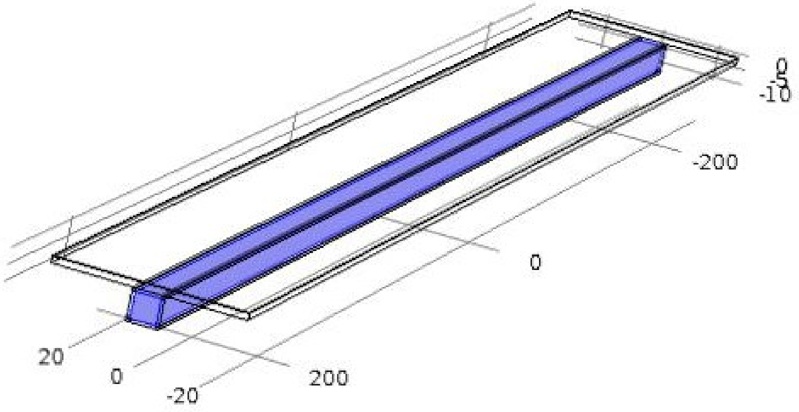

Figure 11. *Fluid domain*

To solve these equations, the inflow and outflow boundary conditions were also imposed, entering the flow velocity and the atmospheric pressure in the inlet and outlet cross section, respectively shown in Figure 12:

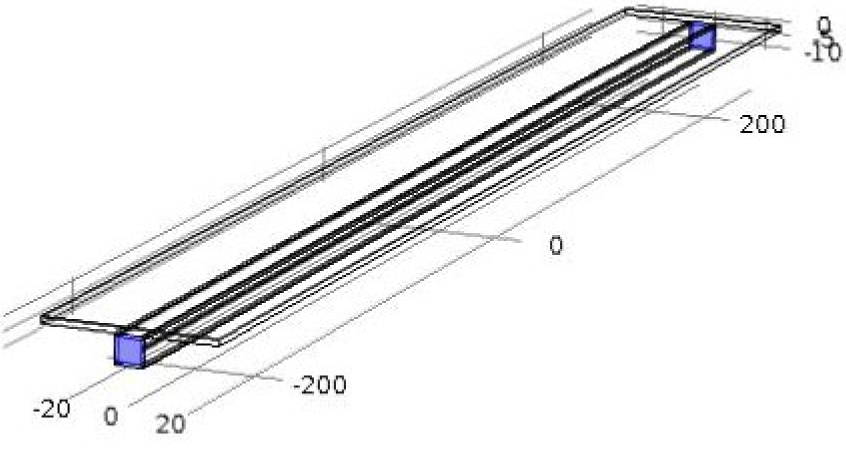

Figure 12. *Inlet and outflow boundaries*

Lastly, the long-wave radiation heat loss can be calculated from Equation (10) below:

$$q_{lw} = \varepsilon \; \sigma \; \left(T_{pv}^{4} - T_{amb}^{4}\right) \tag{10}$$

Also the convergence of the steady state solution was monitored throughout the simulation, resulting in around 50 – 60 seconds (real time) using the normal physics controlled mesh sequence setting.

2.7 Results

The simulations of the absorber with Comsol are aimed to understand what is the expected temperature distribution along the plate. Indeed, an appropriate solution should produce an uniform temperature distribution, thus avoiding local overheating and providing an effective heat removal. All simulations are solved in steady state, in which the conjugate heat transfer and laminar flow physics modules were utilized. In order to account for what underlined in section 2.2, three case studies are considered, distinguished as follows:

- *Case 1:* Aluminum absorber plate with thickness of 0.6 mm and W = 60 mm (distance between the centerline of two consecutive channels);
- *Case 2:* Steel absorber plate with thickness of 2 mm and W = 60 mm;
- *Case 3:* Steel absorber plat with thickness of 0.6 mm and W ranging from 60 to100 m.

In addition, other assumptions must be made to perform the simulations, such as the climatic conditions, the water flow characteristics, and other factors which impact this thermal analysis. In particular:

- The solar irradiance impinging on the entire surface of the PVT panel is 800 W·m^{-2}. However, in the simulation this value is reduced by a factor corresponding to the *transmittance-absorbance product* ***τα*** (see equation 12) as, for the sake of simplicity, the glass was not introduced in the construction of the model:

  $$\tau\alpha = \frac{\tau_{glass}\alpha_{abs}}{1-\left(1-\alpha_{abs}\right)\cdot\rho_{abs}} \tag{11}$$

  Here, the parameters $\tau_{glass} = 0.9$ and $\alpha_{abs} = 0.85$ and $f_s = 0.95$ are the glass transmittance and the absorber plate absorbance The $\tau\alpha$ value is equal to 0.74.
- No dust or any other agent is deposited on the PVT surface affecting the absorptivity of the PVT panel.

- The coolant fluid has an inlet velocity equal to 0.18 $\mathrm{m \cdot s^{-1}}$;
- The flow within the channel is considered to be fully laminar and incompressible.
- The ambient temperature surrounding the PVT panel is 293.15 K.

Furthermore, the water inlet temperature is assumed constant equal to 293.15 K, i.e. the same temperature specified for the ambient temperature. This water temperature was chosen to simulate a scenario in which the cooling water may reach ambient air temperature before entering the channel to carry heat away from the PVT panel.

In Figure 13, the velocity profile of the water in the flow channel is shown, as provided by the simulations. A similar laminar flow profile was achieved in each of the test cases. From this plot one can recognize the no-slip boundary condition invoked on the interior walls of the duct, as well as the parabolic flow profile that is created.

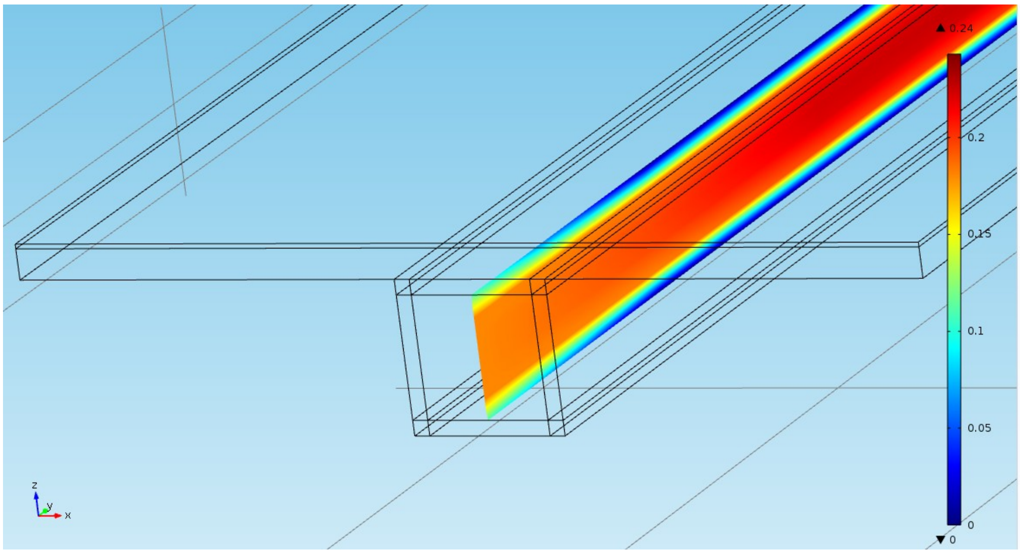

Figure 13 *Laminar flow profile common to all test case*

In Figures 14 and 15 , the three-dimensional plots for the steady state solution of the temperature distribution for test cases 1 and 2 are shown, respectively. These design solutions provide excellent fin efficiency values with rather uniform temperature distribution on the absorber plate. Both project proposals were rejected by Sicep because the first one is considered too expensive, and the second one results in an excessive weight.

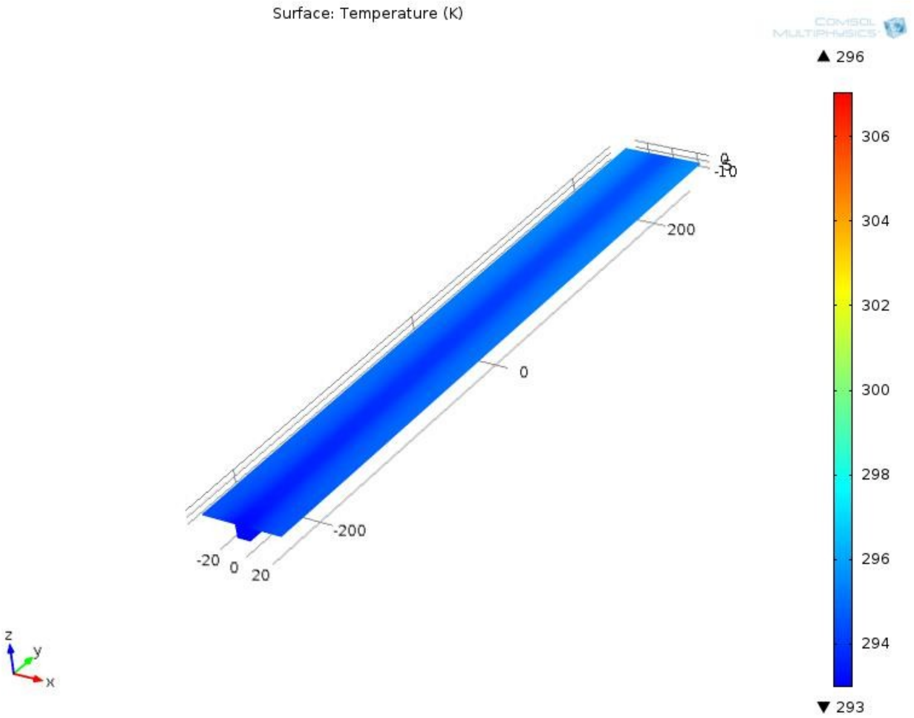

Figure 14. *Aluminum absorber plate with thickness δ=0.6 mm and W=60 mm*

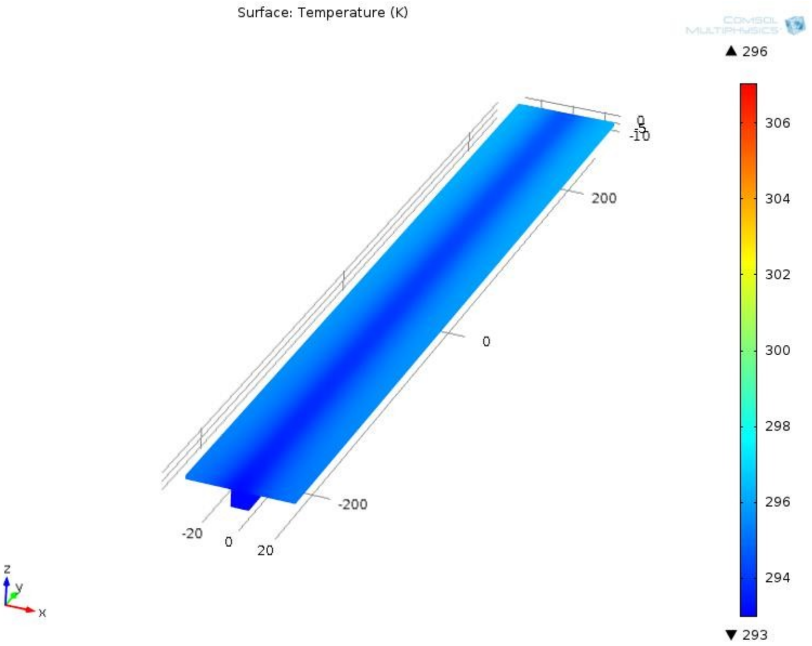

Figure 15. *Steel absorber plate with thickness δ=2 mm and W=60 mm;*

Finally, Sicep established that – irrespective of any consideration concerning the energy optimization of the absorber plate – it should be designed in steel with a thickness of 0.6 mm. Thus to determine which is the optimum distance between the channels that guarantees the best fin efficiency, three simulations were carried out in Comsol varying the parameter W. Figures 16, 17 and 18 show the temperature field for three different values: W = 60, W = 80 and W = 100 mm respectively.

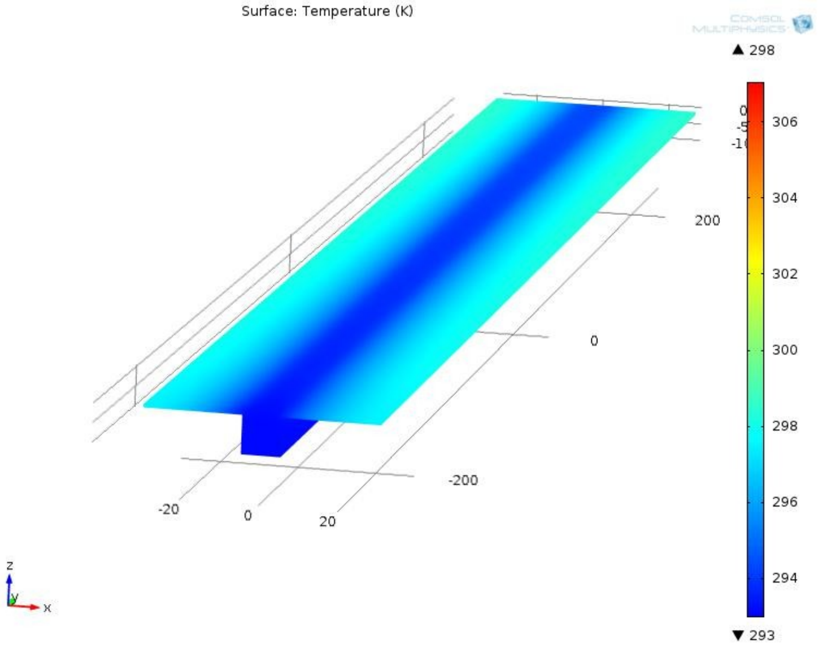

Figure 16. *Steel absorber plat with thickness δ=0.6 mm and W= 60 mm;*

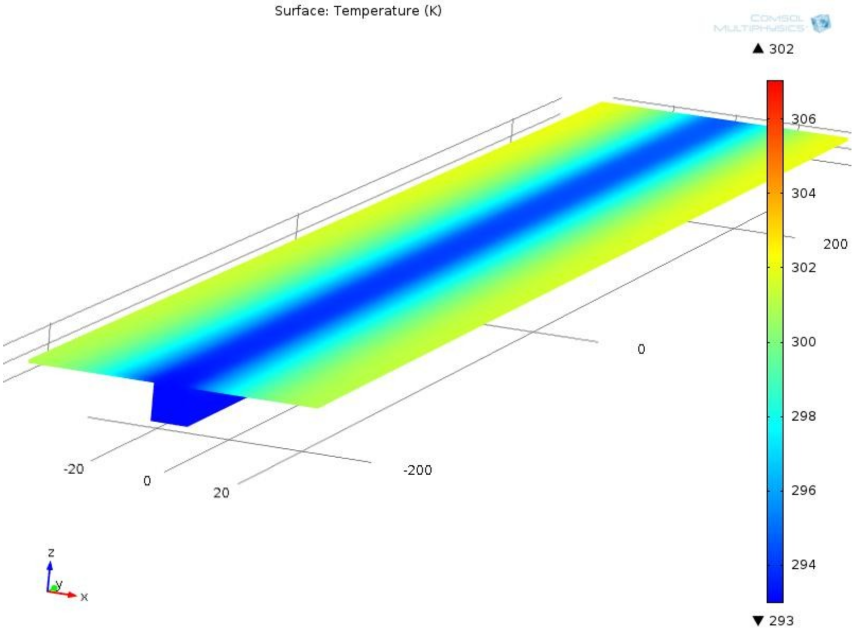

Figure 17. *Steel absorber plat with thickness δ=0.6 mm and W= 80 mm;*

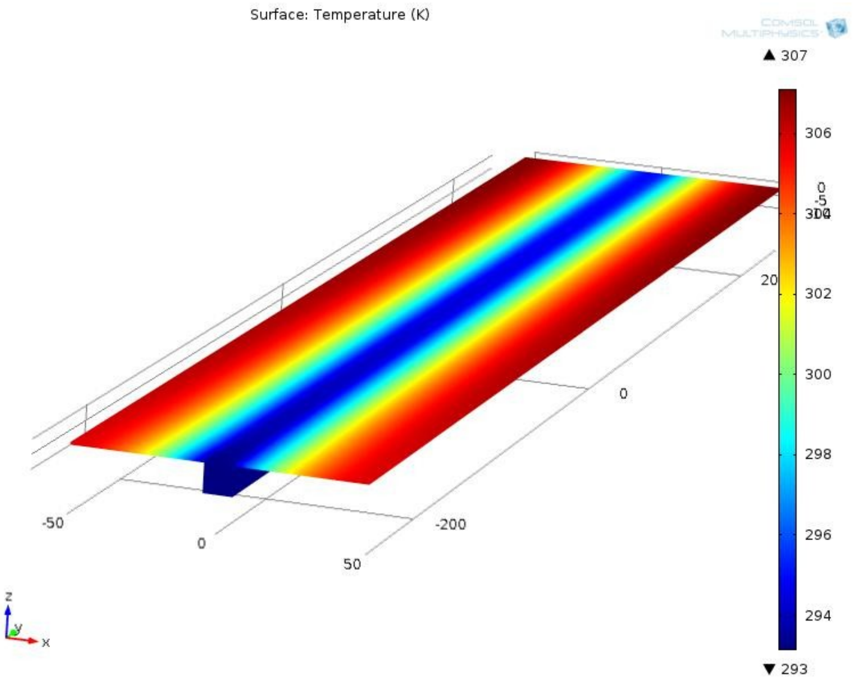

Figure 18. *Steel absorber plat with thickness δ=0.6 mm and W= 100 mm;*

The last three configuration studied provide increasing values of temperature gradient along their fins when increasing of W from 60 to 100 mm. Also, only the model shown in Figure 16 ensures a sufficiently uniform temperature distribution on the absorber plate, and consequently the best fin efficiency. Furthermore, for all the solutions here considered analyzed the temperature along the channel increases with the duct length of a few tenths of degree. In light of these considerations, the best configuration among the latter analyzed systems is the one that has the lowest W values, but the ultimate solution chosen by Sicep is that with W = 80 mm.

2.8 Description of Water PVT Prototype

In order to account for the results obtained from Comsol simulations and the measures imposed by Sicep, the final water PVT prototype consists of a thin absorber plate with a thickness $\delta_p = 0.6$ mm, on which a white backsheet is positioned, that has a protective function, with emissivity close to $\varepsilon = 0.9$, on which photovoltaic cells in polycrystalline silicon are ultimately laminated. The PVT collector thus formed is covered by a glass layer of thickness 3 mm. Under the absorber there are six channels, where water flows as a coolant fluid, made in stainless steel with square cross section, outer side 10 mm and thickness 1 mm. The channels are positioned on a polystyrene support suitably shaped, and they are equally spaced, with a distance between the two channel centerlines equal to W = 78.6 mm. Figure 19 shows this water PVT system, and it is possible to observe the inlet and outlet hydraulic connections of the heat transfer fluid, which are positioned on the same side of the PVT panel. In this way, the fluid flows within six parallel paths, each of length equal to twice the panel length, whose dimensions are: H = 1237 mm and L = 2966 mm.

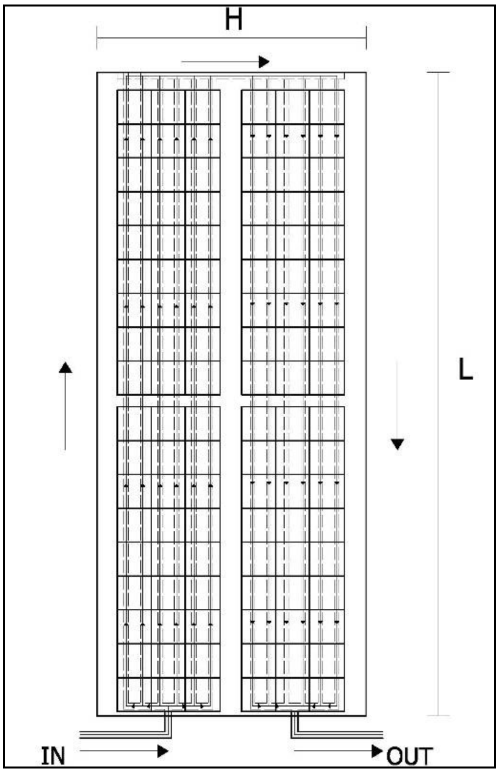

Figure 19. *Water PVT collector*

It is also interesting to observe that not all the surface of the absorber plate is covered by photovoltaic cells. In this sense it is possible to define the Packing factor (PF), that expresses the ratio between the total photovoltaic cells area and the thermal panel area. As on the panel $n_{PV} = 108$ square photovoltaic cells are positioned with side $L_{PV} = 156$ mm, the PF results:

$$PF = \frac{A_{PV}}{A_{thermal}} = \frac{n_{PV} \cdot A_{cell}}{(H - 2h_b) \cdot (L - 2h_b)} = 0.827$$

Here, the thermal area $A_{thermal}$ represents the effective surface of heat exchange, and is calculated through the difference between the total surface panel and its outer frame, whose width is $h_b = 0.06$ m.

References

[1] Thermodynamic analysis of solar hybrid (PV/T) collector. 7th National Congress Cosenza 2013

[2] Niccolò Aste- Francesco Groppi. Impianti Solari termici. Editoriale Delfino.

[3] W.A. Beckmann and A. Duffie. Solar Engineering of thermal processes, John Wiley and Sons,1980.

[4] Heat Transfer Module User's Guide 2013 Comsol

[5] J. Bradley, Fontenault, Ernesto Guitierrez-Miravete. Modeling a combined photovoltaic-thermal solar panel

CHAPTER 3

Plant layout and experimental results

3.1 Introduction

A well-known company, Sicep , has attended to the realization of the PVT prototype. As regards, it is interested in assembling and monitoring the PV modules in order to create a PVT system integrated in prefabricated modules of reinforced concrete and to characterize the prototype in terms of reliability and efficiency. In this context, the PVT module has been included in a test plant, that by means of an appropriate instrumentation, has allowed to detect experimentally some parameters such as the outflow and the absorber plate temperatures, as well as the solar irradiance needed to calculate the performance of the water PVT system.

In this section the operation logic of the test plant is described, together with the instrumentation and the main output variables needed to determine the actual efficiency of the system.

3.2 Control system

Once the PVT system has been realized, it was inserted in a test facility, operating in controlled conditions to determine the performance of the system. This test plant consists of four main components: a boiler, a storage tank of cold water , a chiller and the water PVT collectors. To explain the operation of the test facility, Figure 1 provides a simplified diagram.

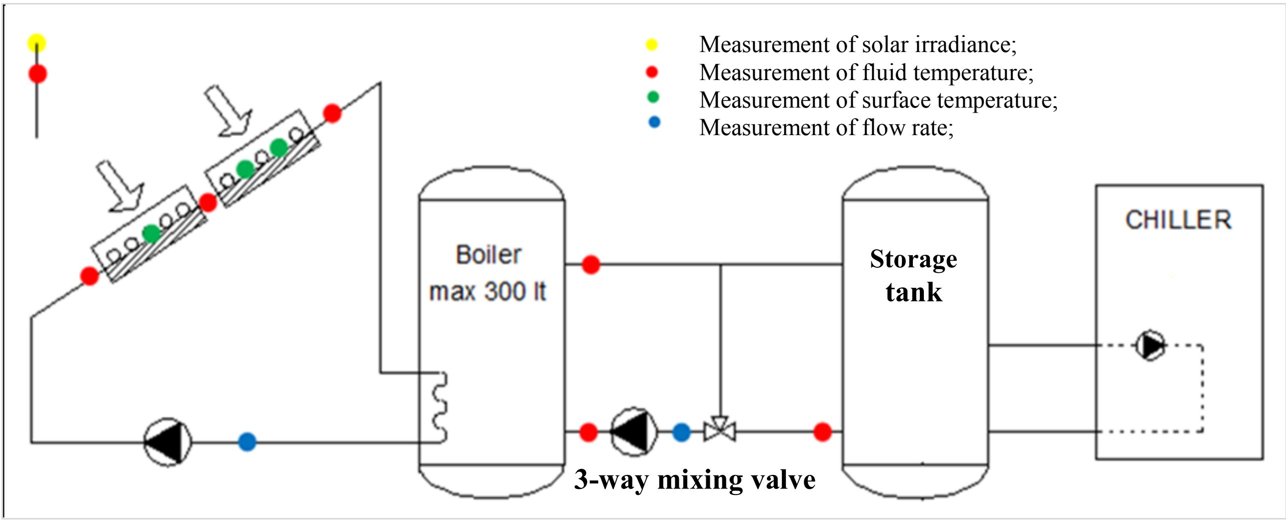

Figure 1. *Simplified test plant*

Here, one can observe a storage tank of 300 l, in which water is heated by the thermal energy recovered from the panels on one side, while on the other side it is cooled by inflow water provided by the . cold storage tank . The latter has a capacity of 200 l and keeps the cold water provided by the chiller at the temperature of 15 °C.

The electric chiller is necessary to ensure the control on the inlet water temperature to the PVT collectors; otherwise, this water would have variable temperature values, depending on the weather conditions. The control on the inlet water temperature to the PVT collector at constant values (20° C), is achieved by means of a 3-way mixing valve electronically controlled according to the boiler temperature. Figures 2 to 4 show the side view of the PVT system and the real components of the plant, respectively.

Figure 2. *Side view of the real test plant*

Figure 3. *The 3-way mixing valve.*

Figure 4. *Two main components of the plant: storage tank and boiler*

3.3 Monitoring system

The prototype has been tested during the summer 2013 at the Sicep factory, situated near Catania. In order to get controlled operating conditions, the panels have been fed with water at constant temperature, thanks to the appropriate control system previously described. The main parameters acquired during the measurement campaign were: absorber plate temperature, inlet and outlet fluid temperature, available solar radiation and outdoor air temperature.

In this context, to monitor the performance of the PVT system several temperature probes have been positioned on certain points of the plant, as shown in Fig. 5, in order to measure some significant temperature values such as:

- *T_fluid _01*, that represents the water temperature measured downstream of the storage tank;
- *T_fluid_02*, that is the inlet water temperature of the boiler, measured downstream of the mixing valve;
- *T_fluid_03*,which represents the water boiler temperature, measured in correspondence of its outflow section;
- *T_fluid_04 ,* that is the water temperature detected at the inlet of the water PVT collectors;
- *T_fluid_05* and *T_fluid_06,* that are the temperatures measured at the outlet of the two PVT prototypes, respectively;
- *T_air*, that is the outdoor air temperature;

- *T_sup_03* and *Tsup_04,* that are the surface temperatures detected on the two PVT panels;

In addition, other parameters have been detected, such us:

- the global solar irradiation *I* on the surface PVT panels, measured in W·m^{-2};
- the water flow rate $\dot{m}$ at the inlet section of the PVT collectors , measured in l·h^{-1};

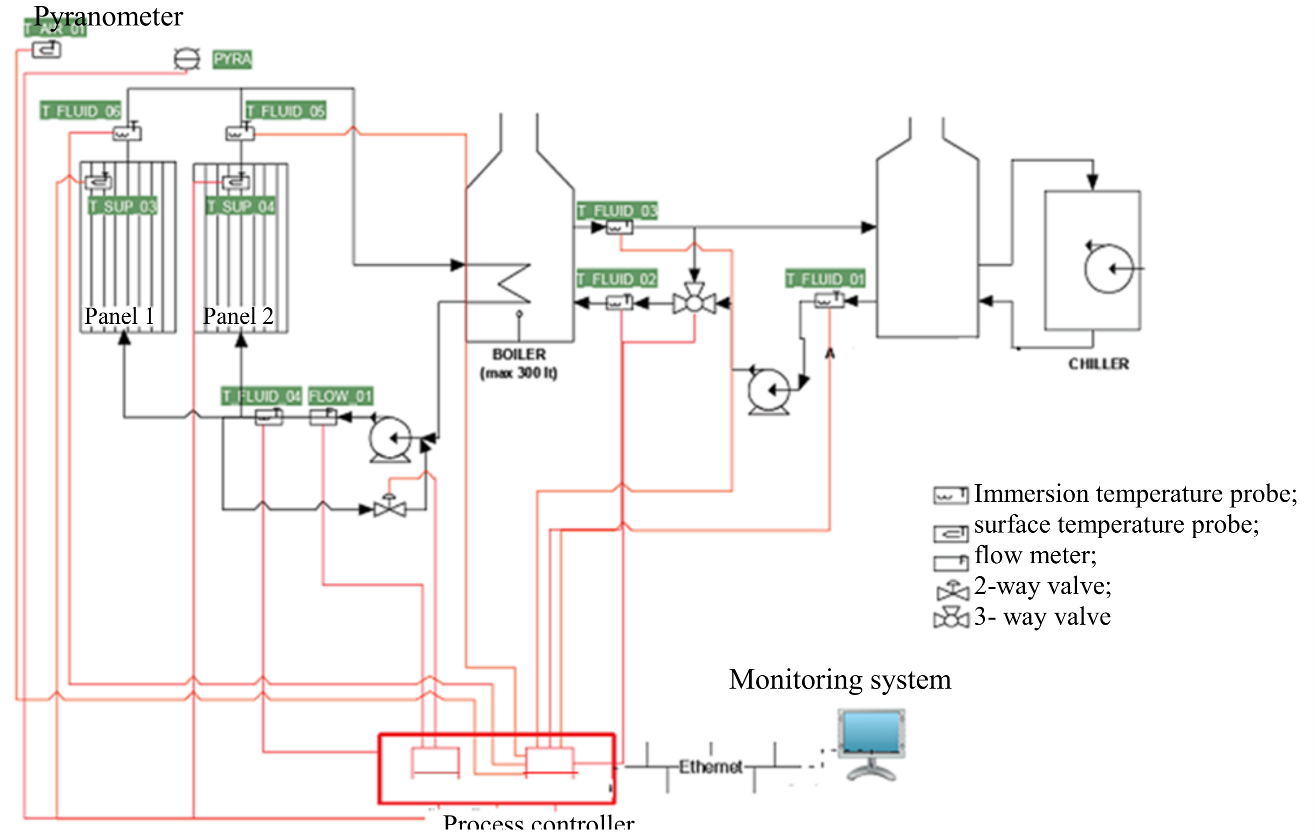

Figure 5. *Monitoring system*

The instrumental monitoring system has been defined as follows. To measure the water temperatures, the resistance thermometer probes Pt100 (immersion type) were chosen, precision class A. To detect air temperature, the probe is also a resistance thermometer Pt100 class A. The measurement of the temperatures on the PVT surfaces were carried out on two points by means of sheet resistance thermometer Pt100 class A. In Fig. 6 the three probes are shown.

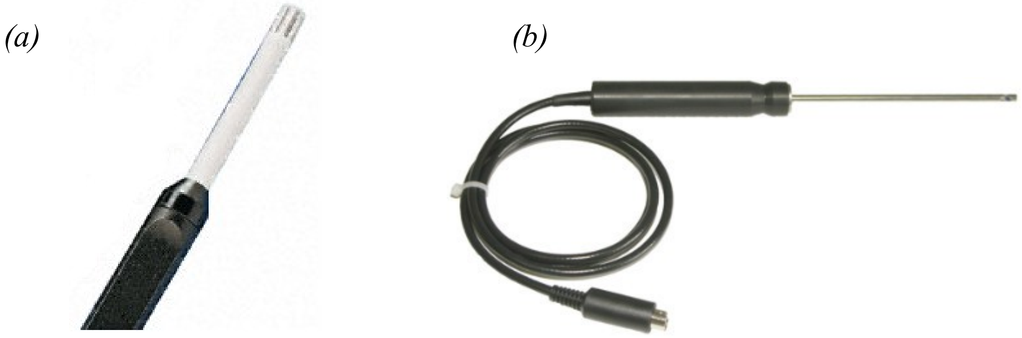

(c)

Figure 6. *Temperature probes Pt 100.(a) Immersion probe; (b) air probe; (c) surface probe*

To measure the global solar irradiance, a pyranometer was selected. It has complete protection with cartridge of silicagel crystals, as shown in Fig. 7; as an output, it provides a current signal. The pyranometer was installed on a suitable support, so that its base is inclined 20° from the horizontal, which is the same inclination of the PVT prototypes.

Figure 7. *Pyranometer*

As one can see from the test plant at the inflow manifold, a flow meter was placed to detected the water flow rate.

Figure 8. *Flow meter*

As regards the chiller, a model of about 6 kW is installed, for cooling only, with circulation pump and expansion tank integrated.

The acquisition of these parameters was possible by means of the National Instruments controller. The acquired data, with time step of 5 minutes, allowed to evaluate the actual performance of the PVT panels.

3.4 Experimental outputs

The measurement campaign, carried out from April to June 2013, has allowed to characterize the two PVT prototypes in terms of electric and thermal efficiencies.. Figures 9, 10, and 11 show the experimental output recorded during the first week in June.

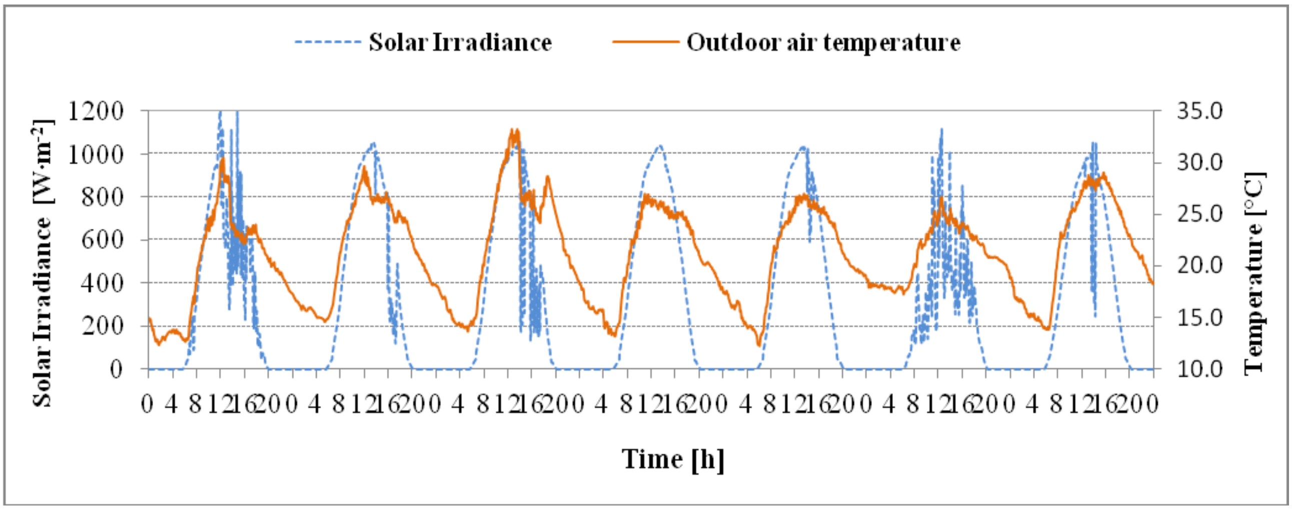

Figure 9. *Solar Irradiance and outdoor air temperature recorded during the first week in June*

During this investigation period, the outdoor temperature profile presents rather regular daily trends. In particular, on June the 3rd a maximum temperature of 33.2°C is recorded. On the other hand, the temporal distribution of the solar irradiance shows different daily trends, which depend on shadowing phenomena. The peak value is usually around 1000 [W·m^{-2}].

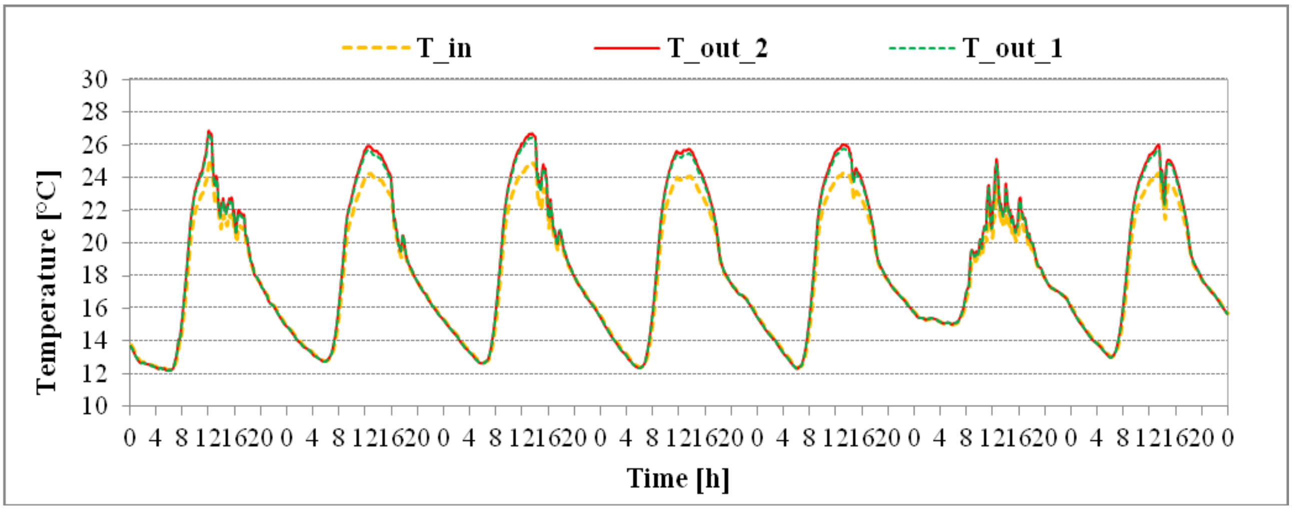

Figure 10. *Inflow and outflow temperatures recorded during the first week in June*

As is clear from Fig. 10, there is a very good overlapping of the two outflow temperature curves. In more detail, they reach a maximum value around 27°C at 12:01 on June 1st. In the same figure, the inflow temperature is plotted in order to consider the thermal drop between the inflow and outflow temperatures; this difference is about 2°C during the sunniest hours of the day.

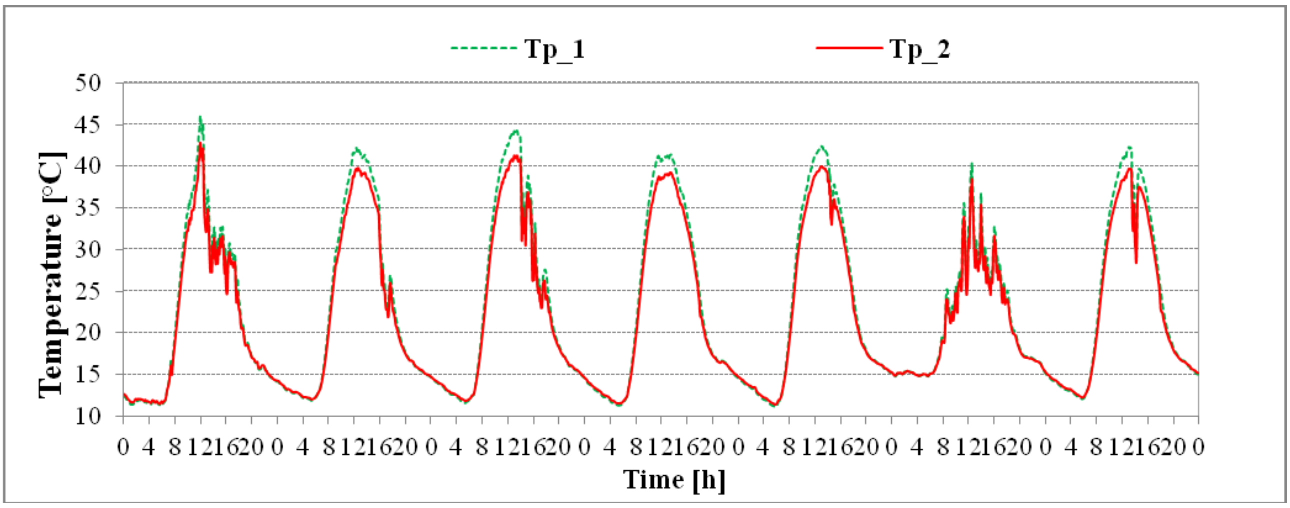

Figure 11. *Surface temperatures of the two absorber plates recorded during the first week in June.*

On the other hand, Fig. 11 shows the temperature trends detected on the two absorber plate surfaces. Here, one can observe a significant mismatch between *Tp_1* and *Tp_2*. This discrepancy is evident between 11:00 and 13:00 and the average maximum value of surface temperature is 44.5°C. In addition, the temperature profile *Tp_1* is higher than the temperature trend *Tp_2* during the whole investigation period.

In order to ensure a good efficiency of heat transfer, each PVT panel has been fed by 270 [$l \cdot h^{-1} m^{-2}$] of water flow rate. This corresponds to a velocity w = 0.621 [$m \cdot s^{-1}$] within the channels. Actually, the feeding system cannot ensure constant flow rates. Fig. 12 shows the flow rate fluctuations detected by means of the flow meter.

During the period of investigation the flow rate oscillates between 260 [$l \cdot h^{-1}m^{-2}$] and 280 [$l \cdot h^{-1}m^{-2}$], and the value 270 has a very good occurrence percentage as provided by Fig.13.

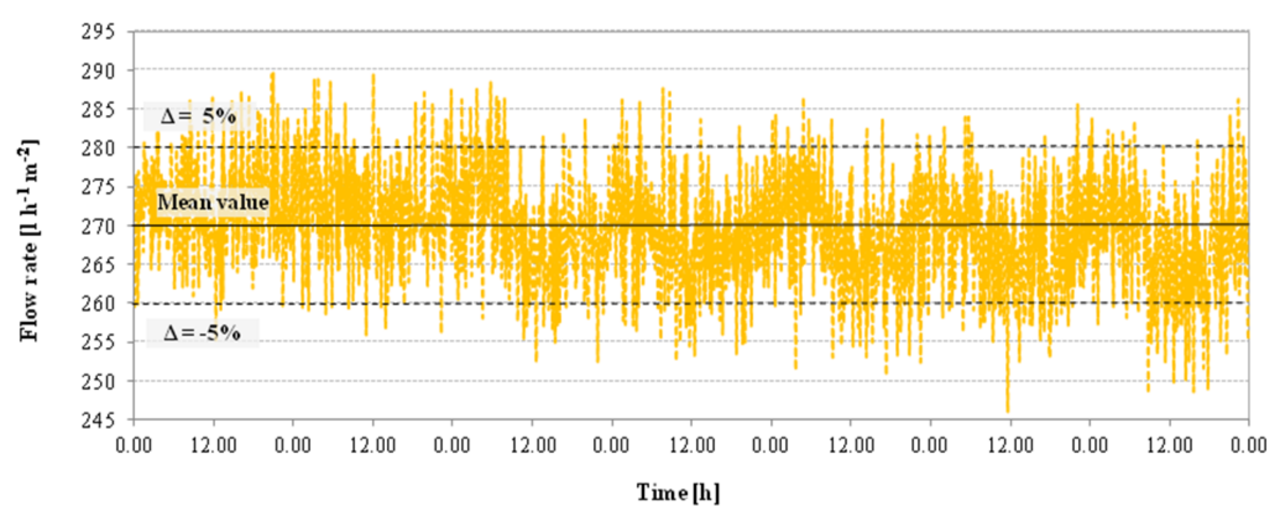

Figure 12. *Flow rate trend recorded during the first week in June*

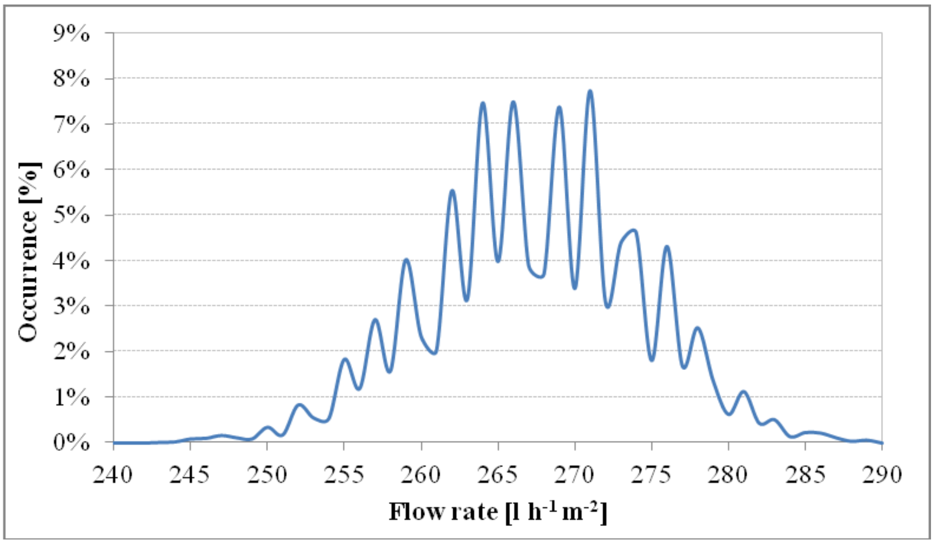

Figure 13. *Flow rate trend in June*

Once we found the temporal distribution of the flow rate, the thermal output $\dot{Q}_{th}$ and electrical output P_{elec} of the two PVT collectors were calculated from the measured data as follows:

$$\dot{Q}_{th} = \dot{m}_W \cdot c_p \left(T_{out} - T_{in}\right) \qquad (1)$$

where c_p is the specific heat, $\dot{m}_w$ the mass flow rate, and T_{out} and T_{in} are the outlet and inlet temperatures of the fluid, respectively.

$$P_{el} = \eta_{\_\ V} \cdot I \cdot A_{PV} \tag{2}$$

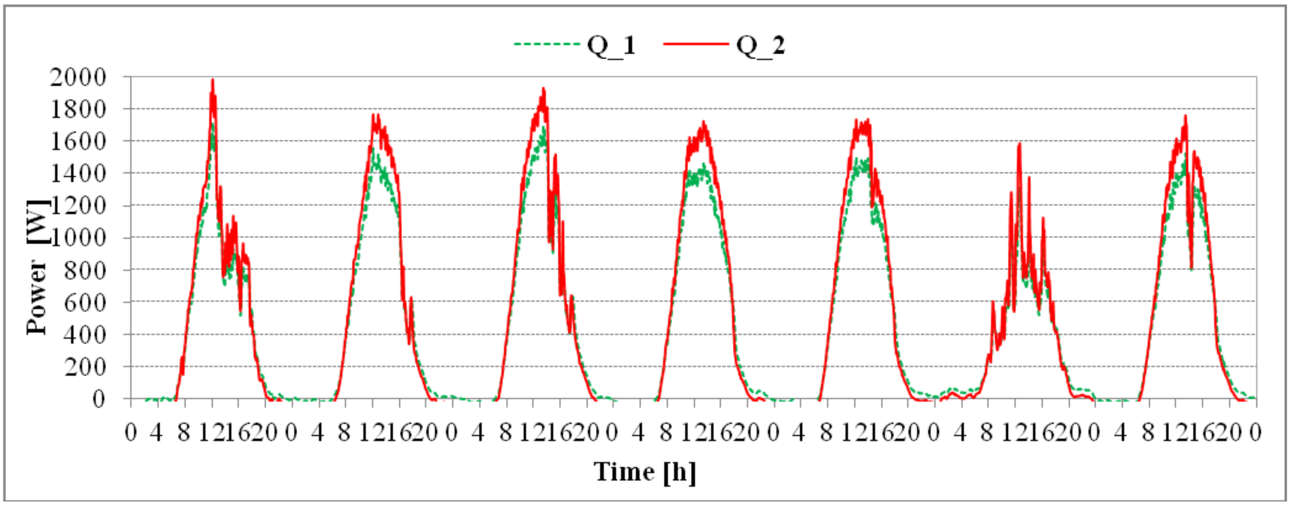

Figure 14. *Thermal power trends of the two PVT prototypes recorded during the first week in June*

In Fig. 14, the thermal power trends *Q_1* and *Q_2* are shown. Whereas the temperature profile outflow *T_out_2* is slightly higher than *T_out_01*, the thermal yield supplied from the second prototype is greater than that provided by the first one, too.

The same considerations spring from the evaluation of the experimental outputs recorded in all other weeks. Furthermore, in table 1 the weekly values of the absorber plate temperature peaks, the irradiation, and the thermal energy are reported.

	Irradiation	**Thermal Energy**	$\mathbf{T_{p,max}}$
	[MJ]	[MJ]	[°C]
first week	586.4	279.6	44.5
second week	638.1	320.4	43.5
third week	646.6	364.5	45.0
fourth week	529.7	280.7	43.7
total	2400.8	**1245.2**	

Table 1. *Experimental results*

So, one can conclude that monthly thermal energy and efficiency provided by each PVT panel are 1245 [MJ] and 51.9%, respectively.

3.5 Thermal and electric efficiencies

Due attention is paid to an important drawback related to the PV cells: since they convert a fraction of the incident solar radiation directly into electricity, they also determine a reduction in the thermal absorption capacity of the absorber plate. This reduction is obviously proportional to the electrical efficiency η_{PV} of the PV cells. The latter depends linearly on the temperature Tp of the cells, according to the well-known relation reported as follows:

$$\eta_{PV} = \eta_{STC} \cdot \left[1 - \mu \left(T_p - 25\right)\right] \tag{3}$$

Here, η_{STC} is the electrical efficiency measured in standard conditions, and μ is the temperature coefficient. So Equation (2) becomes:

$$P_{el} = I \cdot A_{PV} \cdot \eta_{STC} \cdot \left[1 - \mu \left(T_p - T_a\right)\right] \tag{4}$$

Finally, the thermal efficiency η_{th} and electrical efficiency η_{elec} of the collector are defined as follows:

$$\eta_{th} = \frac{\dot{Q}_{th}}{I \cdot A_{th}} \tag{5}$$

$$\eta_{elec} = \frac{\dot{Q}_{elec}}{I \cdot A_{PV}} = \eta_{PV} \tag{6}$$

In which A_{th} = 3.18 m^2 and A_{PV} = 2.63 m^2 represent the surface area of the only absorber plate, obtained by excluding the side insulating layer, and the total surface of the PV cells to the overall absorber surface, respectively.

In addition, the thermal efficiency can be expressed as a function of the ratio $T^* = (T_p - T_{air})/I$. Figure 9 reports the thermal efficiencies of the two PVT prototypes. The overall energy efficiency $\eta_{overall}$ can be stated as:

$$\eta_{overall} = \frac{\dot{Q}_{th} + P_{elec}}{I \cdot A_{th}} = \eta_{th} + PF \cdot \eta_{elec} \tag{7}$$

Using the mass flow rate and outflow temperature values it was found the weekly thermal efficiency as reported in Table 2 :

	Thermal efficiency
	[%]
first week	47.7%
second week	50.2%
third week	56.4%
fourth week	53.0%
total	**51.9%**

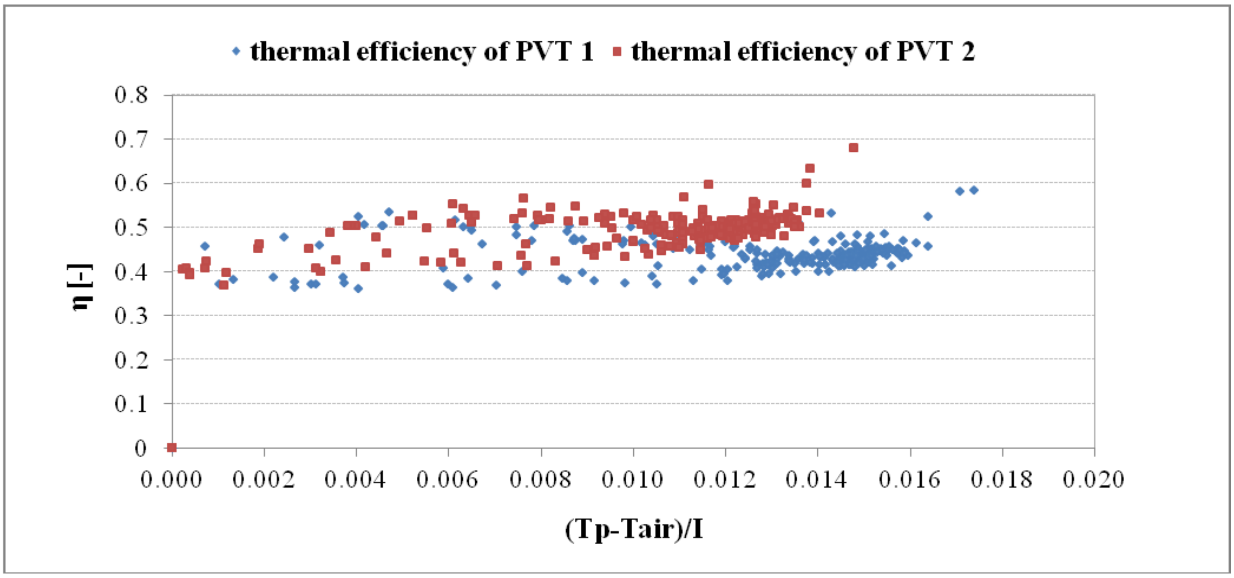

Figure 15. *Thermal effiencies of two PVT prototypes*

Here, the trend of the thermal efficiency reported in Fig. 15 suggests that the calculated thermal performance of the two PVT prototypes are not as good as for a traditional flat plate glazed solar collectors. Indeed, these usually shows an average peak efficiency η_{t0} = 0.7-0.75, while the slope of the efficiency curve is around 4-5 W/(m^2K). Normally, as the parameter T^* increases, the thermal efficiency decreases.

On the contrary, in this case their trends are almost constant. These results are probably due to a series of constructive faults, that will be investigated in the following sections.

CHAPTER 4

Mathematical modeling of the water PVT prototype

4.1 Introduction

Once the water PVT prototype has been designed and realized, an in-depth heat transfer analysis was carried out to evaluate analytically the performance of the entire system. In this context, a numerical code has been implemented on Mathcad 15.0, whose equations, describing the physics of the problem, are used to determine the characteristic operational parameters of the water PVT collector, such as the outflow water temperature, the absorber plate temperature, the thermal and electrical energy yield and consequently their respective efficiencies. The simulations were carried out on an annual basis, analyzing for each month, the system performance related to a typical day.

4.2 Data Input

In order to simulate on Mathcad the thermo-physical behavior of the PVT system, the first step is to enter the input data necessary for the calculations, such as the outdoor air temperature, the solar irradiation on the PVT surface and the fluid temperature at the inlet of the heat exchanger. To determine the performance of the PVT system on an annual basis, the weather data detected from the site of Catania have been used as input parameters, while to validate the mathematical model were used only weather data recorded in two sample days in June at Sicep factory. The temporal distributions of these parameters are very accurate because they were collected by the acquisition system discussed in Section 3 with a time step of 5 minutes. Figures 1 and 2 show the temporal profiles of the input parameters for a sample day (4th June 2013).

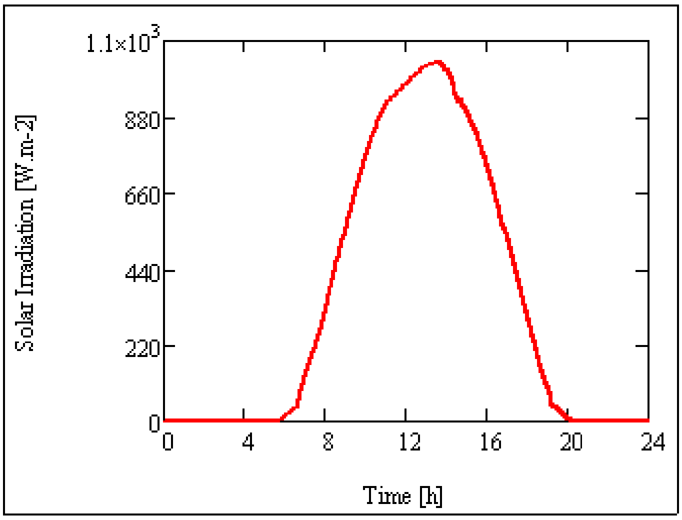

Figure 1: *Solar Irradiance on PVT surface (4th of June 2013)*

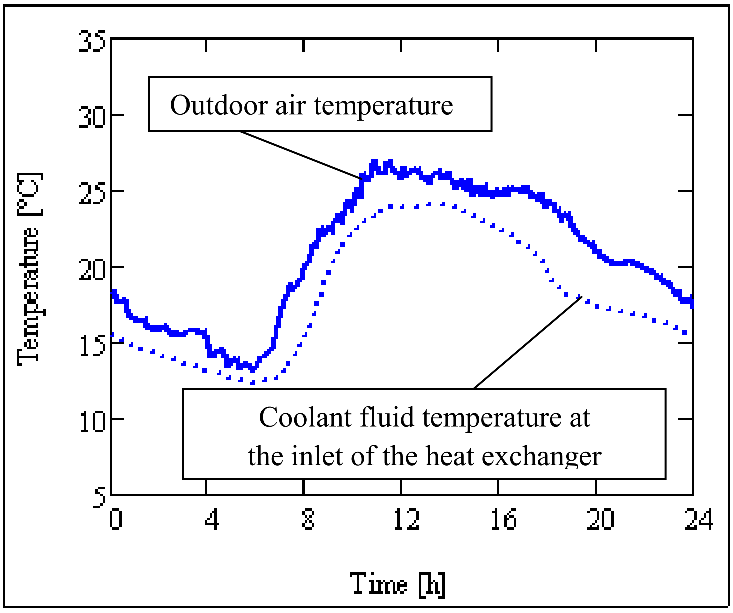

Figure 2: *Outdoor air temperature and inlet fluid temperature (4th of June 2013).*

The mathematical model developed on Mathcad is also able to account for the variation of the optical properties of glass and absorber with the incidence angle θ of the sunbeams. In order to exploit this feature, the equations for the calculation of the incidence angle as a function of time, collector tilt angle ($\beta = 20°$) and latitude ($\Phi = 38°$) were also implemented. Other important input data, concerning the geometrical characteristics of the absorbing plate and the thermo-physical properties of the coolant fluid, will be described in detail in the next paragraphs.

4.3 Radiation transmission through glass cover

To determine the amount of solar radiation impinging and kept by the absorber plate it is important to know its absorption coefficient α and the transmission mode through the transparent media. To this purpose it is necessary to refer to optical concepts.

In more details, when the solar radiation crosses two different media such as air (refractive index $n_a = 1.00029$) and glass (refractive index $n_{glass} = 1.526$), at the interface between the two media the beam splits into two components: one transmitted with intensity I_t and the other one reflected with intensity I_r (see Fig. 3):

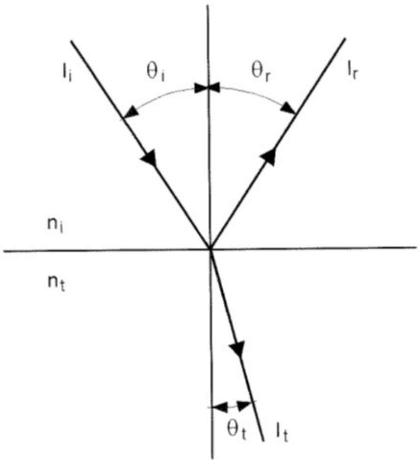

Figure 3. *Reflection and refraction through two media*

The angle formed by the reflected beam with the normal to the interface surface is equal to that formed by the incident beam, that is to say $\vartheta = \vartheta$. Instead, the fraction of solar radiation transmitted through the medium has a different direction from the original one, as it undergoes refraction phenomena governed by Snell's law [1]:

$$\frac{n_i}{n_t} = \frac{sen\,\vartheta}{sen\,\vartheta} \tag{1}$$

Here, ϑ represents the angle formed by the new direction with the normal to the interface surface. Therefore, if one knows the refractive indices of the two media and the angle of incidence of the solar radiation, using the equation (1) it is possible to determine the refraction angle ϑ.

The ratio between the intensity of reflected and incident solar radiation on a surface is the reflection coefficient ρ. This coefficient, in case of unpolarized solar radiation and smooth surface, is calculated as the average between the parallel and perpendicular components of the solar radiation to the incidence plane (i.e. the plane that contains incident, reflected and transmitted beam). So the reflection coefficient is expressed as follows:

$$\rho = \frac{I_r}{I_i} = \frac{r_{II} + r_{\perp}}{2} \tag{2}$$

In which r_{II} and $r_{\perp}$ represent the parallel and perpendicular solar radiation components, respectively calculated using Equations (3) and (4):

$$r_{II} = \frac{\tan^2(\vartheta - \vartheta)}{\tan^2(\vartheta + \vartheta)} \tag{3}$$

$$r_{\perp} = \frac{sen^2(\vartheta - \vartheta)}{sen^2(\vartheta + \vartheta)} \tag{4}$$

Now, in order to calculate the angle of incidence of the beam radiation, one can consider the geometric relationship that expresses it as a function of the position of the sun in the sky, see Eq. (5):

$$\vartheta_i = ar\cos[\cos(\phi - \beta) \cdot \cos\delta \cdot \cos\omega + sen(\phi - \beta) \cdot sen\delta] \tag{5}$$

In Eq. (5), the angles *Φ*, *β, δ* and *ω* represent the latitude, the tilt angle, the declination and hour angle, respectively, as represented in Fig. 4. In more detail, *δ* and *ω* are time dependent values: in fact, the declination angle indicates the angular position of the sun at solar noon with respect to the plane of the equator, varying in the range from -23.45° to 23.45°, while the hour angle regards the angular displacement of the sun from east to west of the local meridian due to the rotation of the earth on its axis at 15° per hour, morning negative, afternoon positive. The declination *δ,* can be found from the equation of Cooper:

$$\delta = 23.45 sen\left(360\frac{284 + n}{365}\right) \tag{6}$$

Where *n* is the day of the year.

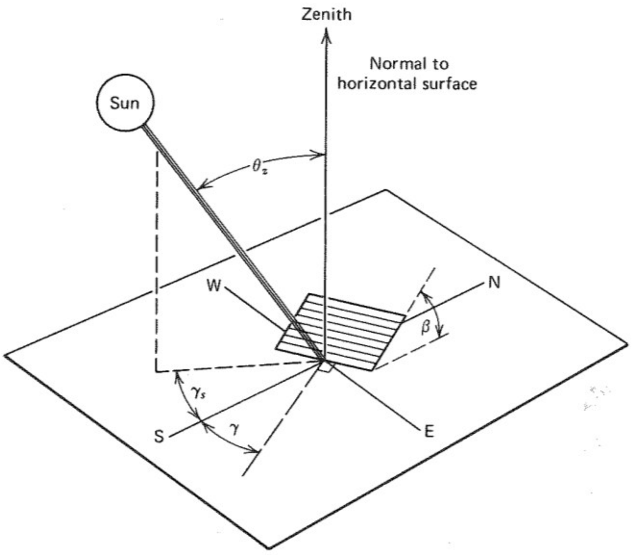

Figure 4. *Zenit angle, slope, surface azimuth angle and solar azimuth angle for a tilted surface*

Considering that the incident solar radiation on a surface can be considered as the sum of three components: direct, diffused and reflected radiation, the Eq. (5) expresses only the angle of incidence relative to the direct component. As concerns the other components, they do not come from defined directions, thus an average angle of incidence is assumed, corresponding to 60°. Figure 5 shows the temporal distribution of the incidence angle for direct radiation related on a simple day in January, April, July and October.

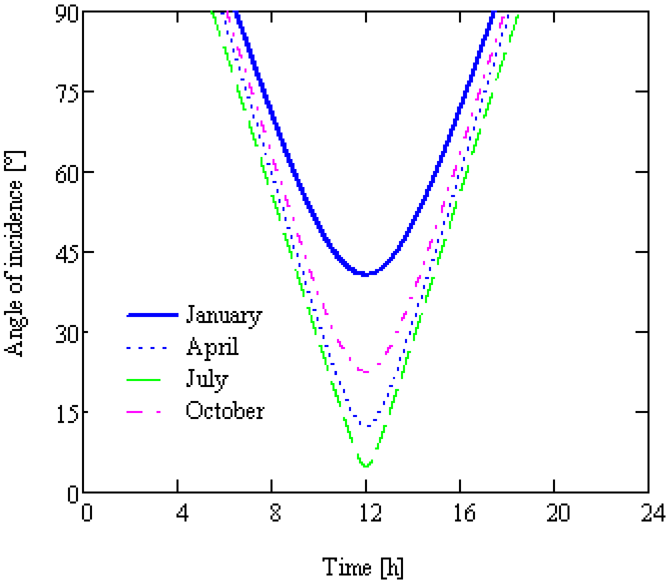

Figure 5. *Temporal distribution of the incidence angle (Catania, β =20°).*

4.4 Optical properties

In the case of a PVT system formed by a single glass, solar radiation first crosses the interface between the external air and the glass, and then the air gap contained between the glass and the absorber plate. In this case, as one can see from Fig. 6, multiple refractions and reflections occur inside the glass.

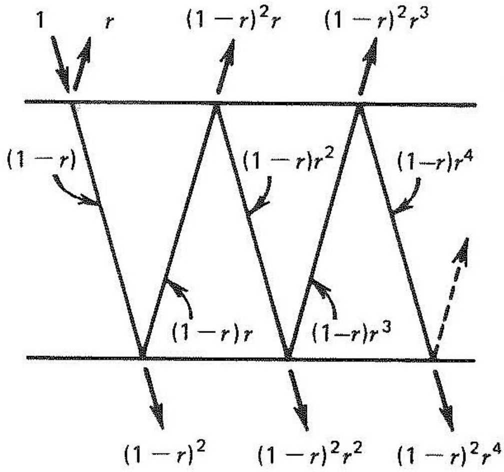

Figure 6. *Transmission through a non-absorbing cover.*

Therefore, it is important to consider the attenuation phenomenon of solar radiation when it passes through the transparent medium. To this aim, the transmission coefficient of the glass can be calculated through Eq. (7):

$$\tau_a = \frac{I_\tau}{I_0} = e^{-\frac{K\cdot d}{\cos\vartheta}} \tag{7}$$

where *K* is a constant, called *extinction coefficient*, that is assumed equal to 8 m^{-1} for glass with low iron content, while *d* is the glass thickness [2].

Starting from the transmittance of the glass τ_a , it is possible to determine the overall transmitted, reflected and absorbed componnets:

$$\tau = \tau_a \cdot \frac{1}{2}\left(\frac{1-r_{II}}{1+r_{II}} + \frac{1-r_\perp}{1+r_\perp}\right)$$ *Transmitted component* (8)

$$\rho = 1 - \tau - \alpha$$ *Reflected component* (9)

$$\alpha = 1 - \tau_a$$ *Absorbed component* (10)

Figure 7 shows the temporal distribution of the glass transmission coefficient in January, April, July and October.

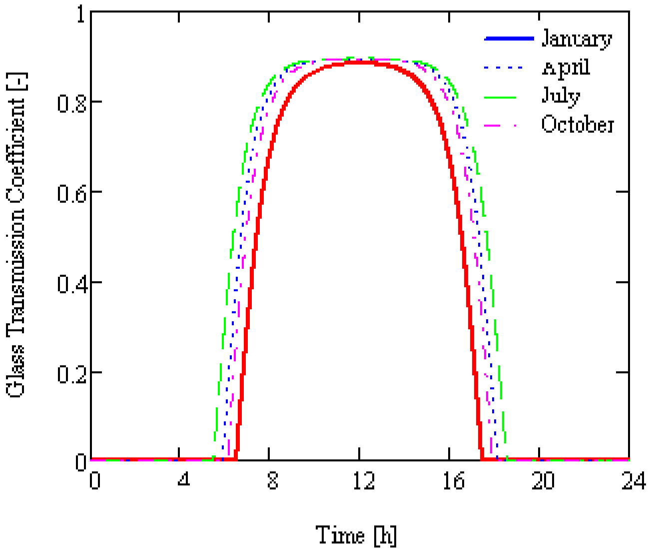

Figure 7. *Glass transmission coefficient τ on a sample day in January, April, July and October.*

4.5 Transmittance-absorptance product

Now, to assess the actual energy captured by the absorber plate, it is necessary to evaluate the transmittance-absorptance product ($\tau\alpha$). Indeed, a certain fraction of the radiation passing through the cover system and striking the plate is reflected back to the cover system. However, all this radiation is not lost, since in turn it is partially reflected back to the plate. This phenomenon is illustrated in Fig. 8, where τ is the transmittance of the cover system at the desired angle and α is the angular absorptance of the absorber plate.

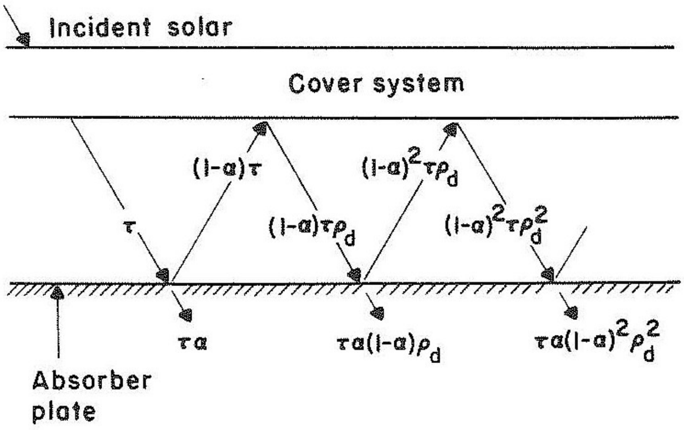

Figure 8. *Adsorption of solar radiation by absorber plate.*

Starting from the incident radiation, the fraction $\tau\alpha$ is absorbed by the absorber plate, and the fraction $(1-\alpha)\cdot\tau$ is reflected back to the cover system. The reflection from the absorber plate is assumed to be diffuse (and unpolarized), so the fraction $(1-\alpha)\cdot\tau\cdot\rho_d$ is reflected back to the absorber plate. The quantity ρ_d refers to the reflectance of the cover system for diffuse radiation incident from the bottom, and can be estimated from equation (11) at an angle of 60°:

$$\rho \cong \;_{a}(- \;_{r}) = \;_{a} - \tag{11}$$

The multiple reflection of diffuse radiation continues so that the energy ultimately absorbed is :

$$\tau\alpha = \alpha\sum_{n=0}^{\infty} 1- \chi \; ^{n} = \frac{\tau\alpha}{1-(- \chi} \tag{12}$$

This parameter has been calculated by means of Mathcad at different values of τ ,which depends on the daily variation of the solar irradiance. Figure 9 shows its temporal distribution on a sample day in January, April, July and October

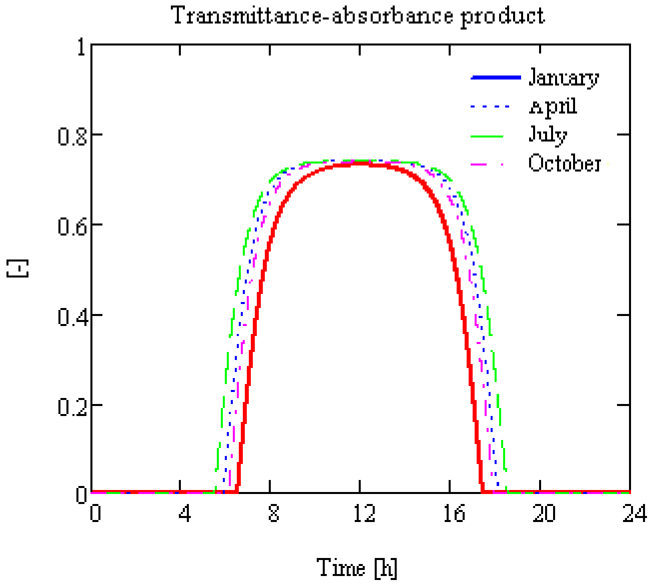

Figure 9. *Temporal distribution of transmittance-absorbance product*

In addition, the glass fouling is another significant parameter that contributes to reduce the solar radiation absorbed by the plate. The effect of the dust is difficult to generalize. The data of Dietz [2] shows that at the angle of interest (0° to 50°) the influence of dust can be as high as 5 percent. From long-term experiments on collectors in the Boston area, Hottel and Woertz [2] found that collector performance decreased by approximately 1% due to dirty glass. In a rainless 30-day experiment in India, Garg [2] found out that dust reduced the transmittance by an average 8% for glass tilted at 45°. For design purposes without extensive tests, it is suggested that radiation absorbed by the plate be reduced by a factor of f_s, where f_s = 0.98 for dust, but this parameter is heavily dependent on external conditions. Hence, Eq. (12) becomes:

$$(\tau\alpha)_e = f_s \cdot \frac{\tau\alpha}{1-(1-\alpha)\rho_d} \qquad (13)$$

4.6 Thermo-physical properties and input parameters for the coolant fluid

Water is the coolant fluid that flows within the channels of the absorber plate. In the simulations, its thermo-physical properties, such as the specific heat C_p and the density ρ, are constant values equal to 4200 $J\cdot kg^{-1}\cdot K^{-1}$ and 990 $kg\cdot m^{-3}$, respectively. On the other hand, the thermal conductivity λ and the cinematic viscosity υ are functions that depend on the inlet water temperature, as provided by the Eq. (14) and Eq. (15), respectively:

$$\lambda(T_{in}) = -\,.9\cdot 10^{-}\cdot T_{in}^2 + 0.001745\cdot T_{in} + 0.5704 \qquad (14)$$

$$\upsilon(T_{in}) = .88\cdot 10^{-\,0}\cdot T_{in}^2 - 2.96\cdot 10^{-}\cdot T_{in} + .55\cdot 10^{-} \qquad (15)$$

These equations have been obtained by interpolating the viscosity and conductivity data collected in the literature at different temperature values.

The convective heat exchange coefficient ***h*** relative to the cooling fluid is another significant parameter, evaluated by means of equation (15):

$$h = \frac{Nu\cdot\lambda}{D_{eq}} \qquad (16)$$

In which :

- D_{eq} is the equivalent diameter of the channel. Its value is calculated by means of Eq. (17) :

  $$D_{eq} = \frac{1.3\cdot l^{2\cdot 0.625}}{(2\cdot l)^{0.25}} = 0.0087\,m \qquad \text{with } l = \text{channel inner side} \qquad (17)$$

- *Nu* is the Nusselt number, that is a function of the flow regime, governed by Reynolds number. So for $Re \geq 2500$, Nusselt number is equal to:

  $$Nu = 0.023\cdot \mathrm{Re}^{0.8}\cdot \mathrm{Pr}^{0.4} \qquad (18)$$

Here, Pr represents the Prandtl number, that varies with the inlet temperature of the absorber plate as provided by Eq. (19):

$$\Pr(t) = 0.00161 \cdot T_{in}^{2}(t) - 0.234 \cdot T_{in}(t) + 1.105 \qquad (19)$$

This relation was found in the same manner as for λ and υ.

In addition, the PVT prototype receives a total water flow rate of about 0.236 $kg \cdot s^{-1}$. Since water is distributed evenly in the six channels, each of them receives a rate equal to 0.0393 $kg \cdot s^{-1}$, with a corresponding velocity around 0.621 $m \cdot s^{-1}$.

4.7 Governing equations of heat exchange

The mathematical modeling of the energy performance of the PVT system, aimed to estimate its electricity and heat production, requires the introduction of some simplifying assumptions. Firstly, it is assumed that the absorbing plate temperature is uniform, that is to say the whole PVT collector is characterized by a single surface temperature value, attributed to the plate absorber and photovoltaic cells positioned on it. In addition, the collector is composed of six identical hydraulic circuits set in parallel, thus in order to calculate the temperatures characteristic of the water PVT system it is possible to focus only on one of them.

In agreement with this assumption, the control volume analyzed is the same used in Comsol simulations (see Section 2) but with a duct length equal to $2 \cdot L$ and including the glass layer. Hence, in the following the equation set regarding heat transfer from the frontal plate to the coolant fluid is introduced. Firstly, Eq. (20) represents the thermal energy balance in a non-stationary system relative to the control volume shown in Fig. 10.

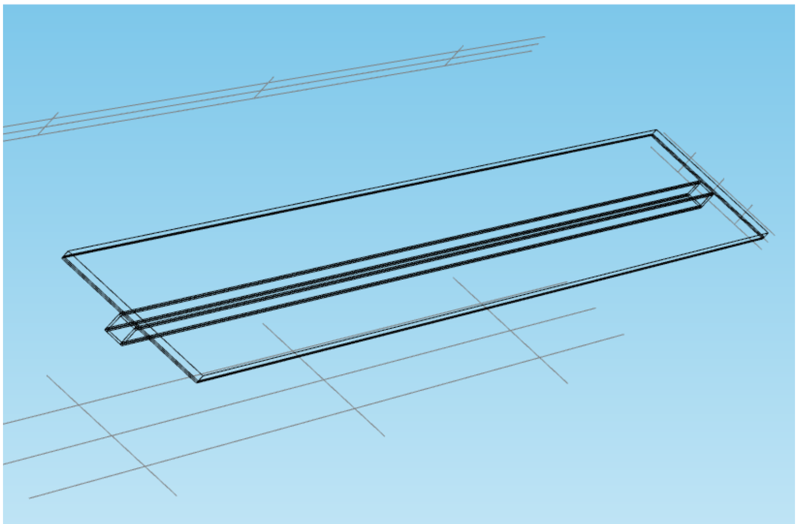

Figure 10. *Control volume analyzed*

$$\dot{Q}_{sol} - \dot{Q}_L - \dot{Q}_w = M_{abs} \cdot c_{p,abs} \cdot \frac{dT_p}{dt} \tag{20}$$

In which:

$$\dot{Q}_{sol} = 2L \cdot \left[(W - D) \cdot F + D\right] \cdot I_{sol} \cdot \left[\tau\alpha\,(1 - \eta_{PV})\right] \tag{21}$$

$$\dot{Q}_L = U_L\,(2L \cdot W) \cdot (T_p - T_a) \tag{22}$$

$$\dot{Q}_w = \dot{m}_w \cdot c_{p,w} \cdot (T_{out} - T_{in}) \tag{23}$$

Equation (21) expresses the energy collected along the flow direction, through the fin surface and the fraction of area above the channel. In addition it takes into account the reduction of the energy absorbed by the absorber plate, due to the presence of the PV cells, which convert a fraction of solar radiation into electrical energy. This reduction is proportional to the electric efficiency, which varies linearly with the PV temperature, as provided by Eq. (24):

$$\eta_{PV} = \eta_{STC} \cdot \left[1 - \beta\,(T_p - T_a)\right] \tag{24}$$

Here, η_{STC} is the electrical efficiency evaluated in standard conditions and β is the temperature coefficient of the PV cells. Considering that the PV cells are made of polycrystalline silicon, η_{STC} and β are equal to 0.157 and 0.0047, respectively.

Equation 21 also includes the so-called fin efficiency F (which has been treated in chapter 2) that takes into account the heat distribution mode along the fin of the absorber plate. Figure 11 shows the surfaces involved to this thermal exchange for a generic absorber.

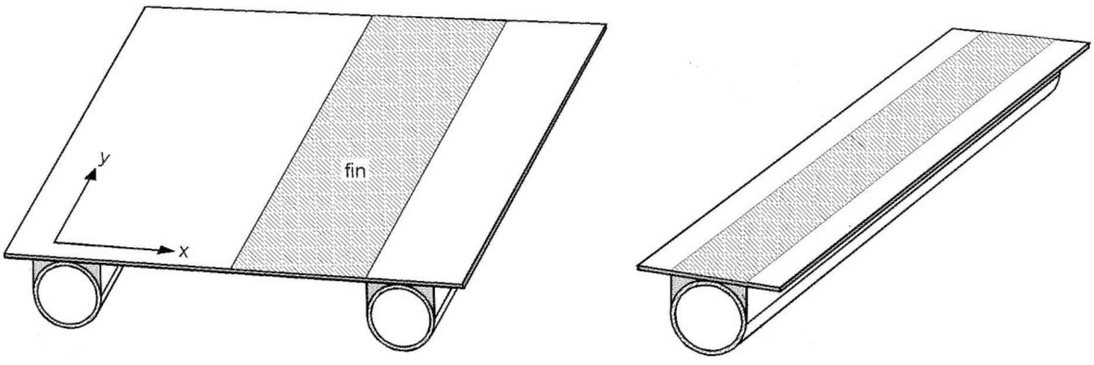

Figure 11. *Surfaces involved in the heat exchange.*

Furthermore, Eq. (22) describes the thermal energy transferred from the absorber plate to the external environment. In more detail, U_L represents the overall loss coefficient, and its value is given by the sum of the top, bottom and edge loss coefficients. However, the back and edge losses rarely exceed 10% of the total for a well insulated PVT system in ordinary operating conditions, i.e. when the absorber plate temperature is between 40°C and 60 °C. The top loss coefficient U_f is the most important parameter, its value varies with the absorber plate and external air temperature as provided by Equations (3)-(5) in Chapter 2.

Figure 12 shows the temporal distribution of the overall loss coefficient when the temperature of the absorber plate is 35°C.

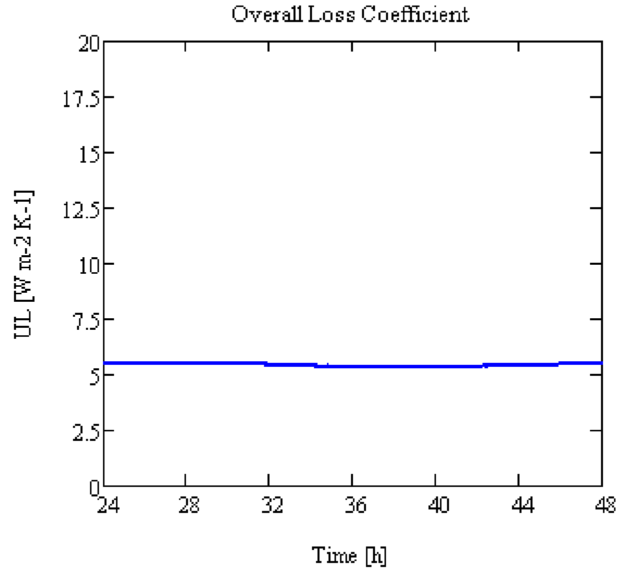

Figure 12. *Temporal distribution of the overall loss coefficient* U_L

Finally, Eq. (23) expresses the thermal energy transferred to the coolant fluid. It is noted that the terms of Eq. (20) can be specified by means of Eq. (21) to (23), that contain two variables: the absorber plate temperature and the outlet temperature of the coolant fluid. Thus, to solve the thermal balance equation, it is necessary to write another relation that contains T_p and T_{out}. In this context, the fin model can be considered as a heat exchanger in which the water, flowing in the square channel, changes its temperature while absorbing heat from an object at uniform temperature. Thus, one can write Eq. (25):

$$\dot{m}_w \cdot c_{p,w} \cdot (T_{out} - T_{in}) = -UA_c \cdot \frac{(T_{out} - T_{in})}{\ln\left(\frac{T_{out} - T_p}{T_{in} - T_p}\right)} \tag{25}$$

In which UA_c is the inverse of the overall thermal resistance as provided by Eq. (26):

$$UA_c = \left[\frac{1}{\alpha\ \ 4a\cdot 2L}+\frac{\delta}{\lambda\ \cdot a\cdot 2L}\right] \qquad (26)$$

This equation does not take into account any contact resistance between the absorber plate and the channels, that is normally considered negligible.

4.8 Performance of the PVT system.

This calculation model was finally applied to the PVT prototype to determine its thermal and electric performance. The simulation was carried out on a hourly basis, characterizing each month by means of a typical day, and to this purpose the climatic data relating to the city of Catania have been used. Table 1 resumes the main calculation parameters:

$a = 0.01$	[m]	$\Lambda p = \lambda c = 23$	$[\mathrm{Wm^{-1}K^{-1}}]$
$W = 0.079$	[m]	$\varepsilon_{abs} = 0.9$	[-]
$L = 2.966$	[m]	$\varepsilon_{glass} = 0.88$	[-]
$c_{p,abs} = 502$	$[\mathrm{Jkg^{-1}K^{-1}}]$	$\beta = 0.0047$	$[°\mathrm{C^{-1}}]$
$\delta_{abs} = 0.6\cdot 10\text{-}3$	[m]	$\eta_{stc} = 0.157$	[-]
$\delta_c = 1\cdot 10\text{-}3$	[m]	$c_{p,w} = 4200$	$[\mathrm{Jkg^{-1}K^{-1}}]$
Mabs = 3.9	[kg]	$n_{air} = 1.00029$	[-]
$w = 2$	$[\mathrm{ms^{-1}}]$	$n_{glass} = 1.526$	[-]

Table 1. *Main parameters used in Mathcad simulations*

The set of equations presented in the previous section allows to calculate at each time step:

- The absorber plate temperature, T_p
- The fluid temperature at the outlet of the heat exchanger, T_{out}
- The thermal power delivered to the users, $\dot{Q}_w$

Therefore, the electric and thermal power provided by the PVT prototype are calculated by means of Eq. (27) and Eq. (28), respectively:

$$P_{el} = \eta_{\_V}\cdot I_{sol}\cdot A_{PV} \qquad (27)$$

$$\dot{Q}_t = \dot{Q}_w \cdot \frac{A_{tot}}{(L\cdot W)} \qquad (28)$$

The model is completed by Eq. (29), which links fluid and absorbers temperatures by accounting for the heat transfer between them.

$$T_{out} = T_p + \left(T_{in} - T_p\right) \cdot e^{-\frac{UA}{\dot{m}_w \cdot c_{p,w}}} \tag{29}$$

In addition, the thermal and electrical efficiencies are the main indicators of performance quality of a water PVT system and are defined as follows:

$$\eta_{th} = \frac{\dot{Q}_t}{I \cdot A_{ther}} \tag{30}$$

$$\eta_{el} = \frac{P_{el}}{I \cdot A_{PV}} \tag{31}$$

In which the thermal and PV areas, A_{therm} and A_{PV} have already been defined in Section 2.

Finally, it is interesting to evaluate the average daily performance of the PVT system, so integrating Eq. (30) and Eq. (31) over a daily period:

$$E_{th} = \int_{day} \dot{Q}_t(t) \cdot dt$$

$$E_{el} = \int_{day} P_{el}(t) \cdot dt$$

$$\eta_{th} = \frac{\int_{day} \dot{Q}_t(t) \cdot dt}{\int_{day} I(t) \cdot A_{th} \cdot dt}$$

$$\eta_{el} = \frac{\int_{day} P_{el}(t) \cdot dt}{\int_{day} I(t) \cdot A_{PV} \cdot dt}$$

Moreover, by multiplying Eq. (27) and Eq. (28) by the number of days in a month, one can find the total thermal and electric yield, as shown by Eq. (32) and (33), respectively:

$$E_{th,tot} = \sum_{n=1}^{12} E_{th} \cdot n_{day} \tag{32}$$

$$E_{el,tot} = \sum_{n=1}^{12} E_{el} \cdot n_{day} \tag{33}$$

Once these parameters are calculated, it is possible to determine the respective efficiencies as follows:

$$\eta_{\ldots,year} = \frac{E_{th,tot}}{I_{tot} \cdot A_{ther}}$$

$$\eta_{..,year} = \frac{E_{el,tot}}{I_{tot} \cdot A_{PV}}$$

Where I_{tot} is the overall year solar irradiation.

References

[1] Niccolò Aste- Francesco Groppi. Impianti Solari termici. Editoriale Delfino.

[2] W.A. Beckmann and A. Duffie. Solar Engineering of thermal processes, John Wiley and Sons,1980.

CHAPTER 5

Validation of the mathematical model

5.1 Introduction

From the examination of the experimental data and the simulations carried out by means of the mathematical model described in Chapter 4, it is possible to identify a discrepancy between simulated and experimental results. This discrepancy has allowed to identify some constructive faults, mainly due to the bad contact between the absorber plate and the channels where the coolant flows. For this reason, the mathematical model has been modified, in order to introduce an additional thermal resistance. A parametric analysis has also allowed to tune the model and to identify the most appropriate values for this thermal resistance and for other parameters, such us the absorption and the emissivity coefficients of the absorber plate, as well as the fouling coefficient for the outer surface of the glass.

5.2 Performance of the water PVT prototype

In order to evaluate the reliability of the model, the equations previously described in Chapter 4 have been implemented on the simulation tool Mathcad, and the experimental results collected on two sample days (4th and 5th of June 2013) have been compared to the output provided by the software. The first simulations were carried out on an ideal PVT collector whose main parameters are reported in Table 1 in Chapter 4.

In particular, an ideal panel is free from constructive faults. This assumption implies the perfect contact between the absorber plate and the upper surface of the channels and no air gap between the glass layer and the upper surface of the photovoltaic cells. Moreover, the absorption and the emissivity coefficients of the absorber plate are assumed equal to the values available in the literature, i.e. $\alpha_p = \varepsilon_p = 0.9$, and the upper surface of the PVT panel is clean and not shaded.

In addition, the other input data used in the simulation are the outdoor air temperature, the solar irradiation on the collector surface and the fluid temperature at the inlet of the square channels. These parameters were measured on June 4th and 5th 2013 and their temporal distribution is shown in Fig. 1 and Fig. 2, respectively:

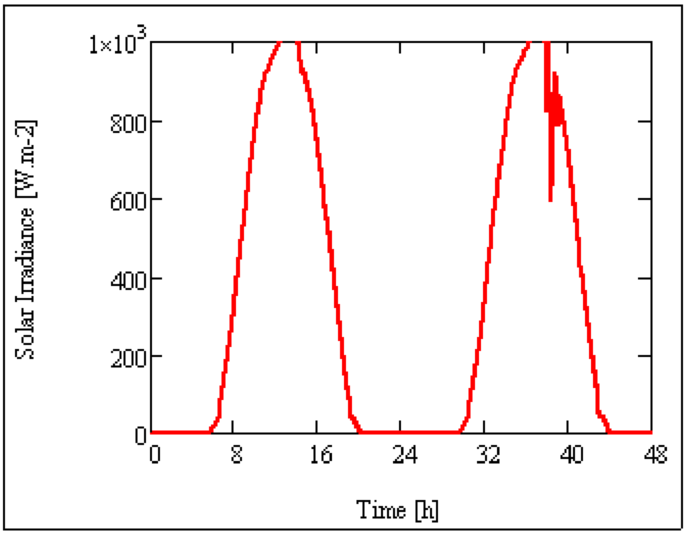

Figure 1: *Solar Irradiance on the PVT surface (June 4th and 5th 2013)*

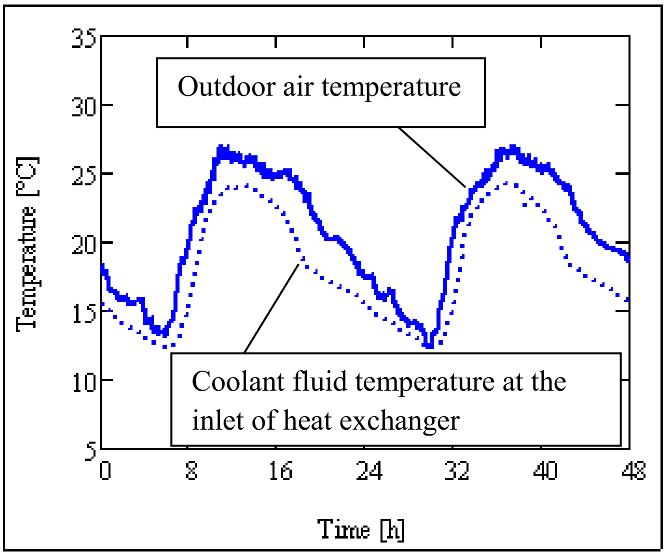

Figure 2: *Outdoor air temperature and inlet fluid temperature on two sample days (June 4th and 5th 2013).*

Once defined the input parameters, the simulation provides the following outputs:

- Outlet water temperature (T_{out_sim})
- Absorber plate temperature (T_{p_sim}),
- Thermal power recovered by the PVT collector (Q_{sim})
- Electric power produced by the PVT collector (P_{el})

The results of this first simulation are reported in Fig. 3, Fig. 4 and Fig. 5. In particular, Fig. 3 shows the comparison between the temporal distribution of the outflow temperatures, both measured (T_{out_1} and T_{out_2}) and simulated (T_{out_sim}). In more detail, T_{out_1} and T_{out_2} represent the temperature trends experimentally detected by means of temperature probes positioned inside the outflow manifold of the two water PVT prototypes. As it is clear from Fig. 3, there is a very good overlapping of the three temperature curves; in correspondence of the sunniest hours, the outlet temperature reaches a maximum value around 26° C. In the same figure, the temporal distribution of the coolant fluid at the inlet manifold is plotted. It allows to evaluate the thermal drop between the inlet and outlet temperatures of the heat exchanger, that is about 2 °C.

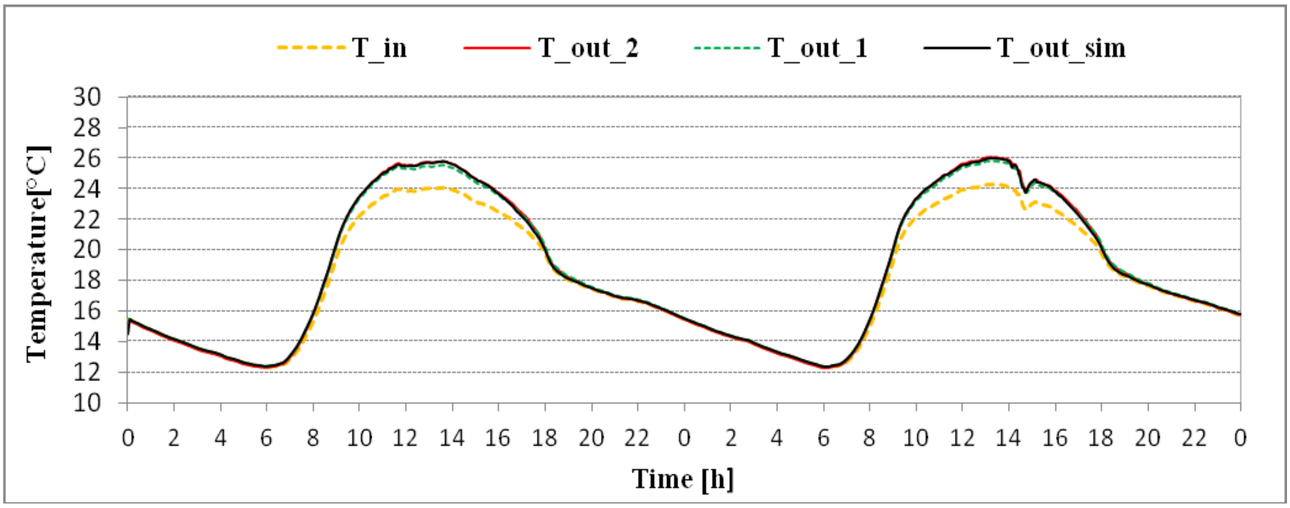

Figure 3: *Comparison between experimental and simulated outlet temperatures (June 4th and 5th 2013)*

On the other hand, Fig. 4 shows the comparison between the temporal distribution of the absorber plate temperatures, both measured (T_{p_1} and T_{p_2}) and simulated (T_{p_sim}). In more detail, T_{p_1} and T_{p_2} represent the temperature trends experimentally detected by means of temperature probes set on the upper surface of two PVT prototypes absorbers. In this case, the prediction of the absorber plate temperature, compared to the experimental values, is not very satisfactory. As one can see from Fig. 4, the absorber surface reaches very high temperature values around 40°C and 42,5° C at 13:00, whereas the calculated maximum surface temperature does not exceed 26°C. The daily average error during the operation time is 7.67°C.

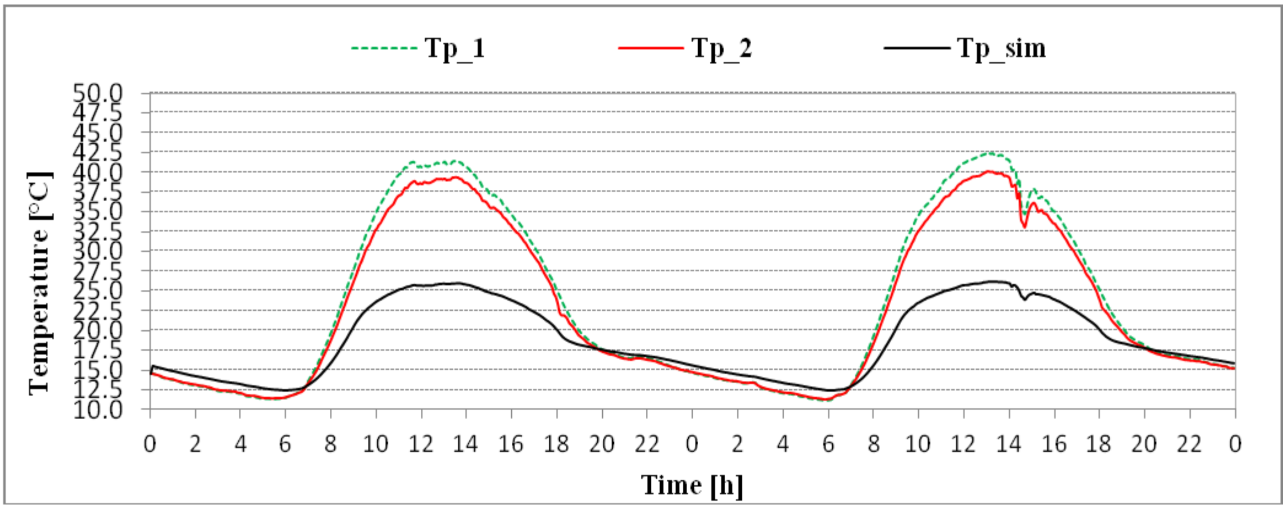

Figure 4: *Comparison between experimental and simulated absorber plate temperatures (June 4th and 5th 2013)*

In addition, a significant mismatch between T_{p_1} and T_{p_2} appears, and it becomes more important around 11:00 and 13:00. As similar oprerating conditions are applied to the two PVT prototypes, these temperature differences are likely to suggest constructive faults, mainly due to the bad contact between the absorber plate and the channels where the coolant flows.

In this context, the thermal conductance has been modified in order to introduce an additional thermal resistance Ra :

$$UA_c = \left[\frac{1}{\alpha \quad 4a \cdot 2L} + \frac{\delta}{\lambda \quad \cdot a \cdot 2L} + Ra \right] \tag{1}$$

In addition, the glass fouling factor f_s is another significant parameter that contributes to reduce the solar radiation absorbed. Its value is always smaller than 1, and difficult to estimate because it depends on the external conditions. It affects the $(\tau\alpha)$ product as follows:

$$\tau\alpha = f_s \cdot \frac{\tau\alpha}{1-(- \chi} \tag{2}$$

Finally, Fig. 5 shows the comparison between the thermal power transferred to the coolant. As expected, the thermal power increases as the outflow temperature increases, and consequently the absorber plate temperature decreases since the heat is removed by the incoming working fluid. The discrepancy between the experimental and simulated output is calculated as follows:

$$error\_\dot{Q} = \frac{\sum_{i=1}^{n} \dot{Q}_{i\_average} - \sum_{i=1}^{n} \dot{Q}_{i\_sim}}{\sum_{i=1}^{n} \dot{Q}_{i-average}} \tag{3}$$

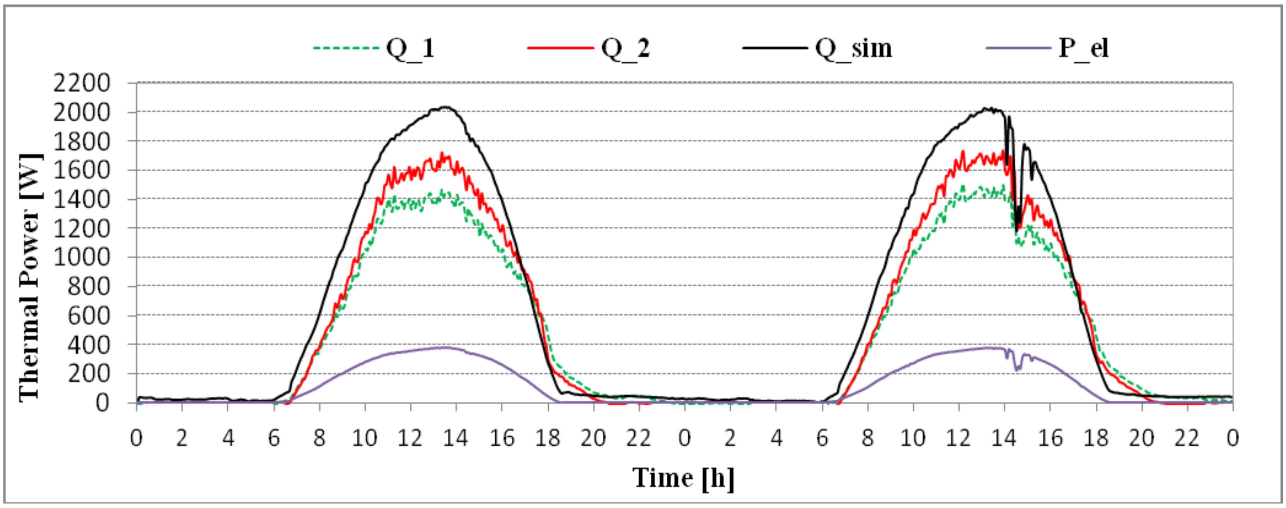

Figure 5: *Comparison between experimental and simulated thermal power (June 4^{th} and 5^{th} 2013)*

In Eq. (3), $\dot{Q}_{i\_average}$ represents the instantaneous average thermal power provided by the two prototypes. The error provided by Eq. (3) is equal to 27.2%. Moreover, in the Fig. 5 the electric power is plotted, and its maximum value is 382 W at 13:30.

5.3 Parametric Analysis

Starting from the results of the simulation carried out on a ideal PVT prototype, the mathematical model has been modified. So a parametric analysis has allowed to tune the model and to identify the values of some parameters, such as the absorber plate emissivity ε_p, the glass fouling coefficient fs, the thermal resistance R_a and the absorber plate coefficient α_p, that minimize the discrepancy between simulated and experimental results.

In this context, ten simulations were carried out on Mathcad, varying only R_a in the range between 0 and 0.1 with a step of 0.01, but keeping all the other input data used in the last simulation. Table 1 resumes the main parameters used in this series of simulations:

parameter	Value
Ra	[0; 0.1] [m·K·W^{-1}]
α_p	0.9
ε_p	0.9
f_s	1

Table 1. *Significant parameters for the simulations*

The assumption $f_s = 1$ corresponds to the case of a perfectly clean glass. The simulation outputs such as the maximum absorber plate temperature, the maximum thermal and electric power and the energy yield for different values of R_a are collected in Table 2.

Ra	**Tp_max**	**Q_max**	**P_el**	**E_term**	**E_el**
[m·K·W^{-1}]	[°C]	[W]	[W]	[kWh]	[kWh]
0	26	2037.4	382	30.63	5.69
0.01	28.6	1989	377.5	30.05	5.64
0.02	31.2	1942.7	372.8	29.38	5.58
0.03	33.7	1900	368.3	28.78	5.53
0.04	36.1	1859.4	364	28.19	5.48
0.05	38.4	1820.3	359.8	27.61	5.43
0.06	40.6	1782.5	355.8	27.05	5.39
0.07	42.7	1745.9	352	26.52	5.34
0.08	44.7	1710.5	348.3	26	5.3
0.09	46.7	1676	344.8	25.5	5.26
0.1	48.5	1643.1	341.4	25.02	5.22

Table 2. *Simulation results for different values of* R_a

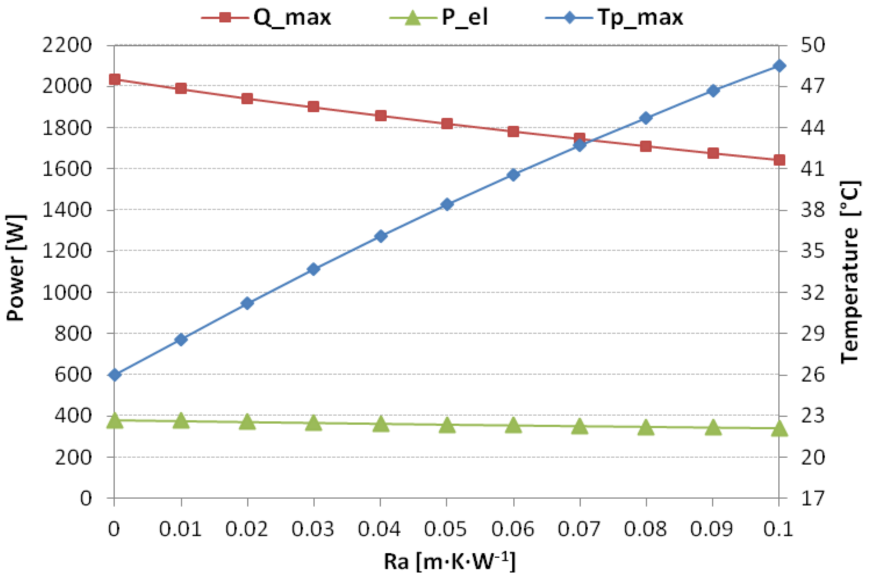

Figure 6. *Simulated performance of the water PVT prototype for different values of* R_a

As it can be seen from Fig. 6, in the ideal case of perfect contact between the upper channel surface and the lower absorber plate surface, which corresponds to $R_a = 0$, the simulated plate temperature is about 26°C, whereas the thermal and electrical power is 2 kW and 400 W, respectively.

However, as long as R_a increases, the thermal conductance decraseses as well as the heat transferred to the coolant fluid, so the absorber plate temperature T_p increases and the thermal and electrical power decrease.

Considering that the experimetal maximum average values of the aborber plate temperature and the total thermal power related to the sample days are 41.3 C and 1620 W, respectively, the discepancy between experimental and simulated data was calculated and plotted in Figure 7.

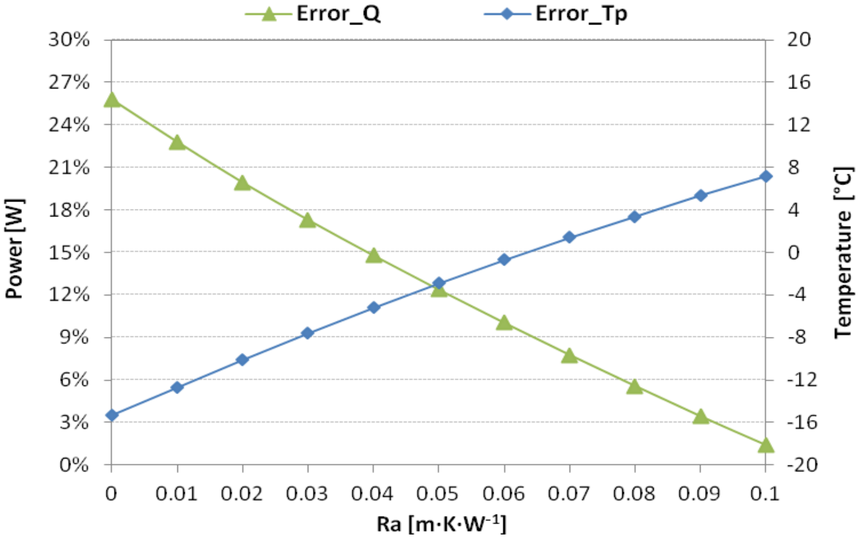

Figure 7. *Error between the simulated and experimental values of thermal power and absorber plate temperature at different values of Ra.*

As shown in Fig, 7, as long as R_a increases the absolute error on the plate temperature increases, while the error on the thermal power decreses; therefore it is necessary to find a compromise between the two solutions. The choice falls on $R_a = 0.07$ [m·K·W^{-1}].

Once investigated how the thermal resistance influences the performance of the PVT system, we can turn our attention to how the absorber plate coefficient α_p and the glass fouling coefficient f_s affect the model validation. The value of α_p can be found as follows:

$$\alpha_p = \frac{\alpha_{PV} \cdot A_{PV} + \alpha_{st} \cdot A_{st}}{A_{tot}} \tag{4}$$

As the ratio between the A_{PV} and A_{tot} is the packing factor *PF,* the equation (4) becomes:

$$\alpha_p = \alpha_{PV} \cdot PF + \alpha_{st}(1 - PF) \tag{5}$$

Considering that α_{PV} and PF values are equal to 0.9 and 0.83, respectively. Eq. (5) is modified as follows:

$$\alpha_p = 0.747 + 0.17 \cdot \alpha_{st} \tag{6}$$

If assigning to α_{st} a value between 0.4 and 0.8, the absorber plate coefficient α_p is equal to 0.88 and 0.82, respectively. Taking into account these considerations, six simulations were carried out varying α_p in the range between 0.8 and 0.9 with step of 0.02.

The numerical results related to T_{p_max}, Q_{max}, P_{el}, E_{term}, E_{el} at different values of α_p, provided by the simulations, are collected in Table 3.

α_p	T_{p_max}	Q_{max}	P_{el}	E_{term}	E_{el}
[-]	[°C]	[W]	[W]	[kWh]	[kWh]
0.8	40.6	1550.3	355.7	23.6	5.38
0.82	41.1	1590	355	24.2	5.375
0.84	41.5	1629.4	354.2	24.8	5.37
0.86	41.9	1668.5	353.5	25.4	5.36
0.88	42.3	1707.3	352.7	26.0	5.35
0.9	42.7	1745.9	352	26.5	5.34

Table 3. *Simulation results at different values of* α_p.

In Figure 8, the performance trends are shown. As expected, as long as the absorber plate coefficient α_p increases, the absorber plate temperature and the thermal power increase too. On the contrary, the electric power slightly decreases at higher α_p values.

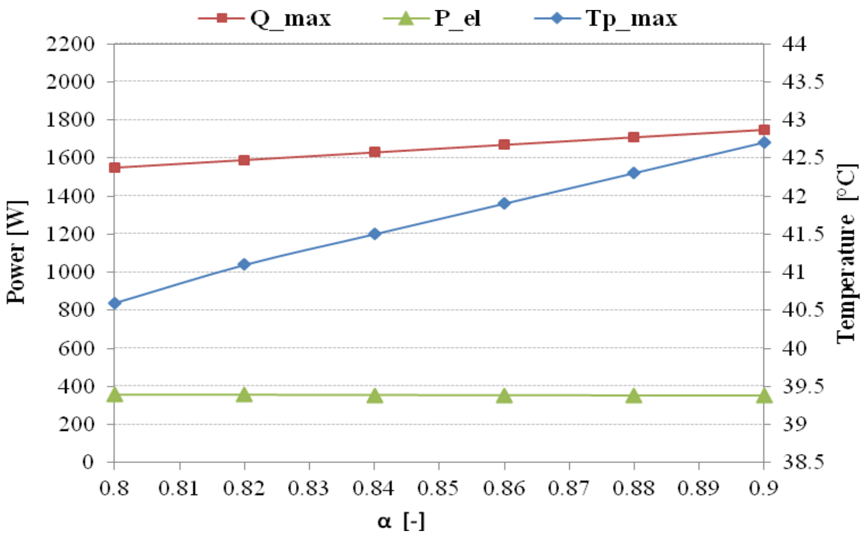

Figure 8. *Simulated performance of the water PVT prototype at different values of* α_p

The comparison between the simulated and the experimental output (Fig. 9) shows that the mismatch on Q_{max} and T_p increase when increasing α_p. In particular, one can observe that the *Error_Q* increases much more rapidly than the *Error_Tp*.

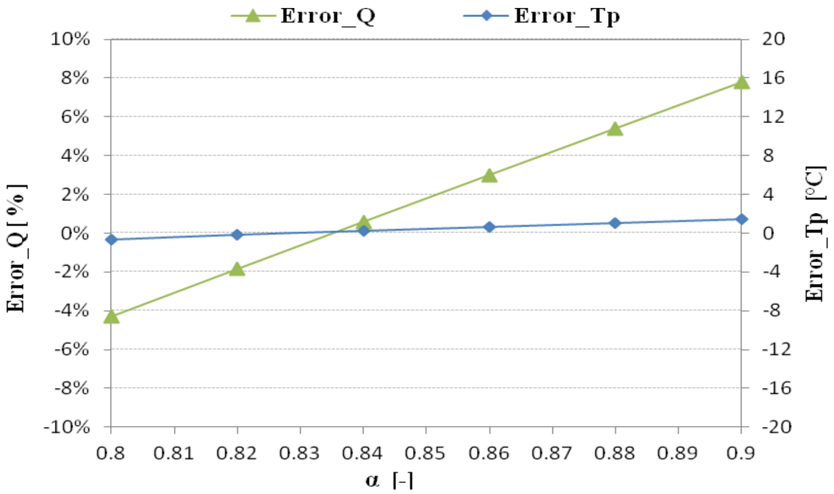

Figure 9. *Error between simulated and experimental values of thermal power and absorber plate temperature at different values of* α_p

As regards the fouling coefficient f_s, other six simulations were performed, by varying this parameter in the range between 0.9 and 1 with a step of 0.02. As shown from the results collected in Table 4, this parameter has a great influence on the PVT performance.

fs	$T_{p\ max}$	Q_{max}	P_{el}	E_{term}	E_{el}
[-]	[°C]	[W]	[W]	[kWh]	[kWh]
0.9	40.6	1544	355.8	23.5	5.39
0.92	41	1584.5	355.1	24.1	5.38
0.94	41.4	1624.9	354.3	24.7	5.37
0.96	41.8	1665.3	353.5	25.3	5.36
0.98	42.3	1705.6	352.8	25.9	5.35
1	42.7	1745.9	352	26.5	5.34

Table 4. *Simulation results at different values of* f_s.

In addition, as shown in Fig. 10 and Fig. 11, at different values of f_s the simulations provide performance trends and mismatch between the simulated and experimental output very similar to those presented in previous simulations. So one can conclude that the variation of α_p and *fs* affect the validation analysis of the mathematical model in a similar fashion.

Finally, $f_s = 0.95$ value is chosen, because it simulates an intermediate glass fouling condition and minimizes the error.

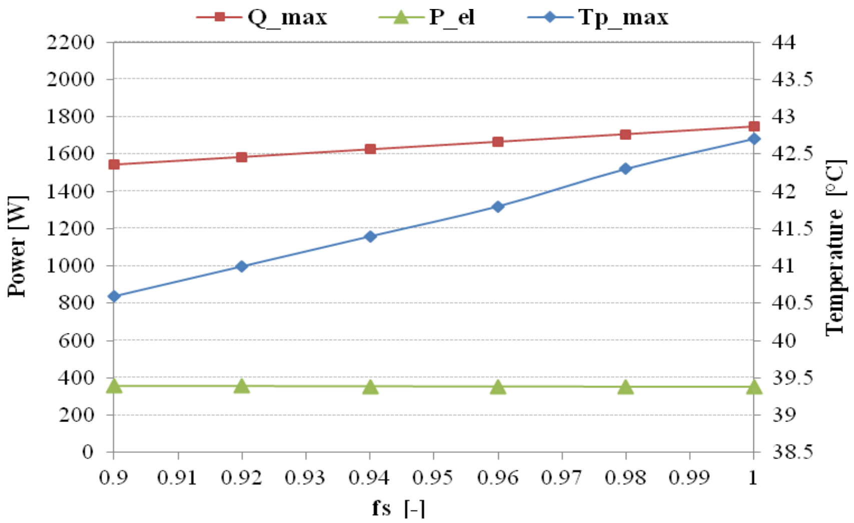

Figure 10. *Simulated performance of the water PVT prototype at different values of* f_s

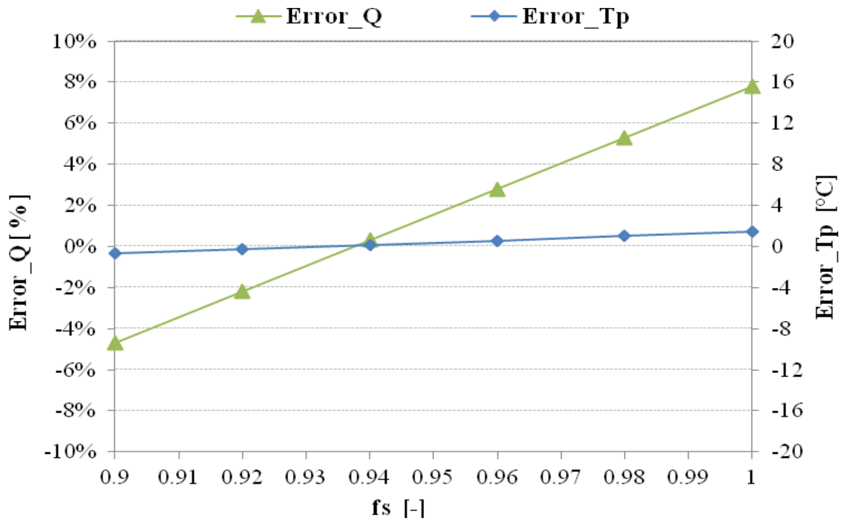

Figure 11. *Error between the simulated and experimental values of thermal power and absorber plate temperature at different values of* f_s

On the contrary, the variation of the absorber plate emissivity ε_p in the range between 0.86 and 0.9, with a step corresponding to 0.01, does not influence the PVT performance and the comparison between simulated and experimental output, as reported in Table 5, Fig. 12 and Fig. 13.

ε_p	Tp_max	Q_max	P_el	E_term	E_el
[-]	[°C]	[W]	[W]	[kWh]	[kWh]
0.86	42.7	1750.4	351.9	26.6	5.34
0.87	42.7	1749.2	351.9	26.6	5.34
0.88	42.7	1748.1	352	26.6	5.34
0.89	42.7	1747	352	26.6	5.34
0.9	42.7	1745.9	352	26.5	5.34

Table 5. *Simulation results at different values of* ε_p

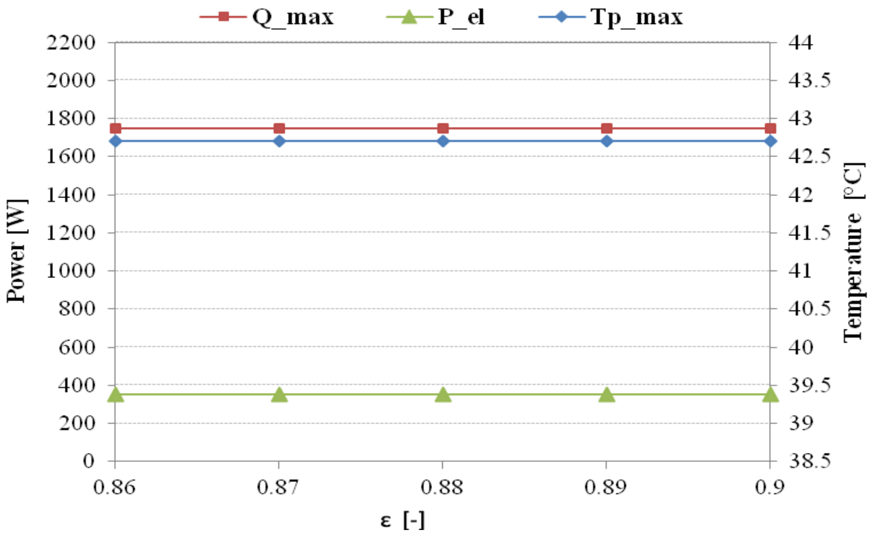

Figure 12. *Performance of the water PVT prototype at different values of* ε_p

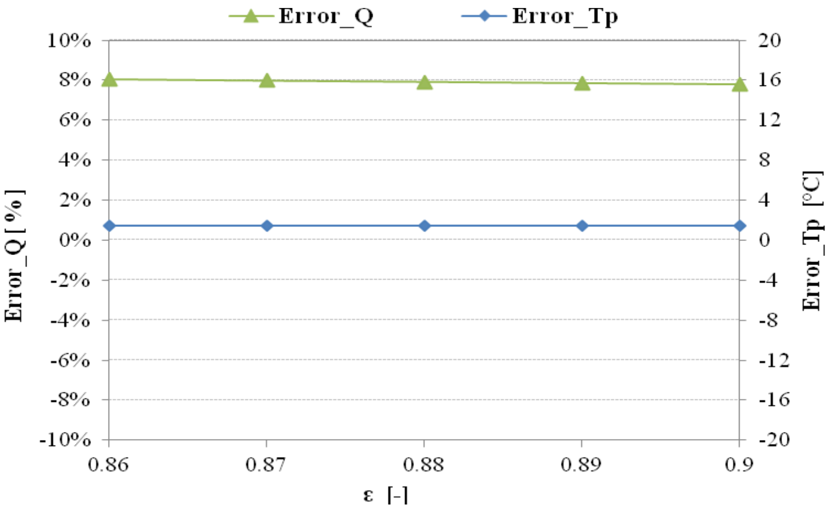

Figure 13. *Error between the simulated and experimental values of thermal power and absorber plate temperature at different values of* ε_p

According to these results, $\varepsilon_p = 0.9$ is chosen, that is the value commonly cited in the literature.

5.4 Numerical code optimization and results

Finally, the mathematical model has been optimized, in order to determine the set of values that minimize the discrepancy between simulated and experimental results. The final parameters provided by this analysis are shown in Table 6:

Parameters	***Values***
Ra	0.08 [$m \cdot K \cdot W^{-1}$]
α_p	0.87
ε_p	0.9
fs	0.95

Table 6. *Final parameters provided by the optimimization process*

Once identified the set of parameters that have allowed to validate the mathematical model, the comparison between the experimental and simulated output is shown in Fig. 14 and Fig. 15.

In particular, Fig. 14 shows the comparison between the experimental absorber plate temperature trends related to two tested PVT prototypes, and those provived by the mathematical model. In both cases, the input data are related to two sample days (4th and 5th June 2013).

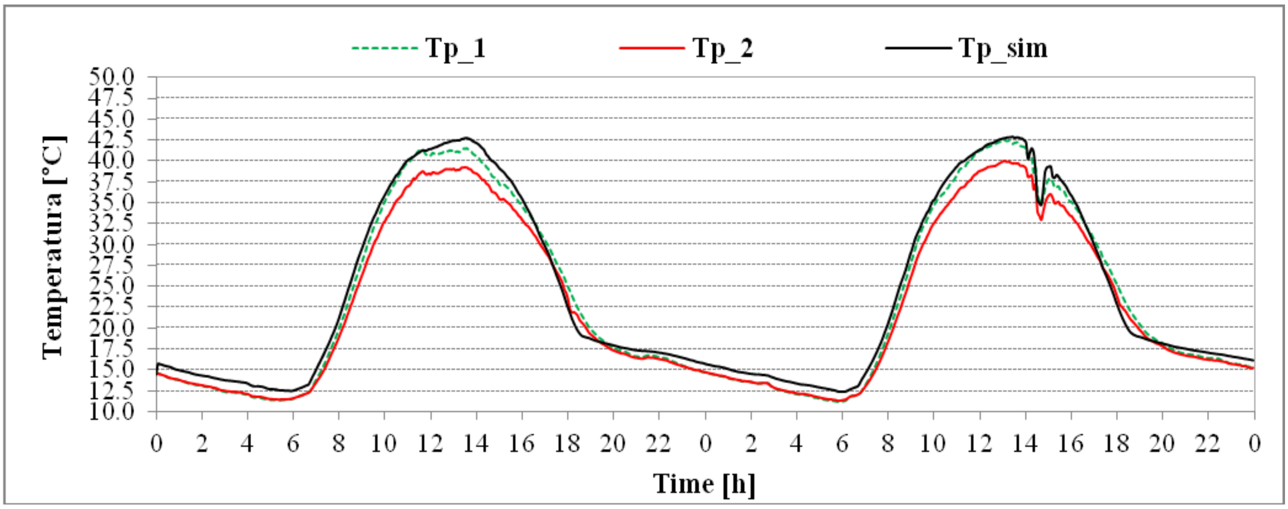

Figure 14. *Final comparison between experimental and simulated absorber plate temperatures (June 4th and 5th 2013)*

In addition, the maximum superficial temperature reached by the two prototypes are 42.5°C and 40°C, respectively, detected around the 13:00 on June 5th. The average error on the calculation of the peak temperature is just around 1.6°C.

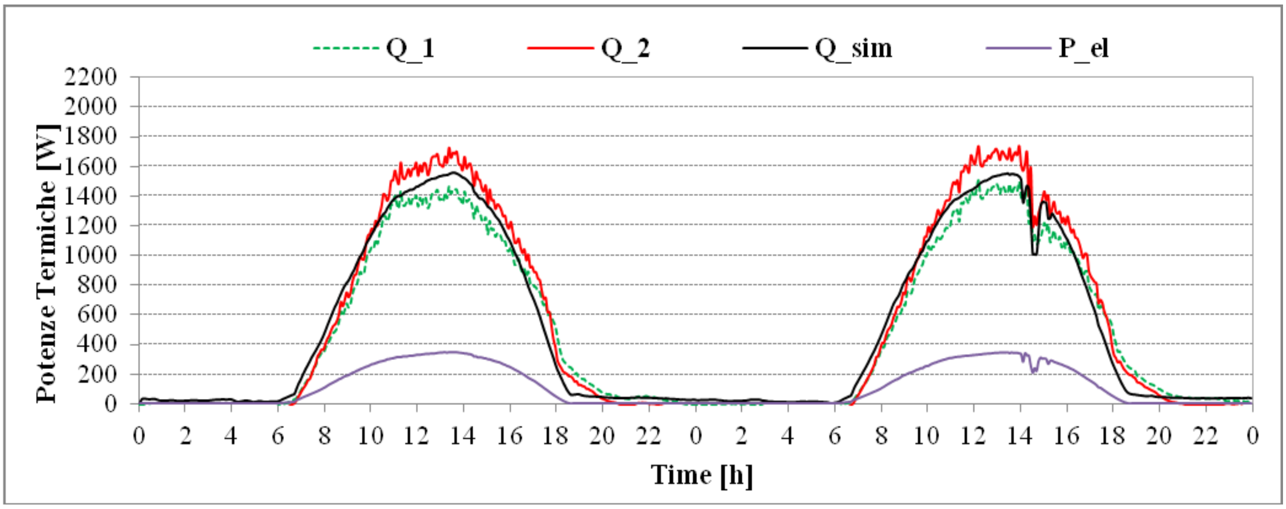

Figure 16. *Final comparison between experimental and simulated thermal power trends (June 4th and 5th 2013)*

Furthermore, as one can see from Fig. 16, the simulated profile of the thermal power has intermediate values between the two experimental trends *Q_1* and *Q_2*. In particular, the average experimental peak thermal power is 1620 W, while the peak simulated thermal power is 1558 W. So the error on the thermal power is about 1.4%. In the same figure the electric power is plotted, and its maximum value is 351.6 W at 13:30 on June 4th.

Finally, Table 7 summarizes the errors on the calculation of the absorber plate temperature and the thermal power, both before and after having tuned the mathematical model. It is clear that the optimization conducted in this chapter provided very good results in terms of reliability of the simulations.

	Ideal PVT system	***Real PVT system***
$Average\_error\_T_{abs}$	7.67 °C	1.58 °C
$Error\_\dot{Q}$	27.2%	1.43%

Table 7. *Errors related by ideal and real PVT systems*

It must be reminded that, in all simulations, we do not take into account the actual variations of the water flow rate, whose fluctuations are reported in Chapter 3, and the actual wind speed. This may be a further cause of the slight discrepancy between experimental and simulated output.

Starting from the results of this investigation, it is possible to envisage the construction of a new PVT panel lacking any construction fault, and whose performance are very promising and significantly better than the prototype tested so far.

CHAPTER 6

Performance of the real and improved PVT collector on an annual basis

6.1 Introduction

The mathematical model presented in the previous section, concerning the energy performance of the PVT solar collector, is basically founded on the First Law of Thermodynamics. According to this approach, the thermal and electric energy collected by the PVT system can be evaluated under a merely metric criterion. In order to evaluate the actual thermodynamic quality, the exergy analysis based on the Second law of Thermodynamics allows a wider view than that provided by a simple energy analysis.

6.2 Results of Energy analysis

The set of equations presented in Section 4 allows, at each time step, the calculation of the output parameters to describe the energy performance of the PVT collector:

- absorber temperature, T_p.
- outlet fluid temperature, T_{out}.
- overall useful thermal power, Q_{tot}.
- electricity production, P_{el}.

Here, the mentioned mathematical model has been applied to the real and improved prototype of water-cooled PVT collector in order to assess its potential performance in terms of annual thermal and electric energy production. In more detail, the real PVT system is a collector that presents some construction faults which influence the value of the thermal resistance R_a. The improvement of this system has led to a better PVT collector, whose significant parameters are reported in Table 1 together with those of a real panel.

Parameters	***Real PVT Collector***	***Improved PVT collector***	***u. m.***
Ra	0.08	0	$[m \cdot K \cdot W^{-1}]$
α_p	0.87	0.9	[-]
ε_p	0.9	0.9	[-]
fs	0.95	1	[-]

Table 1. *Significant parameters for the real and improved PVT collector.*

The calculation has been performed on a monthly basis, with reference to a representative day for each month of the year. The weather data refer to the city of Catania (Italy, latitude 37°30'), and correspond to those available on the database of the software tool EnergyPlus. In particular, the values of the solar irradiance I refer to a surface due south and to a tilt angle β = 20° on the horizontal plane, that is the real configuration of the prototype installation. The calculation time step is Δt = 60 s; thus, a linear interpolation has been done on the weather data, that are available on an hourly basis.

The other geometrical and thermophysical parameters used in the calculation are the same reported in section 4. The water mass flow rate is 80 [$kg \cdot h^{-1} \cdot m^{-2}$], which belongs to the typical range adopted in the design of flat plate solar collectors (40–120 [$kg \cdot h^{-1} \cdot m^{-2}$]); this value implies a velocity v_w = 0.18 [$m \cdot s^{-1}$] for the water flowing inside the channels. Furthermore, in order to prevent an improper management of the system, the circulation of the fluid inside the PVT collector is not activated when the solar irradiance on the collector plane is too low, i.e. below 150 [$W \cdot m^{-2}$]. As concerns the water inlet temperature T_{in}, in the calculation it is kept constant equal to 20°C. Table 2 shows the maximum monthly values of the absorber plate and outflow temperatures calculated for the real and improved PVT panels. The profiles of the monthly absorber plate temperatures in both PVT systems are reported in Fig. 1.

	Real PVT (T_{in} = 20°C)		**Improved PVT (T_{in} = 20°C)**	
	Tp max	***Tout max***	***Tp max***	***Tout max***
	[°C]	[°C]	[°C]	[°C]
Jan	25.5	21	22	21.3
Feb	28.2	21.5	22.9	21.9
Mar	31.6	22.2	24.1	22.7
Apr	35.1	22.8	25.3	23.5
May	38.1	23.4	26.3	24.2
Jun	39.9	23.7	27	24.6
Jul	41.9	24.1	27.6	25
Aug	40.6	23.8	27.1	24.7
Sep	36.8	23.1	25.8	23.8
Oct	31.9	22.2	24.1	22.7
Nov	27.8	21.5	22.7	21.8
Dec	25.0	20.9	21.8	21.2

Table 2. *Maximum monthly outputs of the absorber plate and outflow temperatures.*

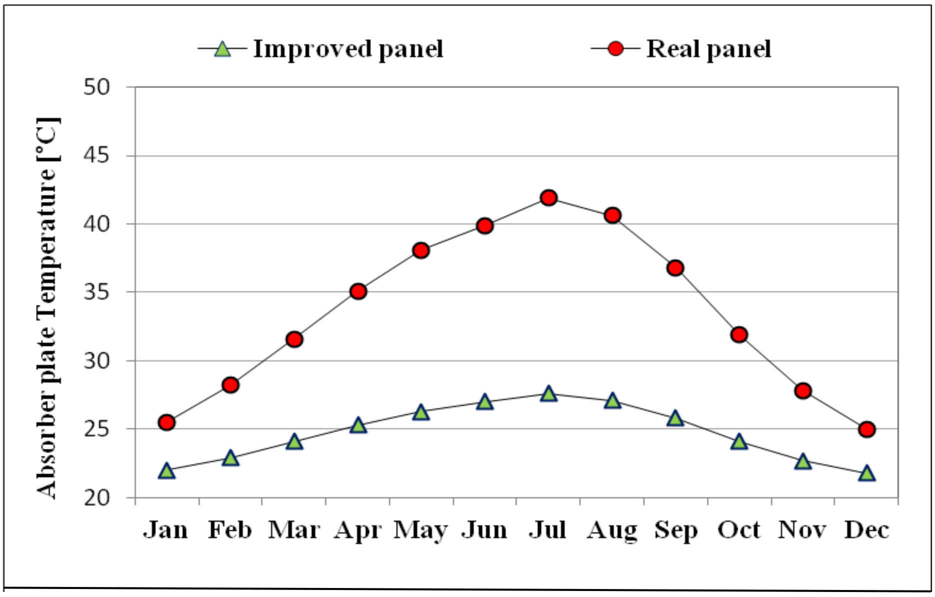

Figure 1.*Absorber plate temperatures of the real and improved PVT systems.*

When T_{in}=20°C, one can observe that the absorber plate temperature of the improved PVT panel is always higher than that of the real PVT system. This result seems to be positive for the cells, whose efficiency can benefit a lot from a temperature far below that usually occurring in common PV modules. In addition, the maximum surface temperatures of the improved and real systems recorded during the overall period of investigation are 27.6°C and 42 °C respectively.

Furthermore, Table 3 reports the monthly values of the thermal electricity production of both real and improved PVT collectors.

	Solar radiation available	**Real PVT (T_{in} = 20°C)**		**Improved PVT (T_{in} = 20°C)**	
		Thermal energy gain	***Electric energy gain***	***Thermal energy gain***	***Electric energy gain***
	[kWh·day^{-1}]	[kWh·day^{-1}]	[kWh·day^{-1}]	[kWh·day^{-1}]	[kWh·day^{-1}]
Jan	6.1	1.58	0.67	2.01	0.68
Feb	8.6	2.61	0.94	3.28	0.96
Mar	12.0	4.13	1.30	5.17	1.33
Apr	15.8	5.95	1.70	7.42	1.76
May	18.6	7.60	1.99	9.44	2.07
Jun	20.1	8.83	2.13	10.90	2.23
Jul	20.7	9.56	2.18	11.71	2.30
Aug	18.7	8.69	1.98	10.60	2.08
Sep	14.8	6.66	1.58	8.15	1.65
Oct	10.5	4.23	1.13	5.22	1.17
Nov	7.2	2.51	0.79	3.12	0.80
Dec	5.2	1.37	0.57	1.73	0.58

Table 3. *Monthly energy results calculated for the real and improved PVT system.*

(a)

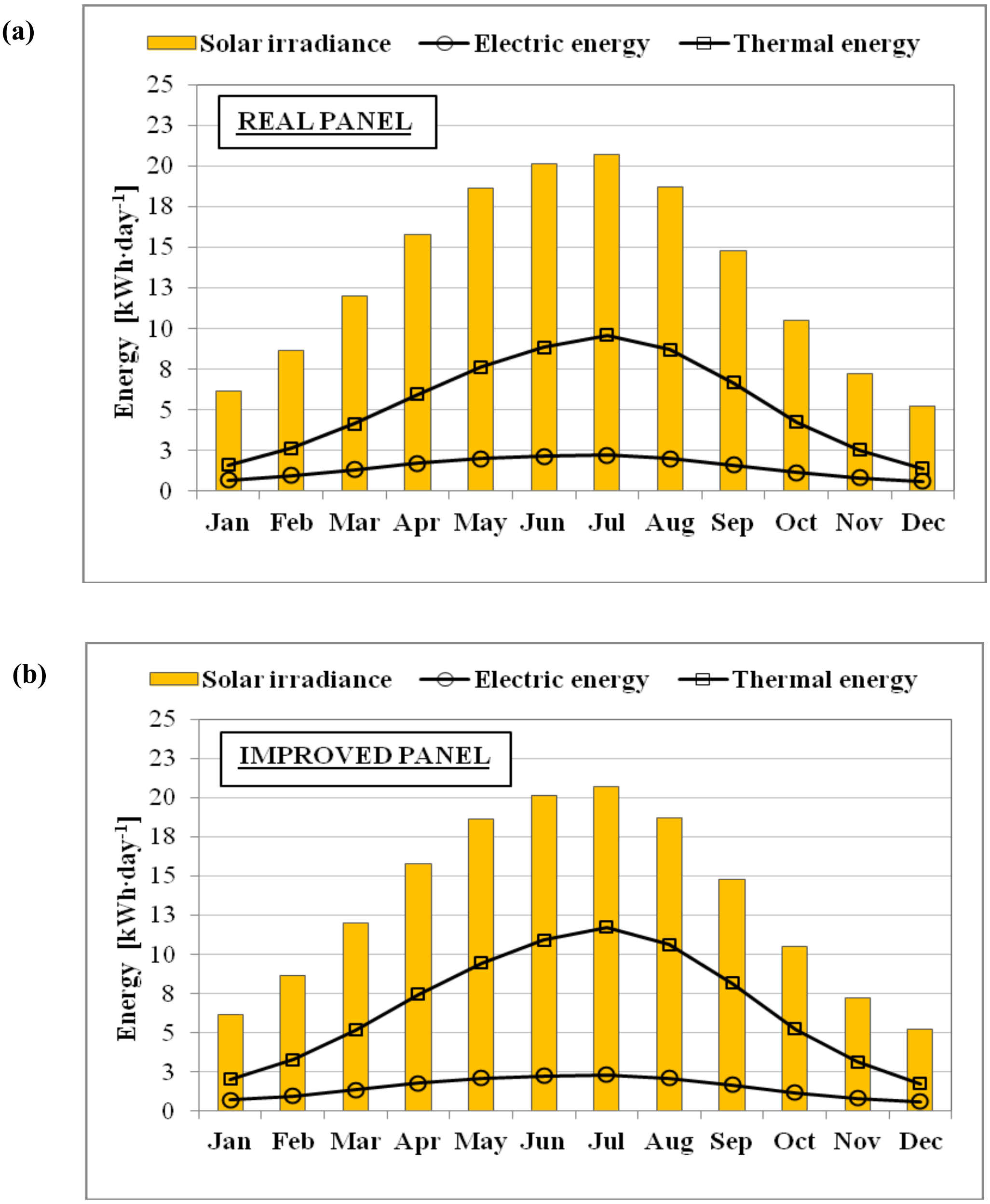

Figure 2. *Monthly electric and thermal energy yields.(a)real PVT system; (b) improvement PVT system.*

As shown in Fig. 2, the monthly electric energy profiles are very similar in both PVT systems. On the other hand, the monthly thermal energy of the improved panel largely exceeds 10 [kW·h·day^{-1}], whereas the thermal energy of the real panel does not overtake this value, even when the solar irradiance is at its height in July.

In Table 4 are reported the monthly outputs of the energy efficiency of both the real PVT system and the improved PVT system.

	Real PVT Panel			**Improved PVT Panel**		
	η_{th}	η_{el}	$\eta_{overall}$	η_{th}	η_{el}	$\eta_{overall}$
	[-]	[-]	[-]	[-]	[-]	[-]
Jan	25.9%	13.3%	36.9%	33.0%	13.5%	44.1%
Feb	30.3%	13.2%	41.3%	38.1%	13.5%	49.3%
Mar	34.4%	13.1%	45.3%	43.1%	13.4%	54.2%
Apr	37.7%	13.0%	48.4%	47.0%	13.4%	58.1%
May	40.9%	12.9%	51.5%	50.8%	13.5%	61.9%
Jun	43.9%	12.8%	54.5%	54.2%	13.4%	65.3%
Jul	46.2%	12.7%	56.7%	56.6%	13.4%	67.7%
Aug	46.5%	12.8%	57.1%	56.7%	13.4%	67.8%
Sep	45.0%	12.9%	55.7%	55.1%	13.5%	66.2%
Oct	40.3%	13.1%	51.1%	49.7%	13.4%	60.8%
Nov	34.9%	13.2%	45.8%	43.3%	13.5%	54.5%
Dec	26.3%	13.3%	37.3%	33.3%	13.4%	44.4%

Table 4. *Monthly performance of the real and improved PVT systems*

Other interesting information are shown by the Fig.3 , where these numerical results are plotted for the case $T_{in} = 20°C$.

In both cases, one can learn that the expected electric energy efficiency keeps almost constant.

From the comparison of the results provided by the simulations of the two PVT systems one can observe that, in the case of the real PVT system the average monthly electric efficiency range from 12.7% to 13.3%. On the other hand, for the improved PVT system the expected electric energy efficiency keeps almost constant, as it oscillates between 13.4% and 13.5%: the lowest values occur in summer, when the overheating of the PV cells is more pronounced.

Moreover, the expected thermal performance in both systems is highly penalized in winter, when the average thermal efficiency is between 20% and 30%, or 30% and 40%, for the real panel and the improved panel , respectively. In the case of the improved panel, it hardly exceeds 50% in the period May-October, whereas it does not overtake 47% in the real panel.

The overall expected energy efficiency shows a similar trend, with a peak value around 60% and 70% in July and August , for real collector and improved collector, respectively. As expected, one can conclude that the improved panel shows better performance trends than the real systems.

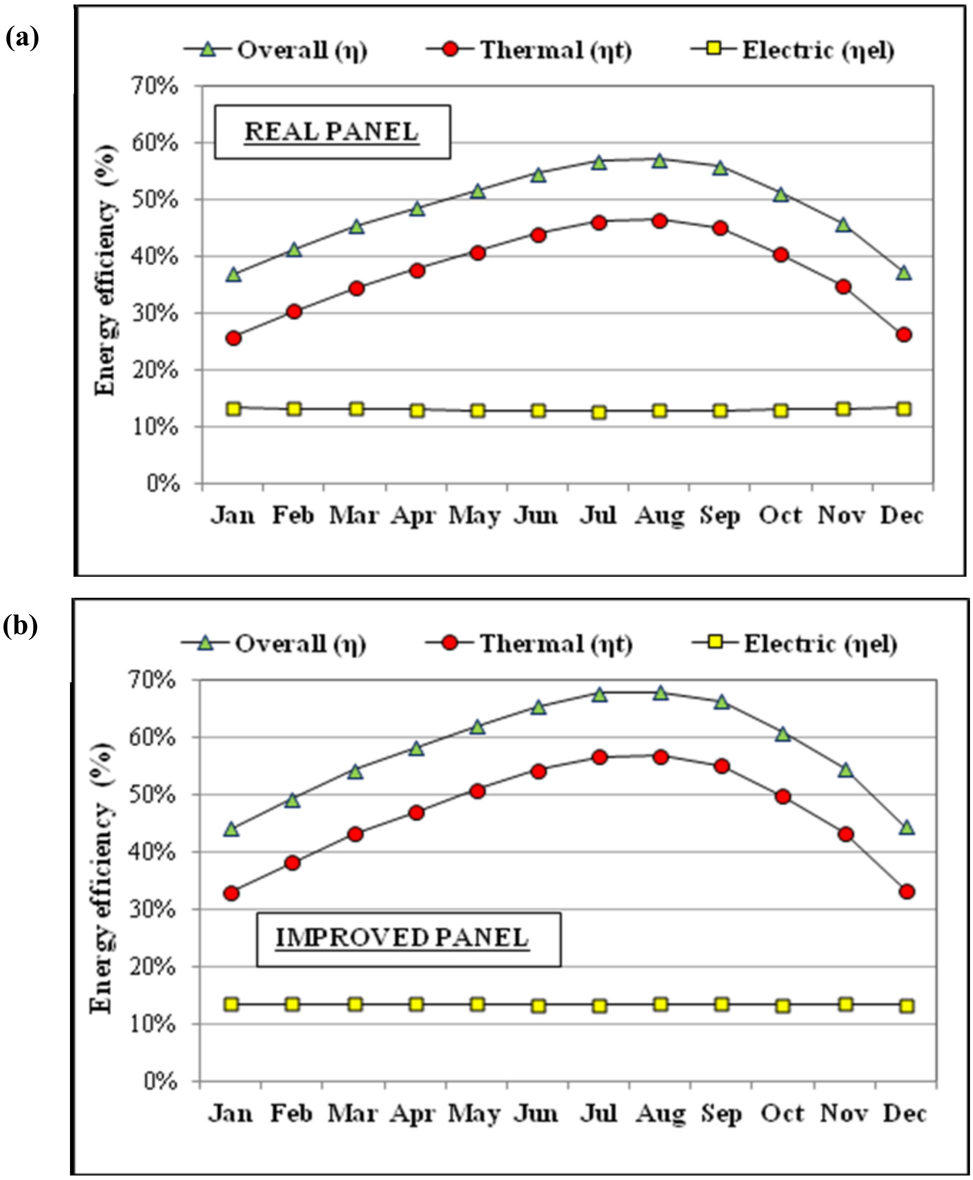

Figure 3. *Average monthly energy efficiency of the PVT collectors.*
(a) Real Panel; (b) Improved Panel.

Finally, Fig. 4 shows the effect of the water inlet temperature on the annual energy efficiency for both systems. According to these results, it is highly recommended to operate the PVT collector at low temperatures, since the reduction in the annual overall efficiency is by about 4% and 5% every 5°C of temperature increase, for real collector and improved collector , respectively.

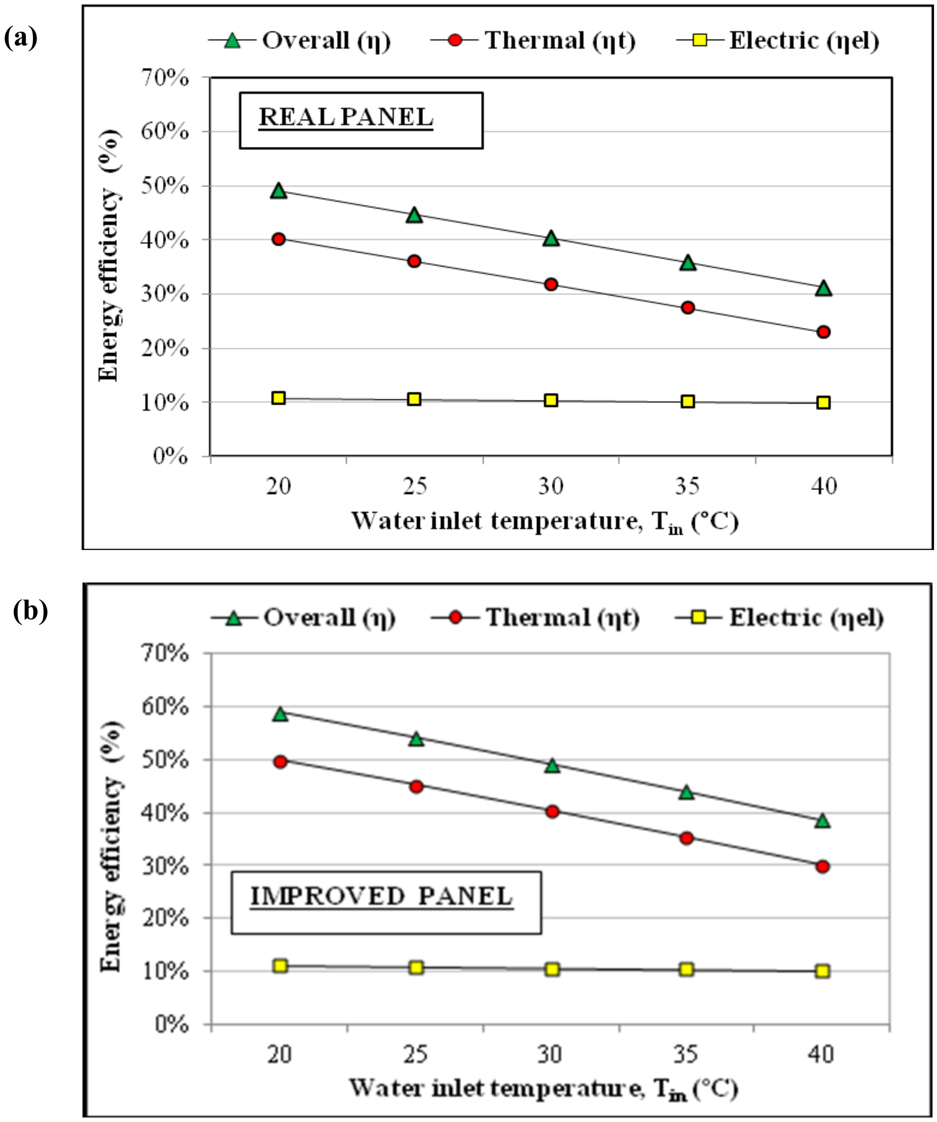

Figure 4. *The average annual energy efficiency of the PVT collector as a function of the (constant) water inlet temperature. (a) Real PVT system; (b) Improved PVT system.*

6.3 Governing equations for the exergy analysis

To understand how much useful is the heat, as a function of the temperature at which it is available, the most appropriate approach is the Second Law of Thermodynamics, and the most suitable tool is the exergy method [1]. Indeed, only by reducing all forms of energy to a common basis, e.g. mechanical work, it is possible to make comparisons in terms of usefulness, in a rational way. Exergy is a well-known concept in the context of Energy Engineering Systems, as it measures the equivalent mechanical work of any process and any form of energy, or energy source (e.g. heat) or carrier (e.g. electricity). Now, while electric energy is pure exergy, thermal energy has an exergy content that depends on the temperature at which heat is made available: this issue is particularly relevant in PVT systems, where the energy yield is highly influenced by the temperature level of the system.

In the recent scientific literature several works have already tackled the exergy analysis of both water-cooled and air-cooled PVT collectors. However, a certain discrepancy emerges when dealing with the evaluation of the exergy content of a mass flow in relation to its temperature level. Eqs. (1) and (2) report the two formulations more frequently adopted in the literature:

$$\dot{E}_Q = \dot{m}_w \cdot c_{pw} \cdot (T_{out} - T_{in}) \cdot \left(1 - \frac{T_0}{T_{out}}\right) \tag{1}$$

$$\dot{E}_Q = \dot{m}_w \cdot \left[(h_{out} - h_{in}) - T_0 \cdot (s_{out} - s_{in})\right] = \dot{m}_w \cdot \left[(T_{out} - T_{in}) - T_0 \cdot \ln \frac{T_{out}}{T_{in}}\right] \tag{2}$$

Now, Eq. (1) basically contemplates that the useful product of the PVT collector is the thermal power extracted by the fluid from the absorber plate, and that this thermal power is made available at the outlet temperature T_{out}. To this aim, the Carnot Factor (1 - T_0/T_{out}) is introduced, where T_0 is the reference temperature at which the exergy content of the thermal power is zero (dead state). This approach is adopted, amongst other authors, by Fujisawa and Tani [2], Joshi and Tiwari [3], Chow et al. [4], Dubey and Tiwari [5], Saidur et al. [6], Zhang et al. [7], Agrawal and Tiwari [8], [9], [10].

On the other hand, Eq. (2) is based on the Gouy-Stodola Theorem [11], and measures the increase in the exergy content of the fluid related to its temperature lift from T_{in} to T_{out}. This approach is followed in a relatively lower number of publications (Coventry and Lovegrove [12]; Duran Sahin et al. [13]; Hepbasli [14]). In our, the approach of Eq. (2) is more rigorous, and is the one that will be adopted in the following.

Moreover, Eq. (2) can be formally rewritten in the same form as for Eq. (1), just replacing – in the Carnot Factor – the outlet temperature T_{out} with the *Mean Thermodynamic Temperature* T_m. The latter, for a liquid (or ideal gas) flow experiencing a heating process from the inlet temperature T_{in} to the outlet T_{out} temperature, can be expressed as:

$$T_m = \frac{h_{out} - h_{in}}{s_{out} - s_{in}} = \frac{T_{out} - T_{in}}{\ln\left(\frac{T_{out}}{T_{in}}\right)} \tag{3}$$

Therefore:

$$\dot{E}_Q = \dot{m}_w \cdot c_{pw} \cdot (T_{out} - T_{in}) \cdot \left(1 - \frac{T_0}{T_m}\right) \tag{4}$$

As to the exergy of the electric power, it is to remind that it is pure exergy. Hence:

$$\dot{E}_{el} = P_{el} = \eta_{PV} \cdot I_{sol} \cdot A_{PV} \tag{5}$$

Another key point that is not unambiguously addressed in the literature is the definition of the reference temperature T_0. In fact, this temperature is generally assumed equal to the actual variable outdoor temperature, as suggested by Duran Sahin et al. [13], Hepbasli [14], Chow et al. [4], Agrawal and Tiwari [10]; however, Pons [15] stated that it is not correct to consider a variable T_0, as this would introduce a series of thermodynamic contradictions.

Therefore, a constant T_0 should be assumed. As concerns the choice of such a constant value, here again there is no agreement amongst the authors: as an example, Joshi and Tiwari [3] adopted $T_0 = 20$ °C, whereas Coventry and Lovegrove [12] chose $T_0 = 25$ °C. On the other hand, Fujisawa and Tani [2] opted for the average monthly outdoor temperature, calculated according to statistical data. In this study, the reference temperature T_0 is defined on the basis of what suggested by Pons [15], i.e. it corresponds to the minimum outdoor temperature registered during any given month.

Finally, one needs to assess the exergy content of the solar radiation incident on the collector surface. To this aim, in the scientific community it is common opinion that solar radiation cannot be considered as pure exergy, therefore an appropriate conversion coefficient ψ_s should be applied to solar irradiance to calculate its exergy content:

$$\dot{e}_{sol} = \psi_s \cdot I_{sol} \tag{6}$$

Now, the most consolidated formulation for the conversion coefficient ψ_s is represented by Eq. (7), proposed by Petela ([16], [17]).

$$\psi_s = 1 - \frac{4}{3} \cdot \frac{T_0}{T_{sol}} + \frac{1}{3} \cdot \left(\frac{T_0}{T_{sol}} \right)^4 \tag{7}$$

Here, the author assimilated extra-atmospheric solar radiation to undiluted blackbody radiation, and used a thermodynamic analogy with a piston-cylinder system exploiting an amount of heat corresponding to the solar radiation absorbed by an ideal blackbody. In Eq. (7), $T_{sol} = 5760$ K is the apparent solar temperature. On the other hand, some authors, as Duran Sahin et al. [13] and Chow et al. [4], prefer an alternative approach, firstly proposed by Jeter [18], where the conversion coefficient is defined just like a Carnot Factor:

$$\psi_s = 1 - \frac{T_0}{T_{sol}} \tag{8}$$

According to this approach, the degradation of solar radiation into heat is not taken into account, and the ideal thermal engine introduced in the thermodynamic analogy receives an amount of heat corresponding to the solar radiation coming from the sun, as also highlighted by Saloux et al. [19]. However, Pons [20] disapproves both approaches, since they do not make a proper distinction between direct and diffuse radiation. According to his investigation, the conversion coefficient should be applied to the daily insolation, and its value should range from 0.68 (overcast condition) to 0.91 (clear sky), i.e. lower than the values obtained by Petela and Jeter ($\psi_s = 0.93 – 0.95$). In this study, the more consolidated approach proposed by Petela will be used, see Eq. (7).

Finally, on the basis of the previously stated model, it is possible to define the average exergy efficiency of both the electricity production (ξ_{el}) and the heat recovery (ξ_t), as well as the overall exergy efficiency ξ of the PVT collector, see Eqs. (9) and (10):

$$\xi_t = \frac{\dot{E}_Q}{\psi \; I_{sol} \cdot A_p} \qquad \xi_{el} = \frac{\dot{E}_{el}}{\psi \; I_{sol} \cdot A_{PV}} \tag{9}$$

$$\xi = \frac{\dot{E}_Q + \dot{E}_{el}}{\psi \cdot I_{sol} \cdot A_p} = \xi_t + PF \cdot \xi_{el} \tag{10}$$

6.4 Results of exergy analysis

The energy analysis presented in the previous section clearly suggests to operate the PVT collector at temperatures as low as possible, so as to get high overall energy efficiencies. However, since they are based just on the First Law of Thermodynamics, these results make no reference to the actual thermodynamic quality of the different forms of energy (electric and thermal) produced by the PVT collector.

To this aim, the concept of exergy (i.e. available energy) should be used, as mentioned in paragraph 6.2. Now, the results of the exergy analysis of two different PVT systems – the real panel and the improved panel – may seem quite disappointing if compared with those of the energy analysis, as shown in Table 5.

	Solar Exergy	**Real PVT (T_{in} = 20°C)**		**Improved PVT (T_{in} = 20°C)**	
		Thermal Exergy	***Electric Exergy***	***Thermal Exergy***	***Electric Exergy***
	[kWh·day^{-1}]	[kWh·day^{-1}]	[kWh·day^{-1}]	[kWh·day^{-1}]	[kWh·day^{-1}]
Jan	5.7	0.07	0.67	0.09	0.68
Feb	8.0	0.12	0.94	0.16	0.96
Mar	11.2	0.20	1.30	0.25	1.33
Apr	14.7	0.23	1.70	0.30	1.76
May	17.4	0.20	1.99	0.25	2.07
Jun	18.8	0.11	2.13	0.15	2.23
Jul	19.3	0.06	2.18	0.09	2.30
Aug	17.5	0.02	1.98	0.04	2.08
Sep	13.8	0.06	1.58	0.08	1.65
Oct	9.8	0.11	1.13	0.14	1.17
Nov	6.8	0.08	0.79	0.10	0.80
Dec	4.9	0.06	0.57	0.07	0.58

Table 5. *Average monthly exergy of the real and improved collectors (constant water inlet temperature T_{in} =20°C).*

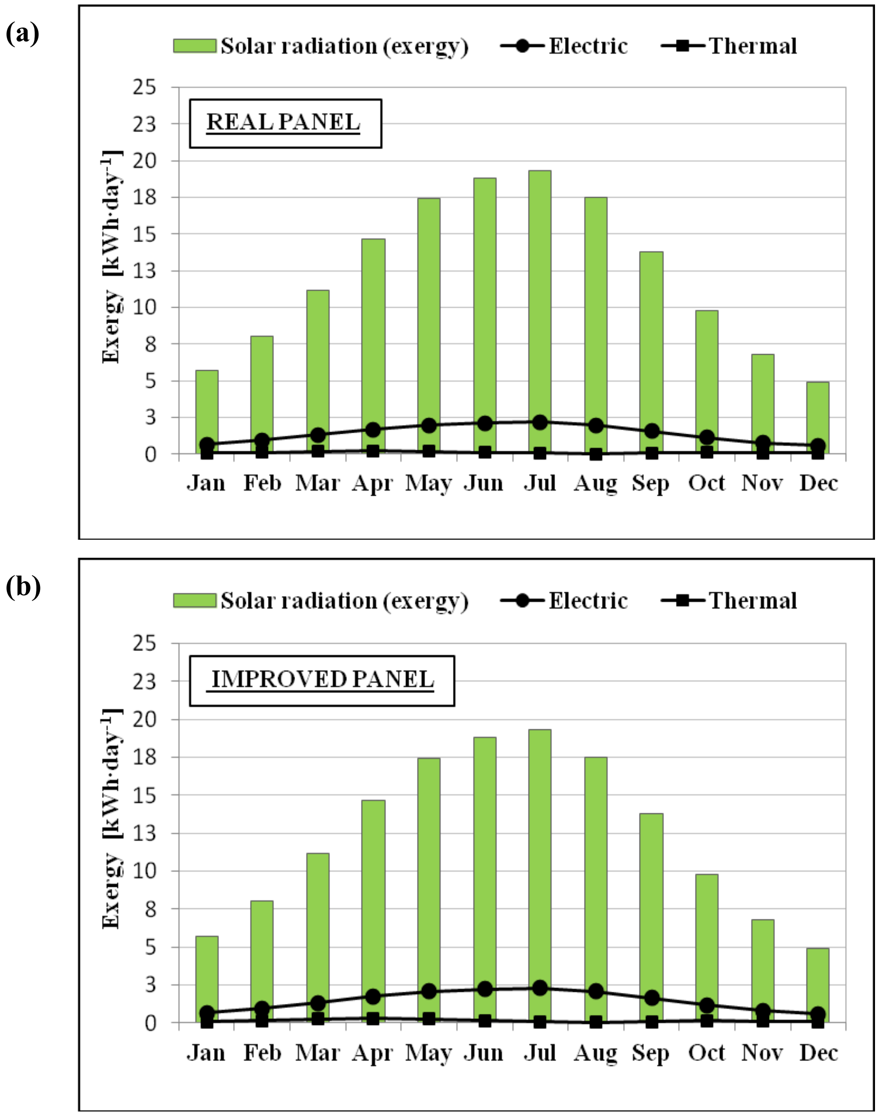

Figure 5. *Average monthly exergy at constant water inlet temperature T_{in}=20°C. (a) Real PVT collector (b) Improved PVT collector.*

These results are plotted in Fig. 5; here, one can observe that the average monthly exergy trends of the improved PVT system are lightly higher than the real collector.

In addition, Table 6 reports the exergy efficiencies of the two considered systems. Indeed, when T_{in} = 20 °C the expected average monthly thermal exergy efficiencies calculated in both cases range from 0.1% to 1.8% and from 0.5% to 2.5%, for real system and improved system, respectively (see Fig. 6), with the lowest values occurring in the hottest months, when the energy efficiency would be at its height (around 60% and 70%, respectively; see Fig. 3).

	Real PVT (T_{in} = 20°C)			**Improved PVT (T_{in} = 20°C)**		
	ξ_t	ξ_{el}	ξ	ξ_t	ξ_{el}	ξ
	[-]	[-]	[-]	[-]	[-]	[-]
Jan	1.2%	14.3%	13.0%	1.6%	14.4%	13.5%
Feb	1.5%	14.2%	13.3%	2.0%	14.5%	14.0%
Mar	1.8%	14.1%	13.4%	2.2%	14.4%	14.1%
Apr	1.6%	14.0%	13.1%	2.0%	14.4%	14.0%
May	1.1%	13.8%	12.6%	1.4%	14.4%	13.3%
Jun	0.6%	13.7%	11.9%	0.8%	14.3%	12.7%
Jul	0.3%	13.7%	11.6%	0.5%	14.4%	12.4%
Aug	0.1%	13.7%	11.4%	0.2%	14.4%	12.1%
Sep	0.4%	13.9%	11.9%	0.6%	14.4%	12.5%
Oct	1.1%	14.0%	12.7%	1.4%	14.4%	13.3%
Nov	1.2%	14.0%	12.8%	1.5%	14.3%	13.3%
Dec	1.2%	14.1%	12.9%	1.4%	14.2%	13.2%

Table 6. *Average monthly values of exergy efficiencies of two different PVT collectors (constant water inlet temperature,* T_{in}*=20°C).*

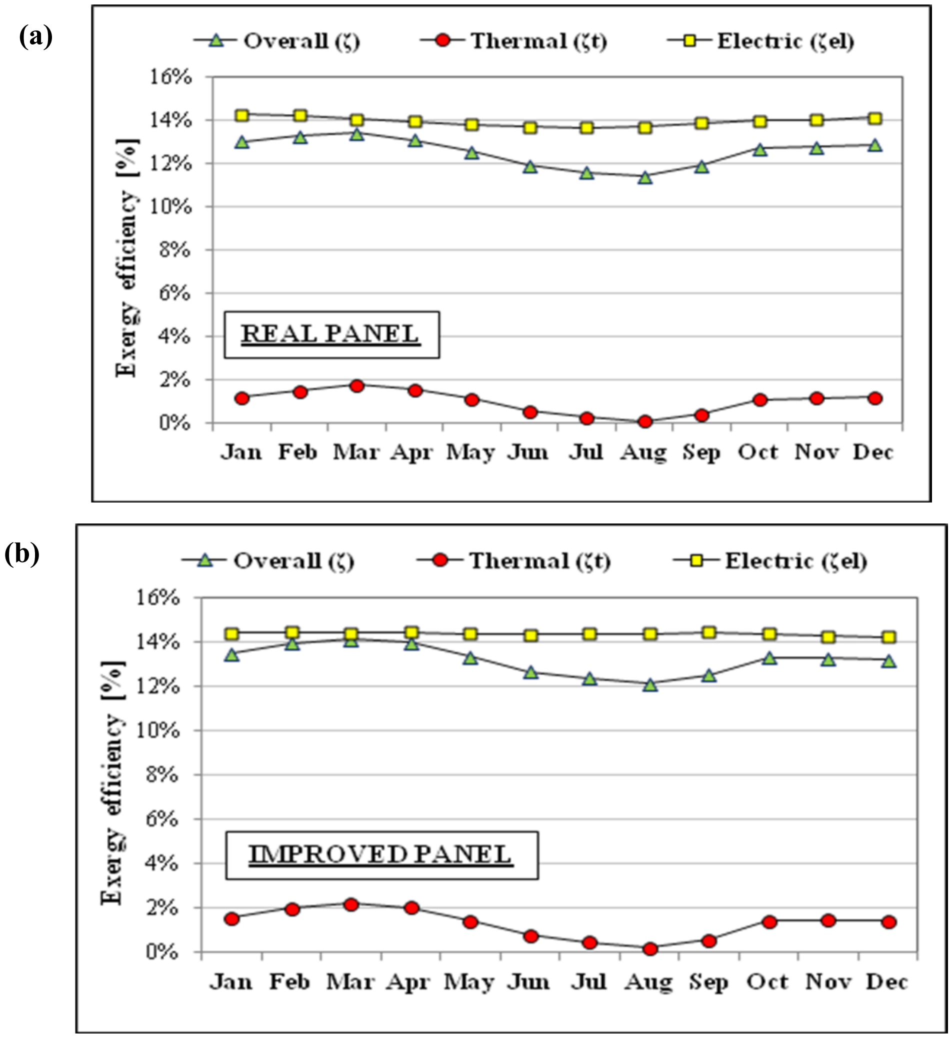

Figure 6. *Average monthly exergy efficiency of the PVT collectors (constant inlet temperature,* T_{in} *=20°C).(a) Real PVT system; (b) Improved PVT system.*

This happens because, despite the PVT collectors are able to convert a relatively high portion of the available solar energy into useful heat, this happens at a temperature that is very close to the ambient temperature (25 – 30 °C), which makes heat scarcely useful on a technical basis. On the other hand, the exergy method exalts the value of the electricity production, as this can be entirely converted into useful work, whatever the temperature of the system; thus, the average exergy efficiency for the electricity production would be even higher than for the thermal energy recovery in both PVT systems, real panel and improved panel (see Fig. 6).

One can also observe that the simulated electric exergy efficiencies (ξ_{el}) overtake the electric energy efficiencies (η_{el}): as an example, in real PVT system η_{el} oscillates between 12.7% and 13.3% (see Fig. 3(a)), while ξ_{el} gets close to 14.3% (see Fig. 6(a)). These differences arise because, for a given energy output, the energy and the exergy content of the solar radiation is not the same, due to the conversion coefficient ψ~~s~~ used in Eq. (6), that is around 0.94 according to Petela.

In conclusion, the overall exergy efficiency ξ is severely penalized by the very low exergy content of the heat recovery in both systems; the highest average values of ξ occur in winter, and attain the peak values of only 13.4% and 14.1% for the real and improved system, respectively.

In Fig. 6 it might seem strange that the overall exergy efficiency ξ turns out to be lower than the electric exergy efficiency ξ_{el}. Actually, this is justified by the definition of ξ provided in Eq. (10): here, ξ_{el} is multiplied by the packing factor PF < 1, as the electricity production takes place only on a limited portion of the absorber surface.

Finally, Fig. 7 shows the effect of the water inlet temperature on the simulated average annual exergy efficiency. Here, one can observe two different trends for the electric and the thermal exergy efficiency in both real and improved systems: while the first one is favored by low water inlet temperatures, the second one decreases at low T_{in}, due to the poor exergy content of the low grade heat. In both systems analyzed, the combination of these two curves produces an interesting result: when operated at constant water inlet temperature, the PVT prototypes would get optimal annual performance for T_{in} in the range from 30°C to 35 °C.

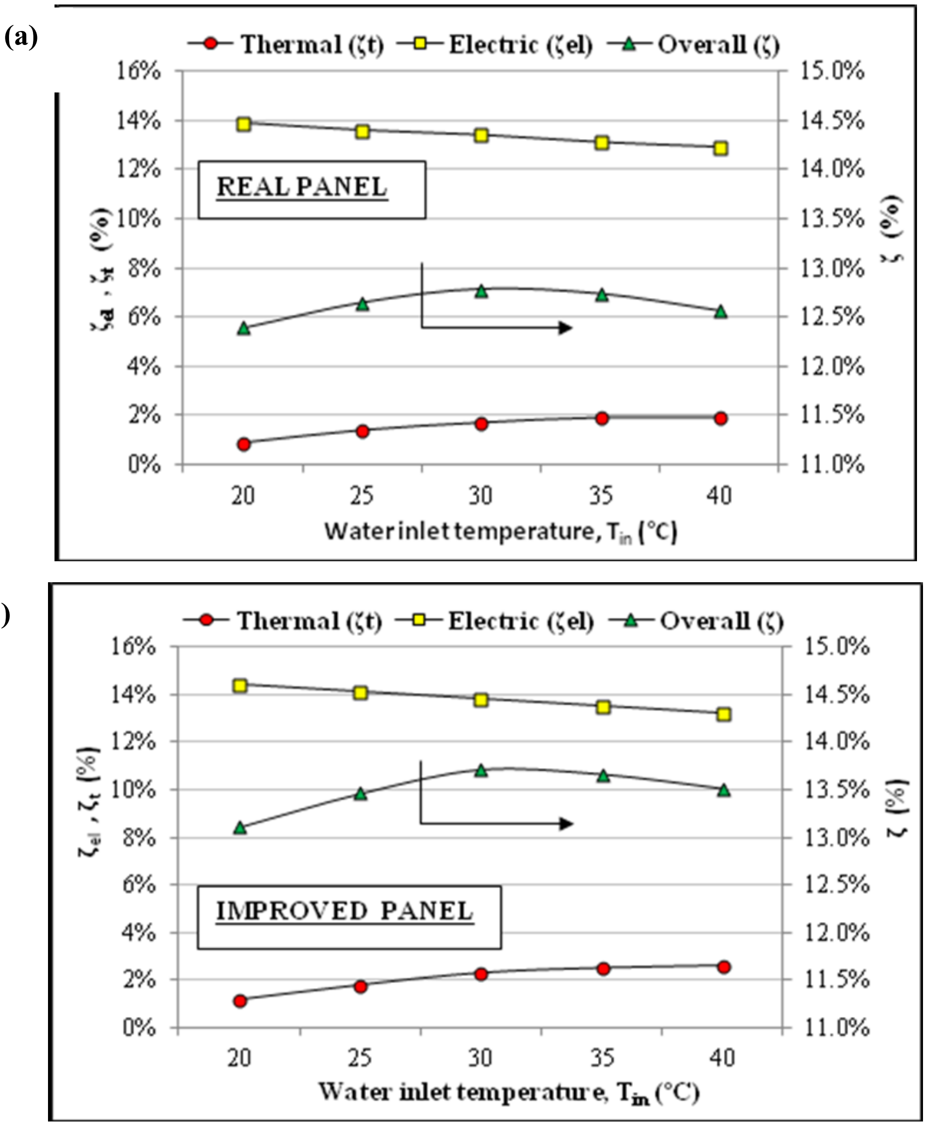

Figure 7. *Average annual exergy efficiency of the PVT collectors as a function of the (constant) water inlet temperature. (a) Real PVT system; (b) Improved PVT system.*

As previously discussed, the investigation based on the First Law of Thermodynamics seems to suggest low temperature operation for the PVT panel in order to maximize its overall energy efficiency (Fig. 4). However, the results plotted in Fig. 7 shows that this strategy is misleading, since heat, no matter how much, is almost useless if available close to the environmental temperature; hence, one should avoid too low operating temperatures. On the contrary, it seems more suitable to look for a compromise between electric and thermal exergy efficiency.

7. Optimum design for the exergy efficiency of the improved PVT system

As previously discussed, the investigation based on the First Law of Thermodynamics seems to suggest low temperature operation for the PVT panel in order to maximize its overall energy efficiency (Fig. 4). However, the results plotted in Fig. 7 shows that this strategy is misleading, since heat, no matter how much, is almost useless if available close to the environmental temperature; hence, one should avoid too low operating temperatures. On the contrary, it seems more suitable to look for a compromise between electric and thermal exergy efficiency. In this section, this issue is further developed. In particular, it is possible to show that there exists – for any operating condition – an optimum water inlet temperature that maximizes the instantaneous overall exergy efficiency of the PVT collector. To this aim, let us consider the definition of exergy efficiency provided in Eq. (10):

$$\xi = \frac{\dot{E}_Q + \dot{E}_{el}}{\psi \; I_{sol} \cdot A_p} = \frac{1}{\psi}\left[\eta \cdot \left(1 - \frac{T_0}{T_m}\right) + \eta_{V} \cdot PF\right] \tag{11}$$

Now, in Eq. (11) one can replace η_{PV} with the corresponding definition , while for the thermal efficiency η_t it is possible to adopt this equation:

$$\eta_{TC} = a - b \cdot \frac{T_p - T_a}{I_{sol}} \tag{12}$$

with a = 0.61 and b = 5.76. As a result, one obtains the following operative formula for the overall exergy efficiency ξ of the prototype of PVT collector:

$$\xi = \frac{1}{\psi} \cdot \left\{\left(a - b \cdot \frac{T_p - T_a}{I_{sol}}\right)\left(1 - \frac{T_0}{T_m}\right) + \eta_{TC} \cdot \left[1 - \mu \left(T_p - 25\right)\right] \cdot PF\right\} \tag{13}$$

If looking at Eq. (13), one can recognize that the overall exergy efficiency ξ depends on the current climatic conditions (I_{sol}, T_a), as well as on both the absorber temperature T_p and the mean thermodynamic temperature Tm. However, it is easy to realize that these two temperatures depend in turn on the climatic conditions, on the water flow rate $\dot{m}_w$ and on the inlet temperature Tin, according to the mathematical model presented in Section 4. Therefore, the exergy efficiency can be finally considered a multivariable function, such as:

$$\xi = f(T_{in}, \dot{m}_w, I_{sol}, T_a) \tag{14}$$

Now, it is predictable that in the right hand side of Eq.(13) the first term – the thermal exergy efficiency – is increasing with Tin, while the second term – the electric exergy efficiency – is decreasing with Tin. Therefore, the overall exergy efficiency ξ may show a maximum.,

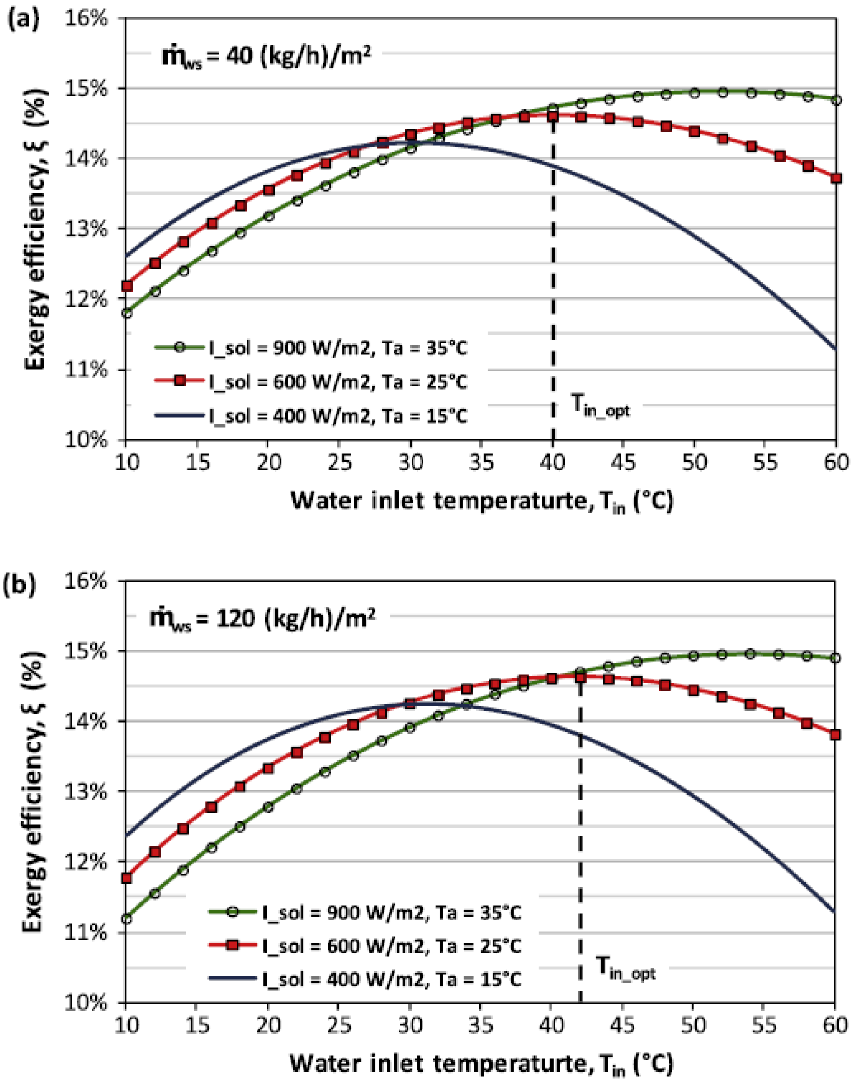

Figure 8. *Instantaneous exergy efficiency of the PVT collector as a function of the operational parameters*

Indeed by using the solar collector data mentioned in the previous sections, one obtains the plots of Fig. 8, that clearly show a maximum. The plots refer to two different water flow rates, belonging to the common operating range for flat plate thermal collectors; each figure presents three different combinations of I_{sol} and T_a, describing typical operating conditions in sunny or cloudy days.

The curves presented in Fig. 8 shows that, for any operating condition, it is possible to identify an optimum fluid inlet temperature T_{in_opt}, for which the overall instantaneous exergy efficiency of the PVT collector would be maximized. Moreover, this optimum temperature is technically feasible, as it belongs to the range commonly occurring in solar thermal systems, i.e. from around 30 °C (when $I_{sol} = 400$ W/m^2 and $T_a = 15$ °C) to around 50 °C (when $I_{sol} = 900$ W/m^2 and $T_a = 35$ °C). The value of the optimum inlet temperature is practically not sensitive to the chosen water flow rate, nor is the peak exergy efficiency achievable by the system. These results introduce the possibility to adopt a simple command-control system, based on a three-way valve installed on the water supply line in the solar loop, intended to feed the PVT collector with water at the optimal supply temperature T_{in_opt}. The latter can be determined in real time through an algorithm based on the mathematical model described in this work, as a function of the values of $\dot{m}_w$, I_{sol} and T_a measured by an appropriate acquisition system. The proposed command-control system would allow the system to work constantly at the physically possible peak of the overall exergy efficiency. An example of how the solar loop would look like is shown in Fig. 9;

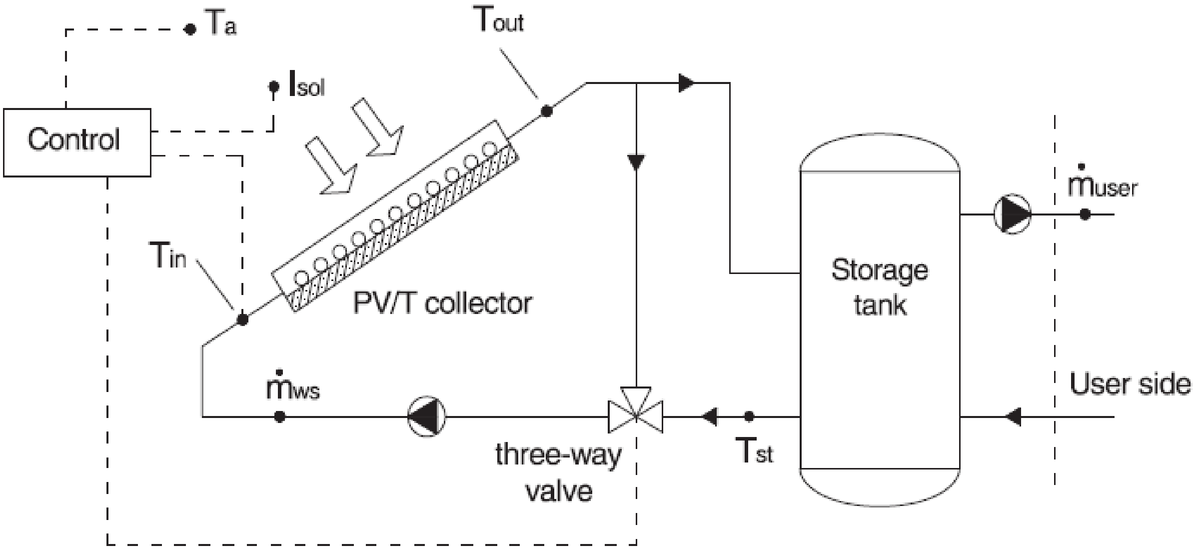

Figure 9. *Simplified sketch of the command-control system on the PVT solar loop*

Actually, the limitation of this configuration is that at each time step the inlet temperature could only fall between the outlet temperature T_{out} and the temperature T_{st} holding in the lower region of the storage tank. Thus, the possibility of getting constantly the exact required T_{in_opt} would be somewhat influenced by the temperature level in the storage tank, hence by the water flow drawn from the storage by the users.

However, the loss in exergy efficiency deriving from an inlet temperature Tin slightly different from the exact T_{in_opt} is almost negligible, since the exergy efficiency curve is almost plate around its peak, especially when working under high solar irradiance (see Fig. 8). As a consequence, a certain tolerance may be accepted in the management of the control-command system. Finally, the potential gain deriving from the application of this control logic is evaluated in Fig. 10.

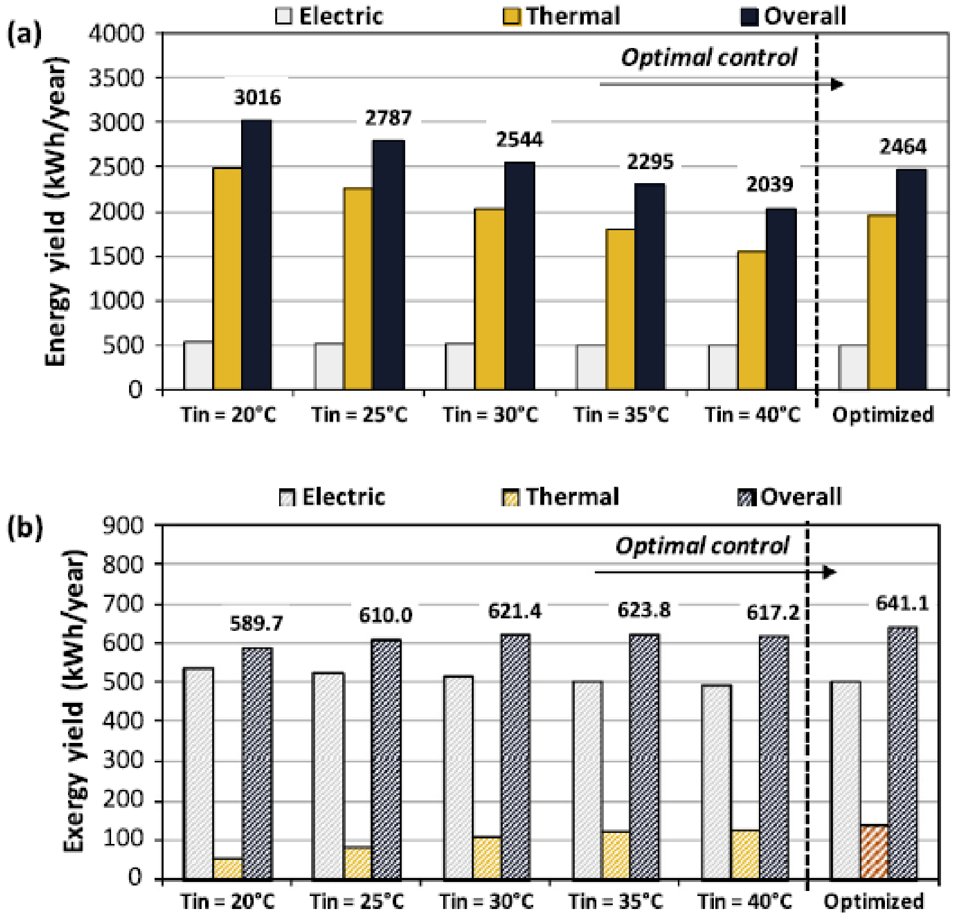

Figure 10. *Annual energy (a) and exergy (b) yield of the PVT collector: effect of an optimized management.*

Here, the expected annual energy yield of the PVT collector (Fig. 10 a) as well as the exergy yield (Fig. 10 b) are determined for several values of the constant inlet temperature Tin; the results are compared to those pertaining to a system based on the optimum control previously discussed. On the one hand, in Fig. 10b it is possible to verify that the optimum management of the PVT system would allow to maximize the annual exergy yield, that would be around 3% higher than with the most performing constant water inlet temperature (T_{in} = 35 °C). On the other hand, the optimal management does not allow to maximize the energy yield: on the contrary, this would be around 18% lower than with T_{in} = 20 °C (see Fig. 10 a). However, it has been already discussed how in this case the higher amount of thermal energy produced would be useless in practice due to the temperature level very close to the ambient conditions.

Conclusions

This thesis concerns a prototype of water-cooled glazed PVT collector integrated into prefabricate concrete, that is being developed in the framework of an Italian research project.

The study aims at evaluating the expected energy performance of a real PVT collector and improved collector, in the light of both the First and the Second Law of Thermodynamics; the evaluation is based on a mathematical model for the dynamic simulation of the system.

According to the First Law of Thermodynamics, the results of this investigation suggest that, when operating at low water inlet temperatures, the collector would reach a very high overall energy efficiency. However, these outcomes may be misleading: indeed, the thermal energy recovered by the PVT collector, even in high quantities, is almost useless when available at low temperatures. On the contrary, the adoption of the Second Law of Thermodynamics, based on the concept of exergy, allows a proper evaluation of the quality of thermal energy, that depends on its temperature level; according to this approach, low temperature operation is not recommended. However, what is more interesting and innovative in this study is that, in the framework of the Second Law of Thermodynamics, it is possible to identify – for any operating condition – an optimum value for the water inlet temperature, that allows to maximize the overall exergy efficiency of the system. This optimum temperature falls within the range commonly occurring in solar thermal systems. These outcomes can be used to define a control logic that might be implemented in a command-control system, based on a three-way valve installed on the water supply line in the solar loop, intended to feed constantly the PVT collector with water at the optimum supply temperature. This would determine the thermodynamic optimization of the PVT system.

References

[1] G. Evola, L. Marletta. Exergy and thermoeconomic optimization of a water-cooled glazed hybrid photovoltaic/thermal (PVT) collector. Solar Energy.

[2] Fujisawa, T., Tani, T., 1997. Annual exergy evaluation on photovoltaic thermal hybrid collector. Solar Energy Mater. Sol. Cells 47, 135–148.

[3] Joshi, A.S., Tiwari, A., 2007. Energy and exergy efficiencies of a hybrid photovoltaic-thermal (PVT) air collector. Renewable Energy 32, 2223– 2241.

[4] Chow, T.T., Pei, G., Fong, K.F., Lin, Z., Chan, A.L.S., Ji, J., 2009. Energy and exergy analysis of photovoltaic-thermal collector with and without glass cover. Appl. Energy 86, 310–316.

[5] Dubey, S., Tiwari, G.N., 2009. Analysis of PVT flat plate water collectors connected in series. Sol. Energy 83, 1485–1498.

[6]. Saidur, R., BoroumandJazi, G., Mekhlif, S., Jameel, M., 2012. Exergy analysis of solar energy applications. Renew. Sustain. Energy Rev. 16, 350–356.

[7] Zhang, X., Zhao, X., Smith, S., Xu, J., Yu, X., 2012. Review of R&D progress and practical application of the solar photovoltaic/thermal (PVT) technologies. Renew. Sustain. Energy Rev. 16, 599–617.

[8] Agrawal, S., Tiwari, G.N., 2011. Energy and exergy analysis of hybrid micro-channel photovoltaic thermal module. Sol. Energy 85, 356–370.

[9] Agrawal, S., Tiwari, G.N., 2012. Exergoeconomic analysis of glazed hybrid photovoltaic thermal module air collector. Sol. Energy 86, 2826–2838.

[10] Agrawal, S., Tiwari, G.N., 2013. Overall energy, exergy and carbon credit analysis by different types of hybrid photovoltaic thermal air collectors.

[11] Bejan, A., Moran, M.J., 1996. Thermal Design and Optimization. John Wiley & Sons, USA.

[12] Coventry, J.S., Lovegrove, K., 2003. Development of an approach to compare the ‘value’ of electrical and thermal output from a domestic PV Thermal system. Sol. Energy 75, 63–72. Energy Convers. Manage. 65, 628–636.

[13] Duran Sahin, A., Dincer, I., Rosen, M., 2007. Thermodynamic analysis of solar photovoltaic cell systems. Sol. Energy Mater. Sol. Cells 91, 153–159.

[14] Hepbasli, A., 2008. A key review on exergetic analysis and assessment of renewable energy resources for a sustainable future. Renew. Sustain. Energy Rev. 12, 593–661.

[15] Pons, M., 2009. On the reference state for exergy when ambient temperature fluctuates. Int. J. Thermodyn. 12 (3), 113–121.

[16] Petela, R., 1964. Exergy of heat radiation. ASME Transact. J. Heat Transfer 2, 187–192.

[17] Petela, R., 2003. Exergy of undiluted thermal radiation. Sol. Energy 74, 469–488.

[18] Jeter, S.M., 1981. Maximum conversion efficiency for the utilization of direct solar radiation. Sol. Energy 26 (3), 231–236.

[19] Saloux, E., Teyssedeou, A., Sorin, M., 2013. Analysis of photovoltaic (PV) and photovoltaic/thermal (PVT) systems using the exergy method. Energy Build. 67, 275–285

[20] Pons, M., 2012. Exergy analysis of solar collectors, from incident radiation to dissipation. Renewable Energy 47, 194–202.